nature cell biology

Article

https://doi.org/10.1038/s41556-026-01936-6

The atypical E3 ligase HOIL-1 safeguards the ribosome during cellular stress

Received: 24 October 2024

Accepted: 20 March 2026

Published online: 30 April 2026

Check for updates

Todd Douglas[1,10] ✉, Pengju Nie[1], Jiasheng Zhang[2,3], Kyrillos S. Abdallah[4], Zhiping Wu[5], Meghan McReynolds[5], Kazuhiro Iwai[6], Junmin Peng[5], Wendy V. Gilbert[4], Lawrence H. Young[2,3,7] & Craig M. Crews[1,8,9]

The ribosome has emerged as a signalling hub that can sense metabolic perturbations and coordinate responses that either restore homeostasis or initiate cell death. The range of insults that signal via the ribosome and the mechanisms governing such cell fate decisions remain uncharacterized. Here we identify the atypical E3 ligase HOIL-1 as an unexpected node in the ribosome signalling network that resolves cellular stress. We find that truncating HOIL-1 mutations associated with dilated cardiomyopathy exacerbate cardiac dysfunction in mice and broadly sensitize cells to nutrient and translational stress. These diverse signals converge on the MAP3K ZAKα, a sentinel of ribotoxic stress. Mechanistically, HOIL-1 promotes ribosome ubiquitination and facilitates cytoprotective ribosome-associated quality control. HOIL-1 loss of function causes glucose starvation to become ribotoxic, leading to ZAKα-dependent ATF4 activation and disulfidptosis driven by the cystine–glutamate antiporter xCT. These data reveal a molecular circuit controlling cell fate during nutrient stress and establish the ribosome as a signalosome that responds to cellular glucose levels.

All living things must at some point mobilize their metabolic reserves to survive. Under conditions of scarcity, such as nutrient deprivation, cells become catabolic via the breakdown of stored fatty acids or glycogen. When these threatening states persist, cells will engage stress response programmes to restore homeostasis. Many such threats converge on the integrated stress response (ISR), during which global protein translation is suppressed while the transcription factor ATF4 is selectively translated to mitigate the stress[1]. Ribosomes are now recognized as signalling hubs that sense a wide range of perturbations and coordinate effector stress response programmes[2–4]. Failure of these programmes to restore homeostasis results in the terminal stress response: cell death.

HOIL-1 is a RING-between-RING (RBR) family E3 ligase whose loss of function results in a fatal multi-organ disease with both immunological and metabolic symptoms[5–14]. This disease, termed polyglucosan body myopathy 1 with or without immunodeficiency (PGBM1), presents with a clear genotype–phenotype spectrum: complete HOIL-1 loss yields fulminant autoinflammatory disease, while frameshift mutations that truncate the catalytic RBR domain predominantly cause myopathy[8]. The latter is associated with pronounced accumulation of glycogen aggregates in cardiomyocytes[6], with heart failure secondary to dilated cardiomyopathy being the main cause of death.

HOIL-1 is most known for its role as a component of the linear ubiquitin assembly complex (LUBAC), an essential regulator of the immune response. LUBAC deficiency impairs immune cell activation and sensitizes to cell death in vivo[5,15–23]. Beyond LUBAC, HOIL-1 also has the rare ability to conjugate ubiquitin onto its substrates via

[1]Department of Molecular, Cellular, and Developmental Biology, Yale University, New Haven, CT, USA. [2]Yale Cardiovascular Research Center, Yale School of Medicine, New Haven, CT, USA. [3]Department of Internal Medicine, Yale School of Medicine, New Haven, CT, USA. [4]Department of Molecular Biophysics and Biochemistry, Yale University, New Haven, CT, USA. [5]Departments of Structural Biology and Developmental Neurobiology, St. Jude Children's Research Hospital, Memphis, TN, USA. [6]Department of Molecular and Cellular Physiology, Graduate School of Medicine, Kyoto University, Kyoto, Japan. [7]Department of Molecular and Cellular Physiology, Yale School of Medicine, New Haven, CT, USA. [8]Department of Pharmacology, Yale University, New Haven, CT, USA. [9]Department of Chemistry, Yale University, New Haven, CT, USA. [10]Present address: Princess Margaret Cancer Centre, University Health Network, Toronto, Ontario, Canada. ✉e-mail: todd.douglas@uhn.ca

an ester linkage. A recent landmark study demonstrated that HOIL-1 can directly ubiquitinate glycogen via this linkage in vitro[24]. In proteins, HOIL-1-mediated ester-linked ubiquitination occurs on serine and threonine residues and has been observed on components of the MyD88 signalosome[25–27]. The immunological features of PGBM1 can be putatively ascribed to these established roles for HOIL-1 in immune signalling. However, the aetiology of the fatal metabolic features of this disease is currently unknown.

While interrogating the role of HOIL-1 in glycogen metabolism, we herein discover that HOIL-1 plays a key role in safeguarding the ribosome during stress. We find that loss of the HOIL-1 RBR domain, as observed in patients with PGBM1, renders cells hypersensitive to disulfidptosis under glucose starvation. By characterizing this non-canonical cell death modality, we show it is initiated by the sentinel of ribotoxic stress, ZAKα, and propagates via ATF4. We define a molecular circuit wherein mutant HOIL-1 acts as a dominant-negative that remodels the ribosome ubiquitin landscape, impairing a cytoprotective quality control response mediated by the RNA-binding proteins PABPC1 and MKRN1. We extend this to show HOIL-1$^{\Delta RBR}$ cells are broadly sensitive to ribotoxic stress. These data position HOIL-1 as a previously unrecognized node in the ribosome signalling network.

Results

HOIL-1 loss exacerbates cardiac remodelling and dilatation under pressure overload

Dilated cardiomyopathy is the most common feature of HOIL-1 loss of function in humans[14]. We first sought to establish whether this could be recapitulated in mice. Full HOIL-1 loss by targeting exons 1 and 2 of *Rbck1* (encoding HOIL-1) is embryonic lethal at e10.5, and is caused by unrestricted endothelial cell death[28]. Conversely, targeting exons 7 and 8 yields viable mice without overt disease[29]. Exons 7–12 encode the RBR domain, highlighting that deletion of the RBR produces a phenotype distinct from that of complete loss in mice and humans. Herein, we refer to these viable mice as HOIL-1$^{\Delta RBR}$.

We subjected wild type (WT; $n = 8$) and HOIL-1$^{\Delta RBR}$ ($n = 10$) mice to transverse aortic constriction (TAC) surgery to induce pressure overload and assessed left ventricular (LV) hypertrophy, function and remodelling over 8 weeks (Fig. 1a). HOIL-1$^{\Delta RBR}$ mice presented with a normal baseline cardiac phenotype at 10 weeks of age. Despite similar pressure overload, as indicated by aortic flow peak velocity after surgery (Fig. 1b), HOIL-1$^{\Delta RBR}$ males, but not females, developed more severe cardiac dilatation 4 weeks post-TAC relative to WT mice (Fig. 1c,d). Histology revealed an increase in cardiomyocyte cross-sectional area (male WT mean 320.2 μm^2 and male HOIL-1$^{\Delta RBR}$ mean 409.5 μm^2) and diameter (male WT mean 17.9 μm and male HOIL-1$^{\Delta RBR}$ mean 20.4 μm) following TAC, consistent with cellular hypertrophy (Fig. 1e,f). No cellular hypertrophy was observed in age-matched untreated mice (Extended Data Fig. 1a,b).

A key feature of PGBM1 is the accumulation of glycogen aggregates in cardiac muscle. Cardiomyocytes from both male and female HOIL-1$^{\Delta RBR}$ mice accumulated dense glycogen aggregates following TAC surgery, which were virtually absent from all WT mice and in untreated control mice (Fig. 1g,h). Using Masson's trichrome to stain collagen, we found no difference between genotypes in myocardial fibrosis (Extended Data Fig. 1c,d). LV contractile function, as assessed by LV ejection fraction, trended lower in male HOIL-1$^{\Delta RBR}$ mice than WT mice but did not reach statistical significance by 8 weeks (Fig. 1i). Nevertheless, male HOIL-1$^{\Delta RBR}$ mice had increased pulmonary oedema as assessed by lung-to-body weight ratio (Fig. 1j), indicative of elevated LV diastolic pressures from cardiac dysfunction. Using terminal deoxynucleotidyl transferase dUTP nick end labelling (TUNEL), we found that the extent of cardiomyocyte apoptosis was variable among mice 9 weeks post-surgery, and there was no difference between genotypes regardless of sex (Extended Data Fig. 1e,f). Apoptotic cell death therefore does not appear to contribute to the exacerbated cardiomyopathy of HOIL-1$^{\Delta RBR}$ mice.

These data demonstrate that loss of HOIL-1 exacerbates cardiac remodelling with the development of excessive LV dilatation, cardiomyocyte hypertrophy and heart failure following pressure overload in a sex-dependent manner.

HOIL-1 promotes glycogenolysis

We sought to explore the role of HOIL-1 in cardiomyocyte function in more mechanistic detail. To this end, we modelled the two main PGBM1 genotypes, namely, complete knockout (KO) or deletion of the C-terminal RBR using exon-specific gRNA in AC16 human immortalized cardiomyocytes (Extended Data Fig. 2a). Targeting exon 2 of *RBCK1* caused full HOIL-1 loss, resulting in destabilized HOIP, the catalytic centre of LUBAC, as expected[30]. Exon-7-directed gRNA also reduced full-length HOIL-1, but HOIP levels remained unchanged (Extended Data Fig. 2b). This is consistent with the expression of the N-terminal LUBAC tethering motif and ubiquitin-like domains in HOIL-1 that stabilize the complex[30] (Extended Data Fig. 2b). Truncated HOIL-1 had greatly reduced expression by immunoblot, as observed with ΔRING1 HOIL-1 in mouse embryonic fibroblasts (MEFs)[31]. Next-generation sequencing confirmed a frameshift after exon 7, resulting in a premature stop codon (Extended Data Fig. 2c). We hereafter refer to these genotypes as HOIL-1^{KO} and HOIL-1$^{\Delta RBR}$.

After having confirmed HOIL-1$^{\Delta RBR}$ mice accumulate myocardial glycogen aggregates (Fig. 1g,h), we measured glycogen levels in our cell lines. We found that during acute glucose starvation, a trigger for glycogenolysis, HOIL-1$^{\Delta RBR}$ cells retained more glycogen than both parental and HOIL-1^{KO} cells (Extended Data Fig. 2d). Using liquid chromatography–tandem mass spectrometry (LC–MS/MS), we measured a pronounced increase in glucose-1-phosphate, the product of glycogenolysis, in parental and HOIL-1^{KO} cells following acute starvation (Extended Data Fig. 2e). No glucose-1-phosphate was measured in starved HOIL-1$^{\Delta RBR}$ cells (Extended Data Fig. 2e), demonstrating that the HOIL-1 RBR domain is necessary for efficient glycogen breakdown during acute nutrient stress.

The HOIL-1 RBR mitigates nutrient stress

Severe nutrient stress triggers programmed cell death[32]. Given that cardiomyocyte cell death is a hallmark of dilated cardiomyopathy and heart failure[33–36], and that HOIL-1 has an established role in cell death[37], we wanted to explore how HOIL-1 loss would impact nutrient stress-induced cell death.

We found that HOIL-1$^{\Delta RBR}$ AC16 cells were highly sensitive to glucose starvation-induced cell death, while complete HOIL-1 loss had no effect (Fig. 2a). The renal cell carcinoma cell line 786-O are glycogen-rich cells that are resistant to glucose starvation[38]; we generated HOIL-1$^{\Delta RBR}$ 786-O cells and found that they also were hypersensitive (Fig. 2b and Extended Data Fig. 2f). HOIL-1^{KO} 786-O cells failed to grow, consistent with a previous report[39]. HOIL-1$^{\Delta RING1}$ MEFs, which lack RING1 of the RBR domain[31], likewise succumbed to glucose starvation more readily than WT cells (Fig. 2c and Extended Fig. 2g).

This sensitivity may be attributed to an inability to utilize glycogen. Inhibition of glycogen phosphorylase did not influence cell death in parental AC16 cells (Extended Data Fig. 3a,b). Depleting glycogen pools via knockdown of glycogen synthase before starvation sensitized AC16 cells to glucose starvation (Extended Data Fig. 3c). Having no accessible glycogen may therefore sensitize cells to glucose starvation-induced cell death.

We next examined the role of other LUBAC components in nutrient stress. CRISPR-Cas9-mediated KO of HOIP did not affect glucose starvation-induced cell death (Extended Data Fig. 3d). HOIL-1 activity limits LUBAC via autoubiquitination[31]; therefore, LUBAC hyperactivity in HOIL-1$^{\Delta RBR}$ cells may drive cell death. Pharmacological inhibition of HOIP using HOIPIN-8[40] did not protect HOIL-1$^{\Delta RBR}$ cells from glucose

https://doi.org/10.1038/s41556-026-01936-6

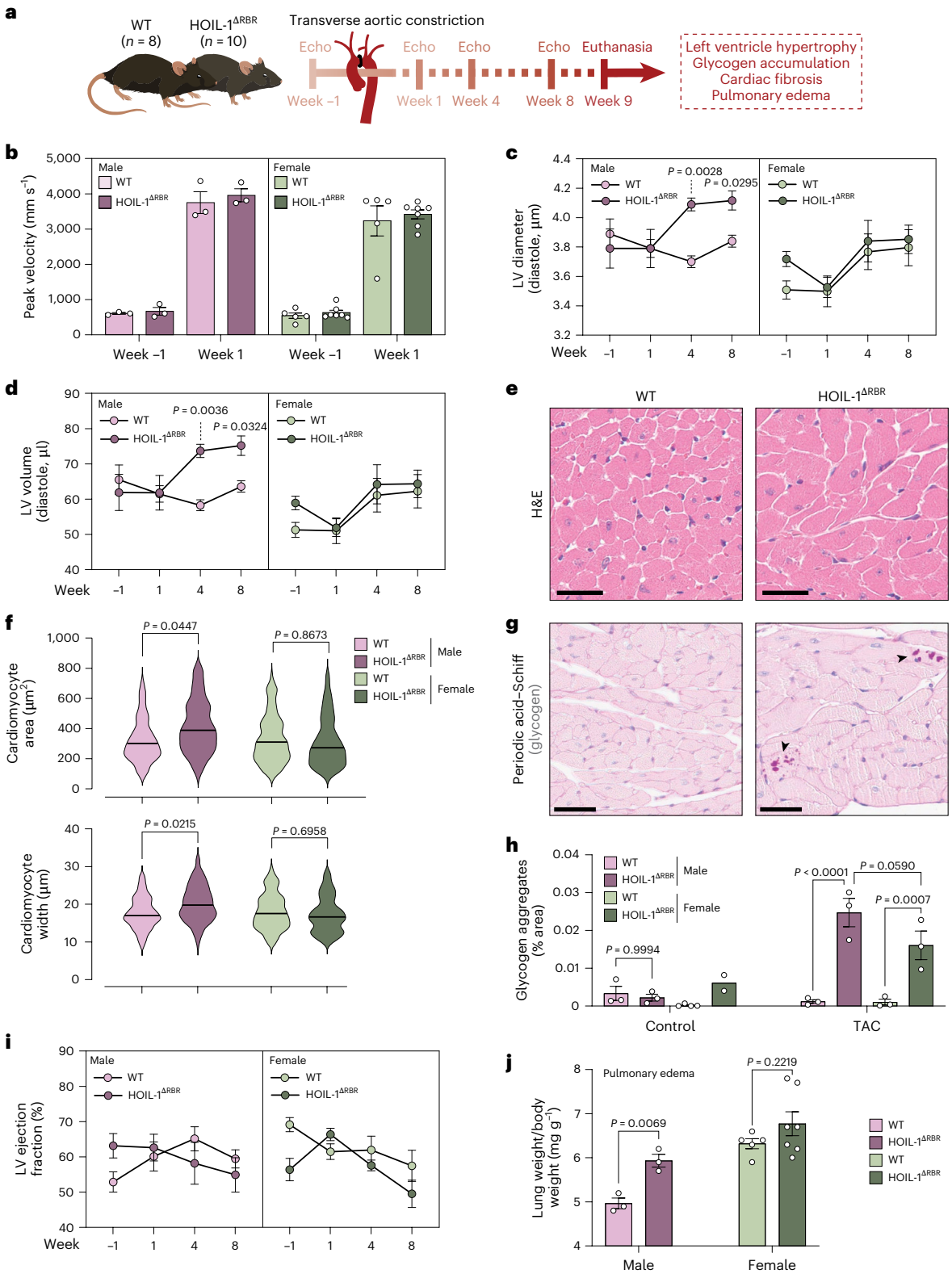

Fig. 1 | HOIL-1 loss exacerbates cardiac remodelling and hypertrophy under pressure overload. a, A schematic of the experimental design assessing cardiac hypertrophy in WT ($n = 8$, 3 males and 5 females) and HOIL-1$^{\Delta RBR}$ ($n = 10$, 3 males and 7 females) mice following TAC surgery. **b**, The peak aortic flow velocity assessed by echocardiography 1 week pre- and post-TAC. **c**, The LV diameter assessed by echocardiography. **d**, The LV volume assessed by echocardiography. **e**, H&E-stained male heart sections 9 weeks post-TAC. Scale bar, 30 µm. **f**, A violin plot of cardiomyocyte cross-sectional area and width quantified from H&E images ($n = 3$ male mice and $n = 3$ female mice per genotype). The black line represents the median. **g**, Periodic acid–Schiff-stained male heart sections 9 weeks post-TAC. Arrowheads indicate glycogen aggregates. Scale bar, 35 µm. **h**, The quantification of glycogen aggregates using Periodic acid–Schiff-stained heart sections. Control mice were age-matched and not subjected to TAC. **i**, Ejection fractions assessed by echocardiography. **j**, The lung weight to body weight ratio assessing pulmonary oedema 9 weeks post-TAC (WT $n = 3$ male mice and $n = 5$ female mice, HOIL-1$^{\Delta RBR}$ $n = 3$ male mice and $n = 7$ female mice). Data are presented as the mean ± s.e.m. (**b**–**d** and **h**–**j**). *P* values were determined by unpaired two-tailed Student's *t*-tests (**c**,**d**,**f**,**h** and **j**).

https://doi.org/10.1038/s41556-026-01936-6

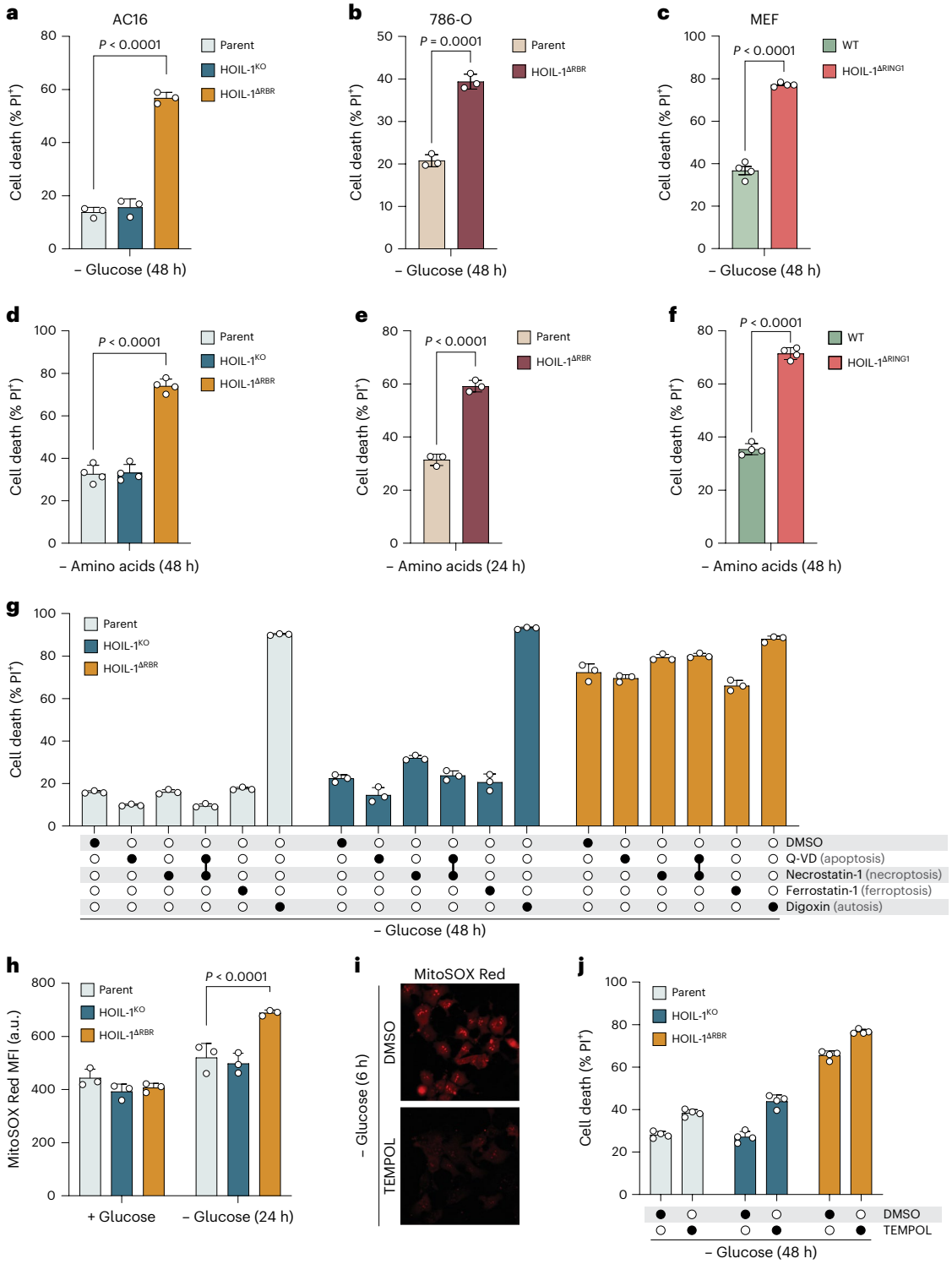

Fig. 2 | HOIL-1 mitigates nutrient stress. a, Cell death in AC16 cells after 48 h glucose starvation ($n = 3$ biological replicates). **b**, Cell death in 786-O cells after 48 h glucose starvation ($n = 3$ biological replicates). **c**, Cell death in MEFs after 48 h glucose starvation ($n = 4$ biological replicates). **d**, Cell death in AC16 cells after 48 h amino acid starvation ($n = 4$ biological replicates). **e**, Cell death in 786-O cells after 24 h amino acid starvation ($n = 3$ biological replicates). **f**, Cell death in MEFs after 48 h amino acid starvation ($n = 4$ biological replicates). **g**, Cell death in AC16 cells treated with cell death inhibitors (Q-VD 5 μM, necrostatin-1 30 μM, ferrostatin-1 2 μM and digoxin 1 μg ml^{-1}) concurrent with 48 h glucose starvation ($n = 3$ biological replicates). **h**, MitoSOX Red mean fluorescence intensity (MFI) assessed by flow cytometry in AC16 cells grown in full media or after 24 h glucose starvation ($n = 3$ biological replicates). **i**, Representative image of MitoSOX Red staining after TEMPOL. No scale bar available given acquisition settings. **j**, Cell death in AC16 cells treated with TEMPOL (50 μM) concurrent with 48 h glucose starvation ($n = 3$ biological replicates). Data are presented as mean ± s.e.m. from one representative experiment. *P* values were determined by unpaired two-tailed Student's *t*-tests (**a**–**f**) or two-way ANOVA followed by Holm–Šídák's multiple comparisons test (**h**).

starvation-induced cell death (Extended Data Fig. 3e). Conversely, and consistent with enhanced LUBAC activity[31], HOIL-1$^{\Delta RBR}$ cells were moderately protected against TNF-induced apoptosis which could be reversed with HOIPIN-8 (Extended Data Fig. 3e). Finally, while LUBAC hyperactivation also occurs following loss of the linear-specific deubiquitinase OTULIN in some cell types[41,42], OTULIN silencing had no effect on glucose starvation-induced cell death (Extended Data Fig. 3f). HOIL-1 therefore acts independently of LUBAC in this context.

To identify whether HOIL-1 is more broadly involved in nutrient stress, we starved cells of amino acids and found that HOIL-1$^{\Delta RBR}$ AC16 cells, HOIL-1$^{\Delta RBR}$ 786-O cells and HOIL-1$^{\Delta RING1}$ MEFs were more sensitive to cell death (Fig. 2d–f). These data demonstrate that the HOIL-1 RBR domain mitigates nutrient stress in multiple cell types.

Glucose starvation induces disulfidptosis in HOIL-1$^{\Delta RBR}$ cells

Unlike the largely universal apoptotic signalling cascade initiated by death receptor ligands, the mechanism of glucose starvation-induced cell death is context-specific and has been attributed to apoptosis[43–45], necrosis[46], necroptosis[47,48], entosis[49] and, more recently, disulfidptosis[38,50].

We sought to characterize the modality of glucose starvation-induced cell death. We tested a panel of inhibitors targeting apoptosis (Q-VD), necroptosis (necrostatin-1), ferroptosis (ferrostatin-1) or autosis (digoxin) and found none prevented cell death in AC16 cells (Fig. 2g). Although we found HOIL-1$^{\Delta RBR}$ cells had elevated mitochondrial superoxide during glucose starvation (Fig. 2h), the reactive oxygen scavenger TEMPOL had no effect (Fig. 2i). We observed sustained AMPK activation in HOIL-1$^{\Delta RBR}$ AC16 cells during prolonged starvation; however, we could not rescue glucose starvation-induced cell death with pharmacological inhibition or activation of either AMPK or mTOR nutrient sensing pathways (Extended Data Fig. 3g,h). These data suggest that HOIL-1$^{\Delta RBR}$ AC16 cells die via a non-canonical cell death programme.

HOIL-1 loss alters the nutrient stress metabolome

We reasoned that cell death caused by glucose starvation may be driven by specific metabolites. We next examined how HOIL-1 deficiency influences the metabolome during nutrient stress. We performed global metabolomics using LC–MS/MS on parental, HOIL-1^{KO} and HOIL-1$^{\Delta RBR}$ AC16 cells in glucose-replete media or following acute (3 h) or prolonged (24 h) glucose starvation (Fig. 3a and Supplementary Table 1). Partial least-squares discriminant analysis (PLS-DA) revealed glucose starvation markedly altered the cellular metabolic profile (Fig. 3b). During glucose starvation, HOIL-1$^{\Delta RBR}$ cells at both timepoints clustered more closely with parent AC16 cells than HOIL-1^{KO} cells (Fig. 3b). These data demonstrate that HOIL-1 loss alters the nutrient stress metabolic signature.

xCT promotes cell death by disrupting glutathione homeostasis

We focused on metabolites with increased abundance in HOIL-1$^{\Delta RBR}$ cells during prolonged starvation as putative drivers of cell death. Pyrimidines were among the most enriched metabolites in starved HOIL-1$^{\Delta RBR}$ cells relative to parent cells (Fig. 3c and Extended Data Fig. 4a,b), so we assessed their contribution. Hydroxyurea (a ribonucleotide reductase inhibitor), brequinar (an inhibitor of de novo pyrimidine synthesis) and oxythiamine (a transketolase inhibitor) all failed to rescue cell death (Extended Data Fig. 4c). Likewise, supplemental uridine did not sensitize cells to glucose starvation (Extended Data Fig. 4c).

Cystine was among the most differentially abundant metabolites in HOIL-1$^{\Delta RBR}$ cells (Fig. 3c). Cystine is imported into the cytosol via system xc$^-$, a cystine–glutamate antiporter consisting of SLC7A11, also known as xCT, and SLC3A2. xCT restricts ferroptosis but during glucose starvation can promote a non-canonical cell death programme termed disulfidptosis caused by excess cystine influx and disulfide stress[38,50]. Consistent with increased cystine, we observed robust upregulation of xCT at the mRNA (Fig. 3d) and protein (Fig. 3e) levels in HOIL-1$^{\Delta RBR}$ cells during glucose starvation. xCT inhibition using either erastin or sulfasalazine (Fig. 3f,g), or CRISPR-Cas9-mediated xCT KO (Fig. 3h), substantially blocked cell death. Conversely, stable xCT overexpression rendered parental AC16 cells sensitive to glucose starvation, which could be blocked by erastin (Extended Data Fig. 4d). Glucose starvation-induced cell death was partially rescued by depleting media of cystine (Extended Data Fig. 4e), demonstrating that xCT drives the distinct cell death observed in HOIL-1$^{\Delta RBR}$ cells in part via cystine import.

Cystine is highly insoluble[51] and rapidly reduced to two molecules of cysteine in the cytosol using NADPH. The pentose phosphate pathway generates the bulk of cellular NADPH from glucose-6-phosphate (Extended Data Fig. 4f). xCT activity during glucose starvation therefore consumes NADPH without replenishing it, increasing the ratio of NADP$^+$:NADPH. We indeed found a sharp increase in the NADP$^+$:NADPH ratio in glucose-starved HOIL-1$^{\Delta RBR}$ cells (Fig. 3i), which was normalized to parental levels by knocking out xCT (Extended Data Fig. 4g). We interrogated whether the collapse of the NADPH system was involved in cell death, as reported in other systems[52]. Inhibiting glucose-6-phosphate dehydrogenase (G6PD), the rate-limiting enzyme of the pentose phosphate pathway, using G6PDi-1[53] increased the NADP$^+$:NADPH ratio (Extended Data Fig. 4h) but did not sensitize cells to glucose starvation (Extended Data Fig. 4i). Another G6PD inhibitor, 6-aminonicotinamide, also had no effect (Extended Data Fig. 4i). Next, we generated cells with doxycycline-inducible expression of the engineered bacterial oxidase TPNOX[54] to artificially oxidize NADPH. No effect on cell death was observed when TPNOX was induced before starvation or concurrently (Extended Data Fig. 4j). These data suggest that NADPH collapse per se is not causing cell death.

An increased NADP$^+$:NADPH ratio reflects a deficit in cellular reducing power. Our untargeted metabolomics screen revealed an accumulation of the glutathione (GSH) precursor γ-glutamylcysteine and oxidized GSH (GSSG) in HOIL-1$^{\Delta RBR}$ cells (Extended Data Fig. 4k), consistent with disulfide stress. We found that GSH synthesis inhibition with buthionine sulfoximine (BSO) enhanced glucose starvation-induced cell death (Fig. 3j). We next assessed the effect of exogenous reducing agents. While neither *N*-acetylcysteine nor tris(2-carboxyethyl)phosphine (TCEP) had a protective effect, GSH ethyl ester dose-dependently suppressed glucose starvation-induced cell death (Fig. 3k). These

Fig. 3 | The nutrient stress metabolome reveals glucose starvation causes disulfidptosis mediated by cystine influx via xCT. a, A schematic of the experimental design examining the metabolome in AC16 cells in full medium or after 3 h or 24 h glucose starvation. **b**, PLS-DA of the metabolomics dataset. **c**, A volcano plot of targeted metabolites in parent and HOIL-1$^{\Delta RBR}$ AC16 cells after 24 h glucose starvation. Significant when −log(*P* value) ≥1.3. **d**, *SLC7A11* mRNA levels (normalized to *TBP*) in AC16 cells after 24 h glucose starvation. Data are represented as the fold change over full medium ($n = 3$ biological replicates). **e**, Immunoblot analysis of xCT levels in AC16 cells during glucose starvation. **f**, A schematic of xCT-dependent nutrient and metabolite flux. **g**, Cell death in AC16 cells treated with erastin (2 μM), sulfasalazine (500 μM) or DMSO vehicle concurrent with 48 h glucose starvation ($n = 4$ biological replicates). **h**, Cell death in xCT^{KO} AC16 cells after 48 h glucose starvation ($n = 3$ biological replicates). Representative immunoblot of xCT KO. **i**, The measurement of NADP$^+$ and NADPH ratios during glucose starvation in AC16 cells ($n = 3$ biological replicates). **j**, Cell death in AC16 cells treated with BSO (500 μM) or DMSO vehicle concurrent with 48 h glucose starvation ($n = 3$ biological replicates). **k**, Cell death in AC16 cells treated with GSH ethyl ester (0.5 mM, 1.0 mM), NAC (0.5 mM, 1.0 mM), TCEP (0.5 mM, 1.0 mM) or H_2O vehicle concurrent with 48 h glucose starvation ($n = 3$ biological replicates). Data are presented as mean ± s.e.m. from one representative experiment. *P* values were determined by moderated *t*-tests using the limma R package followed by the Benjamini–Hochberg procedure (**c**), unpaired two-tailed Student's *t*-tests (**d** and **i**) or two-way ANOVA followed by Dunnett's (**g** and **k**) or Holm–Šídák's (**h** and **j**) post hoc comparisons.

https://doi.org/10.1038/s41556-026-01936-6

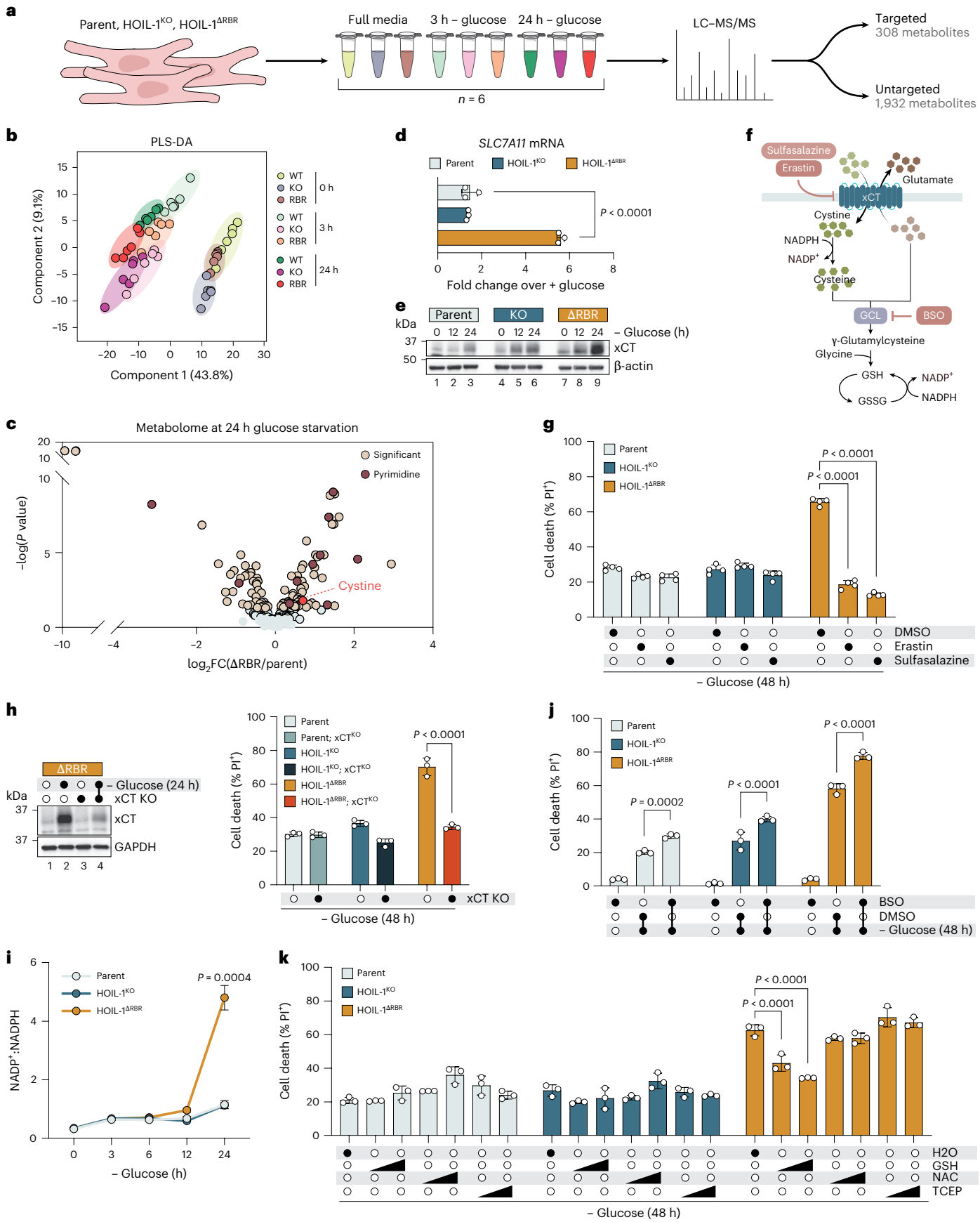

https://doi.org/10.1038/s41556-026-01936-6

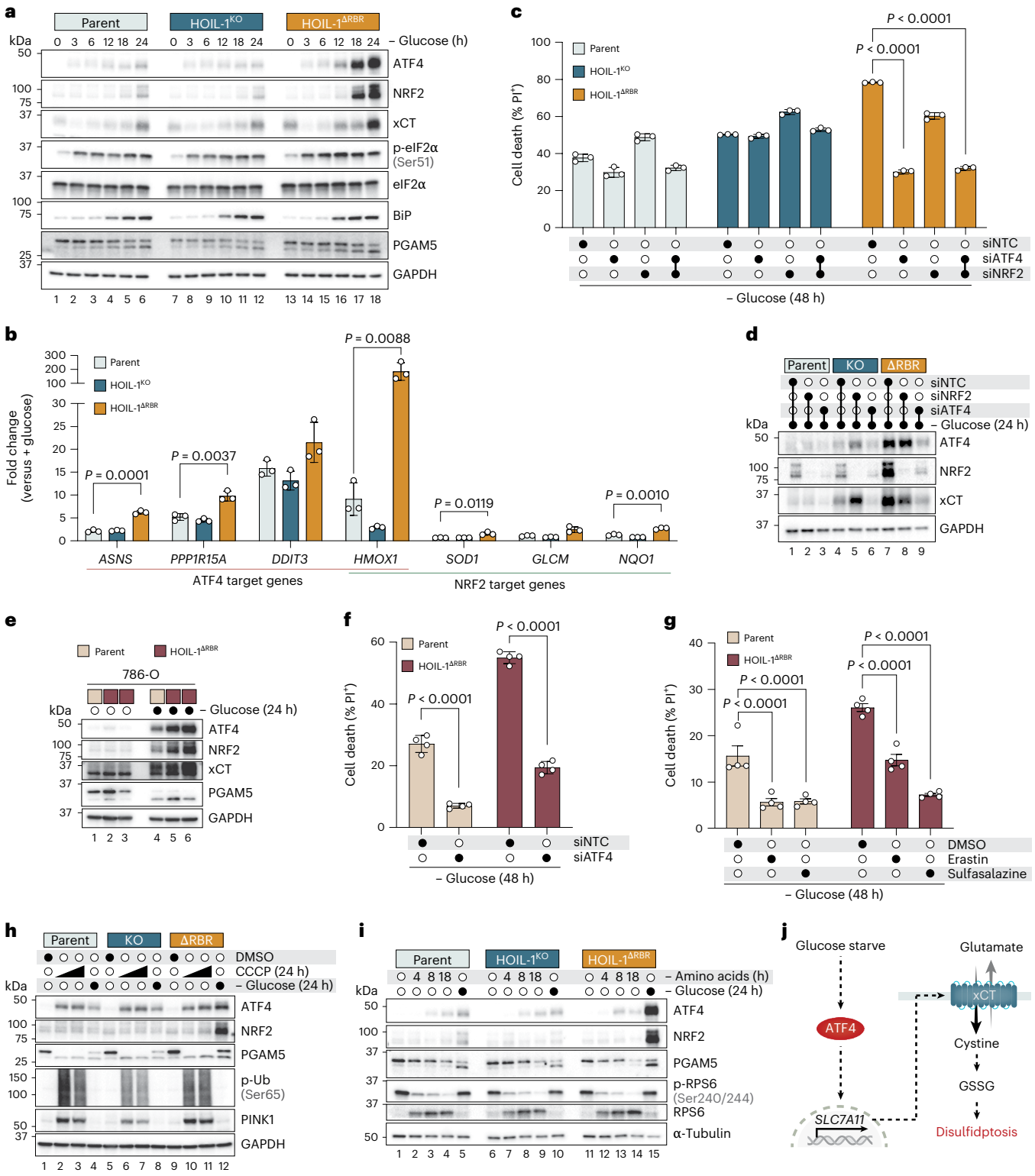

Fig. 4 | ATF4 orchestrates disulfidptosis. a, Immunoblot analysis of AC16 cells after glucose starvation for the indicated timepoints. **b**, ATF4 and NRF2 target genes in AC16 cells measured by RT–qPCR. Data are presented as the fold change over full medium ($n = 3$ biological replicates). **c**, Cell death in AC16 cells transfected with ATF4, NRF2 or non-targeting control (NTC) siRNA 48 h before glucose starvation for 48 h ($n = 3$ biological replicates). **d**, Immunoblot analysis of AC16 cells transfected with ATF4, NRF2 or NTC siRNA 48 h before glucose starvation for 24 h. **e**, Immunoblot analysis of 786-O cells after 24 h glucose starvation. Two different HOIL-1$^{\Delta RBR}$ clones are shown. **f**, Cell death in 786-O cells transfected with ATF4 or NTC siRNA 48 h before glucose starvation for 48 h ($n = 4$ biological replicates). **g**, Cell death in 786-O cells treated with erastin (2 μM), sulfasalazine (500 μM) or DMSO vehicle concurrent with 48 h glucose starvation ($n = 4$ biological replicates). **h**, Immunoblot analysis of AC16 cells after DMSO vehicle, CCCP (5 μM, 25 μM) or glucose starvation for 24 h. **i**, Immunoblot analysis of AC16 cells after amino acid or glucose starvation for the indicated timepoints. **j**, A schematic of the cell death pathway. Data are presented as mean ± s.e.m. from one representative experiment. *P* values were determined by unpaired two-tailed Student's *t*-tests followed by Holm–Šídák's post hoc comparison (**b**, **f** and **g**) or two-way ANOVA followed by Dunnett's post hoc comparison (**c**).

https://doi.org/10.1038/s41556-026-01936-6

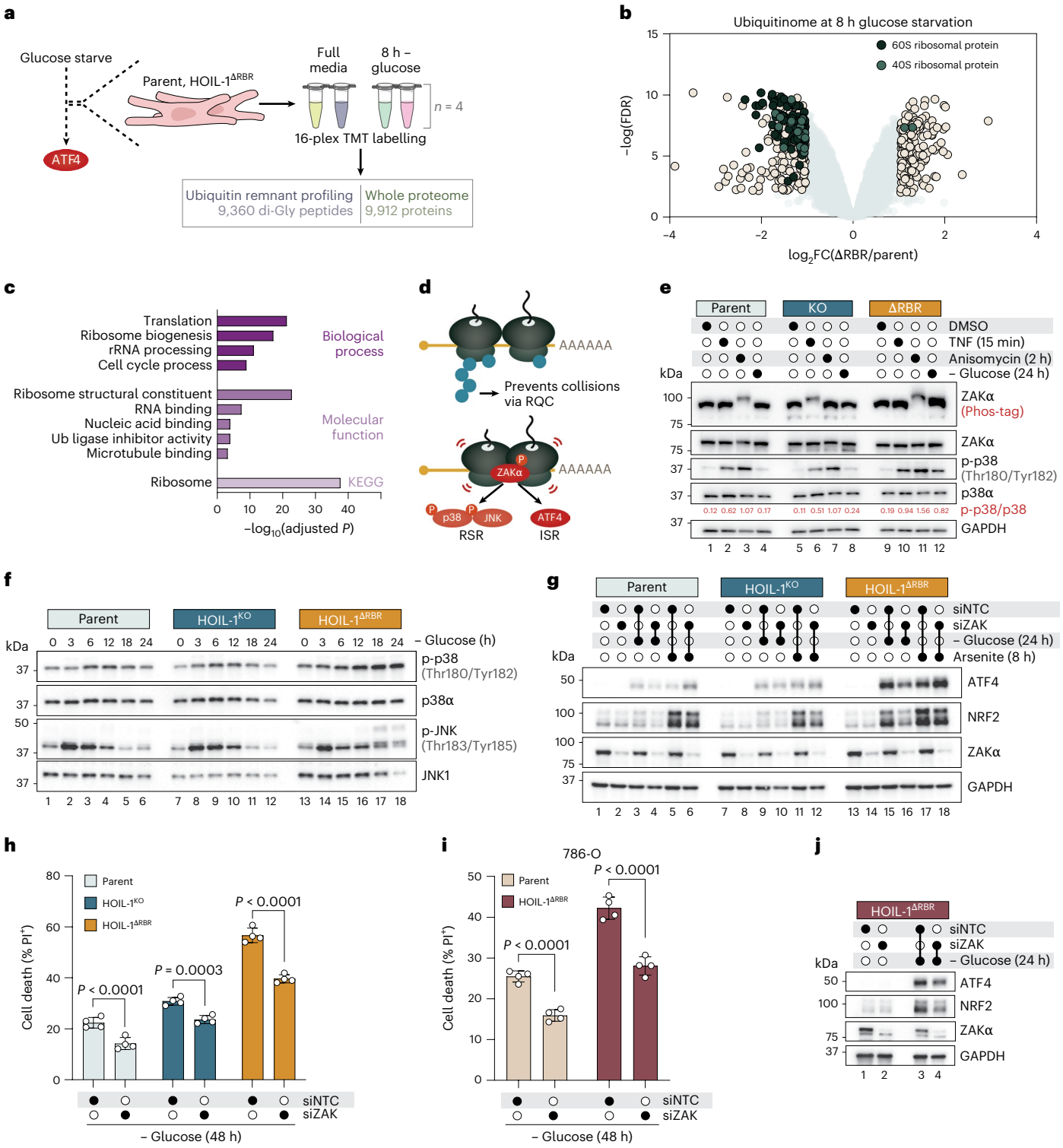

Fig. 5 | Loss of the HOIL-1 RBR domain remodels the ribosome ubiquitin landscape and renders glucose starvation ribotoxic. a, A schematic of the experimental design. **b**, A volcano plot showing differentially ubiquitinated peptides after 8 h glucose starvation. Significant at −log(FDR) ≥2s.d. ≤−2s.d. **c**, Gene Ontology enrichment analysis of proteins with reduced ubiquitin-modified peptides in HOIL-1$^{\Delta RBR}$ cells relative to parent AC16 cells after 8 h glucose starvation. **d**, A schematic of RSR signalling. **e**, An immunoblot analysis of AC16 cells after DMSO vehicle, TNF (10 ng ml^{-1}), anisomycin (5 μM) or glucose starvation for the indicated timepoints. ZAKα phosphorylation was assessed using a Phos-Tag acrylamide gel. **f**, An immunoblot analysis of AC16 cells after glucose starvation for the indicated timepoints. **g**, An immunoblot analysis of AC16 cells transfected with ZAK or NTC siRNA 48 h before sodium arsenite (10 μM) or glucose starvation for the indicated timepoints. **h**, Cell death in AC16 cells transfected with ZAK or NTC siRNA before glucose starvation for 48 h ($n = 4$ biological replicates). **i**, Cell death in 786-O cells transfected with ZAK or NTC siRNA before glucose starvation for 48 h ($n = 4$ biological replicates). **j**, Immunoblot analysis of 786-O cells transfected with ZAK or NTC siRNA before glucose starvation. Data are presented as mean ± s.e.m. from one representative experiment. FDR values were calculated using moderated *t*-tests in the limma R package followed by the Benjamini–Hochberg procedure (**b**); *P* values were determined using the hypergeometric test in ShinyGO (**c**) or two-way ANOVA followed by Holm–Šídák's post hoc comparison (**h** and **i**).

data collectively show that selective upregulation of xCT in HOIL-1$^{\Delta RBR}$ cells during glucose starvation drives disulfidptosis by disrupting GSH homeostasis.

ATF4 orchestrates cell death

Why is xCT uniquely upregulated in HOIL-1$^{\Delta RBR}$ cells during glucose starvation? *SLC7A11* is a target gene of ATF4 and NRF2, two key transcription factors in the ISR and oxidative stress response, respectively. We found that both ATF4 and NRF2 were selectively induced in HOIL-1$^{\Delta RBR}$ AC16 cells during starvation (Fig. 4a). There was a pronounced upregulation of ATF4 and, to a lesser extent, NRF2 target genes in HOIL-1$^{\Delta RBR}$ cells (Fig. 4b), further demonstrating the activation of these transcription factors. Knockdown of ATF4, but not NRF2, abolished xCT upregulation and subsequent cell death (Fig. 4c,d). Glucose starvation-induced cell death was also driven by ATF4 and xCT in HOIL-1$^{\Delta RBR}$ 786-O cells (Fig. 4e–g and Extended Data Fig. 5a,b). We noted that ATF4 knockdown also suppressed NRF2: this regulation was post-transcriptional, specific to glucose starvation and independent of the GSH-degrading enzyme CHAC1[55] (Extended Data Fig. 5c–e).

Curiously, eIF2α phosphorylation, which represses global translation while driving ATF4 translation, was only slightly increased in HOIL-1$^{\Delta RBR}$ cells (Fig. 4a). Consistent with this, HOIL-1$^{\Delta RBR}$ cells had only a modest decrease in global protein synthesis rates as assessed by puromycin incorporation by immunoblot and *O*-propargyl-puromycin incorporation by flow cytometry (Extended Data Fig. 5f,g). ATF4 translation therefore appears divorced from eIF2α phosphorylation in this context.

We next examined whether HOIL-1$^{\Delta RBR}$ cells preferentially engage ATF4 in response to other metabolic stressors and found that neither mitochondrial oxidative phosphorylation uncoupling with cyanide m-chlorophenylhydrazone (CCCP) nor amino acid starvation induced a robust ISR (Fig. 4h,i).

These data collectively demonstrate that loss of the HOIL-1 RBR domain results in maladaptive activation of the ISR effector ATF4 during glucose starvation, leading to xCT-dependent disulfidptosis (Fig. 4j).

Selective autophagy is not involved in the glucose starvation response

Since the RBR of HOIL-1 confers E3 ligase activity, we explored global changes to the ubiquitinome during glucose starvation. We performed ubiquitin remnant profiling before the onset of the ISR to identify molecular events upstream of ATF4 (Fig. 5a and Extended Data Fig. 6a). After 8 h of starvation, there were 186 upregulated and 321 downregulated ubiquitinated peptides ($\log_2$fold change(FC) >1.04 or <−1.04 and false discovery rate (FDR) <0.05) in HOIL-1$^{\Delta RBR}$ cells relative to parental AC16 cells (Supplementary Table 2).

Gene Ontology analysis of proteins with increased ubiquitination revealed an overrepresentation of chaperones and regulators of stress responses and protein processing in the endoplasmic reticulum (ER) (Extended Data Fig. 6b), key players in selective autophagy of the ER (ER-phagy). Indeed, there were data suggesting increased ER-phagy activity. HOIL-1$^{\Delta RBR}$ cells had increased ubiquitinated ARL6IP1 (Extended Data Fig. 6c), an ER-shaping protein whose ubiquitination promotes ER-phagy flux[56]. Further, whole proteome analysis revealed that the level of collagens, a prototypical ER-phagy substrate[57], was dramatically reduced in HOIL-1$^{\Delta RBR}$ cells (Extended Data Fig. 6d and Supplementary Table 3), which we confirmed by immunoblot (Extended Data Fig. 6e). Nevertheless, silencing ARL6IP1 or the ER-phagy receptor FAM134B did not reduce ATF4 translation (Extended Data Fig. 6f). Unlike amino acid starvation or mTOR inhibition, glucose starvation failed to induce ER-phagy flux using two different reporters[58,59] (Extended Data Fig. 6g–i).

The most striking feature of the ubiquitinome dataset was the dramatic reduction in both 40S and 60S ribosomal protein ubiquitination in HOIL-1$^{\Delta RBR}$ cells (Fig. 5b,c), prompting us to explore ribophagy. There was no change in the abundance of ribosomal proteins (Extended Data Fig. 6e), nor did we detect ribophagy flux using a pH-sensitive reporter[60] (Extended Data Fig. 6j,k). Collectively, these data suggest that ER-phagy and ribophagy are not involved in the glucose starvation response.

The ribotoxic sentinel ZAKα activates ATF4 during nutrient stress

Ubiquitination also plays a central role in ribosome quality control (RQC) (Fig. 5d). During translational stress, translating ribosomes may stall on their cognate mRNA, leading to a collision by a trailing ribosome. Ubiquitination of stalled ribosomes facilitates their extraction off mRNA to prevent further collisions[61,62]. As such, inadequate RQC leads to excessive ribosome collisions[63,64]. These collided[2] or stalled[3] ribosomes are sensed by the MAP3K ZAKα, which autophosphorylates and engages a two-pronged stress response involving the stress-activated protein kinases p38 and JNK via the ribotoxic stress response (RSR) and the ISR.

We examined ZAKα activation as a marker of ribosomal stress. During glucose starvation, ZAKα and its downstream target p38 were phosphorylated uniquely in HOIL-1$^{\Delta RBR}$ cells (Fig. 5e). Conversely, the translation elongation inhibitor anisomycin, a known inducer of ribosome collisions, triggered ZAKα activation in all genotypes. Time-course analyses demonstrated rapid and sustained activation of p38 and JNK during glucose starvation in HOIL-1$^{\Delta RBR}$ cells (Fig. 5f) and HOIL-1$^{\Delta RING1}$ cells (Extended Data Fig. 7a). ZAK silencing, which targets both ZAKα and ZAKβ isoforms, attenuated ATF4 in response to glucose starvation but not sodium arsenite, a general inducer of oxidative stress (Fig. 5g) and protected against disulfidptosis in HOIL-1$^{\Delta RBR}$ AC16 and 786-O cells (Fig. 5h–j).

GCN1 and GCN2 are kinases proposed to function in ribotoxic stress signalling[2]; however, GCN2 inhibition or deletion also causes more ribosome collisions by increasing translation initiation[3,65]. We found that GCN1 or GCN2 silencing enhanced disulfidptosis and ATF4 translation in glucose-starved HOIL-1$^{\Delta RBR}$ AC16 cells (Extended Data Fig. 7b,c). We then sought to better characterize the ISR signalling cascade in HOIL-1$^{\Delta RBR}$ cells. We individually silenced each known eIF2α kinase (HRI, PKR, PERK and GCN2) and found no effect on cell death or phospho-eIF2α levels (Extended Data Fig. 7d,e). These data suggest that RSR activation and disulfidptosis are not controlled by GCN1/GCN2 or other eIF2α kinases in this context.

HOIL-1 silences the RSR by promoting ribosome ubiquitination

After establishing ZAKα promotes disulfidptosis in HOIL-1$^{\Delta RBR}$ cells, we next investigated whether HOIL-1 loss of function enhances cell death during canonical ribotoxic stress. Both HOIL-1^{KO} and HOIL-1$^{\Delta RBR}$ AC16 cells were hypersensitive to anisomycin; however, ZAK silencing abolished cell death in HOIL-1$^{\Delta RBR}$ cells but had only a modest effect in HOIL-1^{KO} cells (Fig. 6a), suggesting that excess cell death in HOIL-1^{KO} cells is largely RSR-independent. Expanding our search, we found HOIL-1$^{\Delta RBR}$ AC16 and 786-O cells and HOIL-1$^{\Delta RING1}$ MEFs were dose-dependently sensitive to a panel of ribotoxic stressors with distinct mechanisms of action: harringtonine, hygromycin and UV-C irradiation (Fig. 6b and Extended Data Fig. 8a,b). HOIL-1 loss of function caused prolonged ZAKα and JNK phosphorylation during translational arrest (Extended Data Fig. 8c–e), suggesting HOIL-1 silences the RSR.

Ubiquitination of ribosomal proteins RPS10 and RPS20 resolves cellular stress by promoting ribosome extraction and recycling, mRNA decay and eventual nascent peptide degradation[62,66]. We quantitatively examined RPS10 and RPS20 ubiquitination kinetics during translational stress and found they peaked ~5–15 min after anisomycin treatment and were significantly impaired in HOIL-1-deficient AC16 cells, 786-O cells and MEFs (Fig. 6c–h). These data demonstrate HOIL-1

https://doi.org/10.1038/s41556-026-01936-6

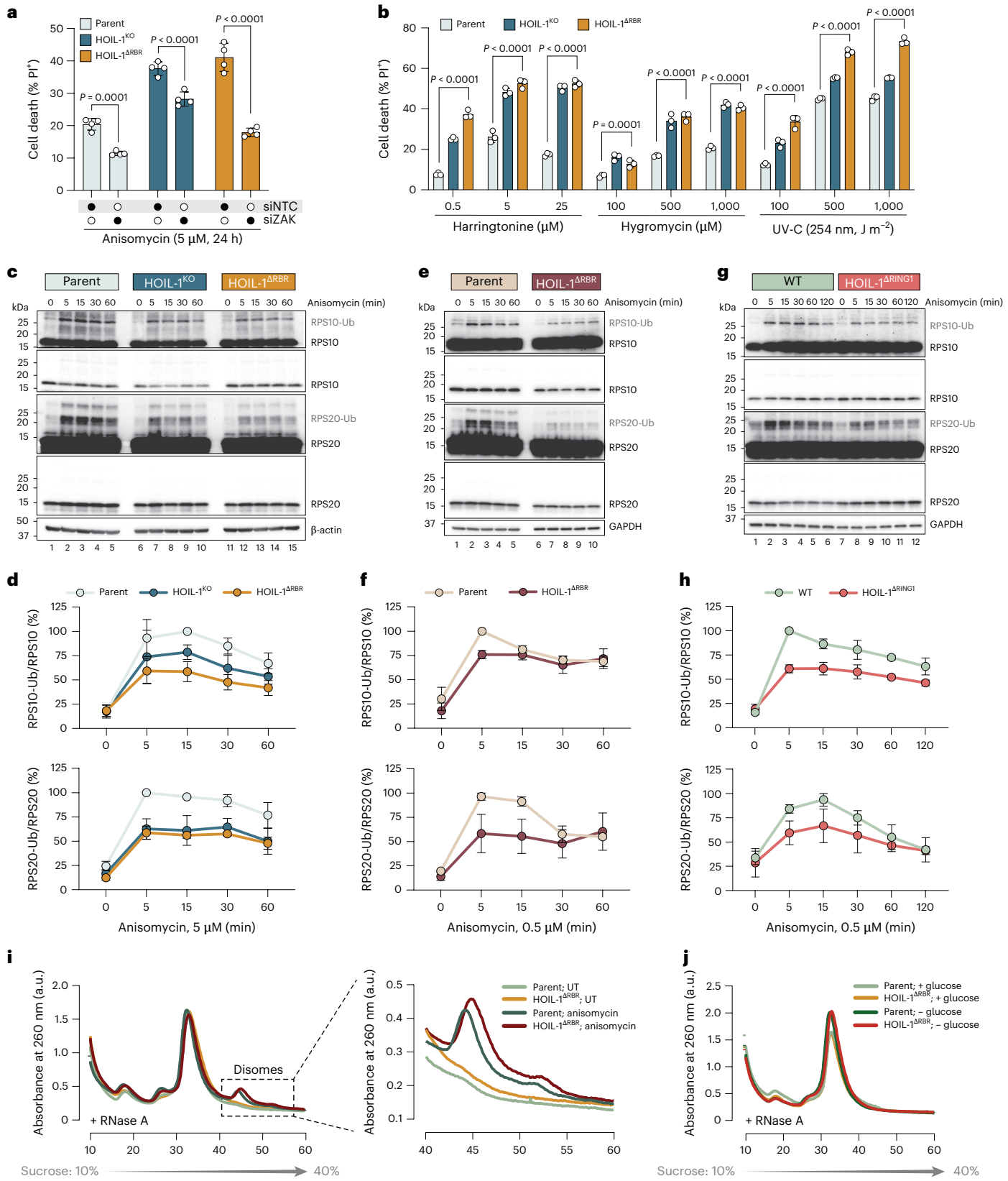

Fig. 6 | HOIL-1 resolves translational stress by promoting quality control-associated ubiquitination and limiting ribosome collisions. a, Cell death in AC16 cells transfected with ZAK or NTC siRNA 48 h before anisomycin (5 μM) treatment for 24 h ($n = 4$ biological replicates). **b**, Cell death in AC16 cells treated with the indicated ribotoxic stressors for 24 h ($n = 3$ biological replicates). **c**,**e**,**g**, Immunoblot analysis of RPS10 and RPS20 ubiquitination during anisomycin treatment in AC16 cells (**c**), 786-O cells (**e**) or MEFs (**g**). **d**,**f**,**h**, Quantification of RPS10 and RPS20 ubiquitination by immunoblot densitometry analysis from three independent experiments in AC16 cells (**d**), 786-O cells (**f**) or MEFs (**h**). Data were calculated as the percentage of the maximum RPS-ubiquitin (Ub)/total RPS within the experiment and represented as the mean ± s.e.m. **i**, Polysome profiles from RNase A-digested lysates of AC16 cells treated with anisomycin (5 μM) for 1 h or left untreated. **j**, Polysome profiles from RNase A-digested lysates of AC16 cells starved of glucose for 24 h or fed full medium. Data are presented as mean ± s.e.m. from one representative experiment. *P* values were determined by two-way ANOVA followed by Holm–Šídák's post-hoc comparison (**a**,**b**).

promotes RQC during translational arrest by regulating ribosomal protein ubiquitination. By contrast, we could not detect RPS10 or RPS20 ubiquitination during glucose starvation at any timepoint (Extended Data Fig. 8f).

ZAKα is activated by ribosome stalling during glucose starvation in HOIL-1$^{\Delta RBR}$ cells

ZAKα is activated by both ribosome collisions and ribosome stalling. After obtaining several lines of evidence that ZAKα is active in HOIL-1$^{\Delta RBR}$ cells, we performed polysome and disome profiling to examine ribosome collisions (Extended Data Fig. 9a–d). Following anisomycin treatment, we observed more higher-order ribosome complexes in HOIL-1$^{\Delta RBR}$ cells (Extended Data Fig. 9b), consistent with more collisions[67]. By contrast, glucose starvation triggered the collapse of polysomes into 80S monosomes (Extended Data Fig. 9c). By immunoblot analysis, anisomycin caused a marked shift in the collision-specific marker EDF1[68] (Extended Data Fig. 9d), while glucose starvation had no effect on either EDF1 or GIGYF2, another collision marker[69,70] (Extended Data Fig. 9d). We likewise observed no differential shift in ZAKα between genotypes.

Two collided ribosomes form an RNase-resistant disome that protects bound mRNA species. To more directly probe for the presence of collisions, we digested lysates with RNase before sucrose fractionation. In untreated cells, RNase digestion flattened polysomes as expected (Fig. 6i). Anisomycin treatment triggered the formation of a distinct disome peak that was taller in HOIL-1$^{\Delta RBR}$ cells than parental cells (Fig. 6i), confirming that loss of the HOIL-1 RBR increases ribosome collisions during translational arrest. We did not observe disomes after 24 h of glucose starvation, when ZAKα is activated in HOIL-1$^{\Delta RBR}$ cells (Fig. 6j). These data suggest ZAKα is probably activated by ribosome stalling, not collisions, during glucose starvation. Of note, neither ribosome collisions nor RPS10/RPS20 ubiquitination are observed during amino acid starvation[2,3], suggesting a distinct pathway to RSR activation during nutrient stress versus translational arrest.

We next examined the effect of HOIL-1 loss on ribosome stalling using a dual fluorescence reporter consisting of GFP and RFP separated by a linker of 20 lysines encoded by AAA codons, or a Flag tag as a non-stalling control[71] (Extended Data Fig. 9e). Poly(A) stretches cue ribosome stalling[72], impairing downstream RFP translation. As a control, silencing of ZNF598, an RQC E3 ligase that promotes stalling[61], increased the RFP:GFP ratio (Extended Data Fig. 9f). HOIL-1^{KO} cells had a defect in stalling comparable to ZNF598 silencing, while HOIL-1$^{\Delta RBR}$ cells did not (Extended Data Fig. 10g,h), suggesting that full-length HOIL-1 promotes ribosome stalling.

Collectively, these data identify the HOIL-1 RBR domain as an engineer of the ribosome ubiquitin landscape that controls cell fate under translational stress downstream of ribosome stalling.

The HOIL-1 proximitome during glucose starvation reveals an enrichment of RNA-binding proteins

How could loss of the HOIL-1 RBR cause widespread changes to ribosome ubiquitination during glucose starvation? To address this question, we sought to resolve the HOIL-1 proximitome during glucose starvation using proximity labelling. We fused the MiniTurbo biotin ligase to either the N- or C-terminus of ΔRBR HOIL-1 and stably expressed these constructs in HOIL-1$^{\Delta RBR}$ AC16 cells, using GFP-MiniTurbo as a negative control (Fig. 7a). This approach identified 24 proteins across two independent experiments that were enriched in both HOIL-1-MiniTurbo cell lines relative to GFP-MiniTurbo after 6 h of starvation, of which, unexpectedly, half (12/24) were RNA-binding proteins (Fig. 7b and Supplementary Table 4). Among these 24, only PABPC1 had decreased ubiquitination in HOIL-1$^{\Delta RBR}$ cells during glucose starvation (Extended Data Fig. 10a), highlighting its potential as a direct HOIL-1 substrate. STRING analysis identified PABPC1 as a hub of the HOIL-1 proximitome, further supporting its candidacy (Extended Data Fig. 10b).

Mutant HOIL-1 excludes MKRN1 from PABPC1, rendering glucose starvation ribotoxic

PABPC1 is a cytosolic poly(A) binding protein whose ability to regulate virtually all aspects of mRNA metabolism is dictated by the various protein complexes it assembles. For example, PABPC1 promotes translation initiation via mRNA circularization through interaction with the eIF4E/eIF4G cap-binding complex[73,74], stimulates deadenylation and prevents mRNA decay via interaction with the CCR4–NOT complex[75,76], and, critically, promotes ribosome ubiquitination via interaction with the E3 ligase MKRN1[77].

We first validated the binding between PABPC1 and HOIL-1 in 786-O cells, which had higher expression of endogenous ΔRBR HOIL-1 than AC16 cells (Extended Data Fig. 2f). We found that both full-length and ΔRBR HOIL-1 bound PABPC1 in glucose-replete media and this binding was enhanced for both proteoforms during glucose starvation (Fig. 7c). In HEK293T cells, we found that co-expression of full-length HOIL-1 triggered PABPC1 ubiquitination (Extended Data Fig. 10c). As expected, ΔRBR HOIL-1 had no effect on ubiquitination, while MKRN1, a known PABPC1 E3 ligase[77], robustly modified PABPC1 (Extended Data Fig. 10c). HOIL-1 can target serine and threonine residues for ubiquitination via an ester linkage. To assess whether HOIL-1-generated PABPC1 polyubiquitin chains contained ester linkages, we used the engineered bacterial deubiquitinase TssM*, which has a 5,000-fold increased specificity for ester-linked substrates over conventional isopeptide linkages[78]. Transfection of TssM* abolished PABPC1 ubiquitination caused by HOIL-1 overexpression but had only a modest effect on MKRN1-mediated ubiquitination (Fig. 7d). These data suggest HOIL-1 can modify PABPC1 with ester-linked polyubiquitin chains.

As observed in 786-O cells, full-length HOIL-1 binds endogenous PABPC1 in AC16 cells during glucose starvation (Fig. 7e). We could not detect ΔRBR HOIL-1 in AC16 cells owing to poor immunoreactivity and low expression. During glucose starvation, a smear characteristic of polyubiquitination was observed above PABPC1 in parental and HOIL-1^{KO} cells but not HOIL-1$^{\Delta RBR}$ cells, suggesting that the loss of the HOIL-1 RBR abrogates endogenous PABPC1 ubiquitination.

Fig. 7 | Mutant HOIL-1 binds PABPC1 and excludes MKRN1, triggering ribotoxic stress during glucose starvation. a, A schematic of the experimental design examining the ΔRBR HOIL-1 proximitome in AC16 cells in full medium or after 6 h glucose starvation. **b**, A volcano plot showing $\log_2$FCs of proteins detected in ΔRBR HOIL-1-MiniTurbo streptavidin pulldown samples over GFP-MiniTurbo samples after 6 h glucose starvation. Significant when $-\log_{10}$(*P* value) >1.3 and $\log_2$FC >0.6. **c**, Immunoblot analysis following endogenous HOIL-1 or IgG immunoprecipitation from 786-O lysates. **d**, Immunoblot analysis of HEK293T cells transfected with the indicated plasmids, followed by denaturing lysis and GFP-Trap immunoprecipitation. **e**, Immunoblot analysis following endogenous PABPC1 or IgG immunoprecipitation from AC16 lysates. The asterisk denotes the IgG heavy chain and the arrowheads denote full-length HOIL-1. **f**, The quantification of MKRN1–PABPC1 binding under glucose starvation by immunoblot densitometry analysis from three independent experiments, as in **e**. The ratio of MKRN1:PABPC1 in parental AC16 lysates in full medium was set to 1.0. **g**, Immunoblot analysis of AC16 cells stably expressing PABPC1-GFP following sodium arsenite treatment (10 μM) for 8 h or glucose starvation for 24 h. **h**, Immunoblot analysis of AC16 cells stably expressing PABPC1-GFP after 24 h glucose starvation. ZAKα phosphorylation was assessed using a Phos-Tag acrylamide gel. **i**, Cell death in AC16 cells stably expressing MKRN1 or ZNF598 after 48 h glucose starvation ($n = 3$ biological replicates). **j**, Immunoblot analysis of AC16 cells stably expressing MKRN1 or ZNF598 after 24 h glucose starvation. **k**, Immunoblot analysis of AC16 cells transfected with the indicated siRNA before glucose starvation. Data are presented as mean ± s.e.m. from one representative experiment. *P* values were determined by a two-tailed Mann-Whitney *U*-test followed by Benjamini–Hochberg correction (**b**) or two-way ANOVA followed by Dunnett's post hoc comparison (**i**).

https://doi.org/10.1038/s41556-026-01936-6

One outstanding question from our data thus far is: what explains the disparity in phenotypes between HOIL-1^{KO} and HOIL-1$^{\Delta RBR}$ cells? One possibility is that truncated HOIL-1 acts as a dominant-negative, wherein it binds to its substrate but does not ubiquitinate it. To explore this, we compared PABPC1 interactions in HOIL-1^{KO} and HOIL-1$^{\Delta RBR}$ AC16 cells during glucose starvation.

MKRN1 is recruited to ribosomes via PABPC1 to initiate RQC. We found that the interaction between MKRN1 and PABPC1 was quantitatively impaired in HOIL-1$^{\Delta RBR}$ cells during glucose starvation across three independent experiments (Fig. 7e,f). Truncated HOIL-1 did not universally shield PABPC1 interactors; MKRN2 binding to PABPC1 was not impaired, while LARP1 binding was enhanced. Subcellular fractionation of RNA–protein granules further revealed MKRN1 is depleted from this fraction in HOIL-1$^{\Delta RBR}$ cells during starvation despite equivalent PABPC1 levels (Extended Data Fig. 10d, lanes 46 and 47). These data suggest that HOIL-1 regulates PABPC1 functionalization and reveals MKRN1 is mislocalized in HOIL-1$^{\Delta RBR}$ cells during nutrient stress.

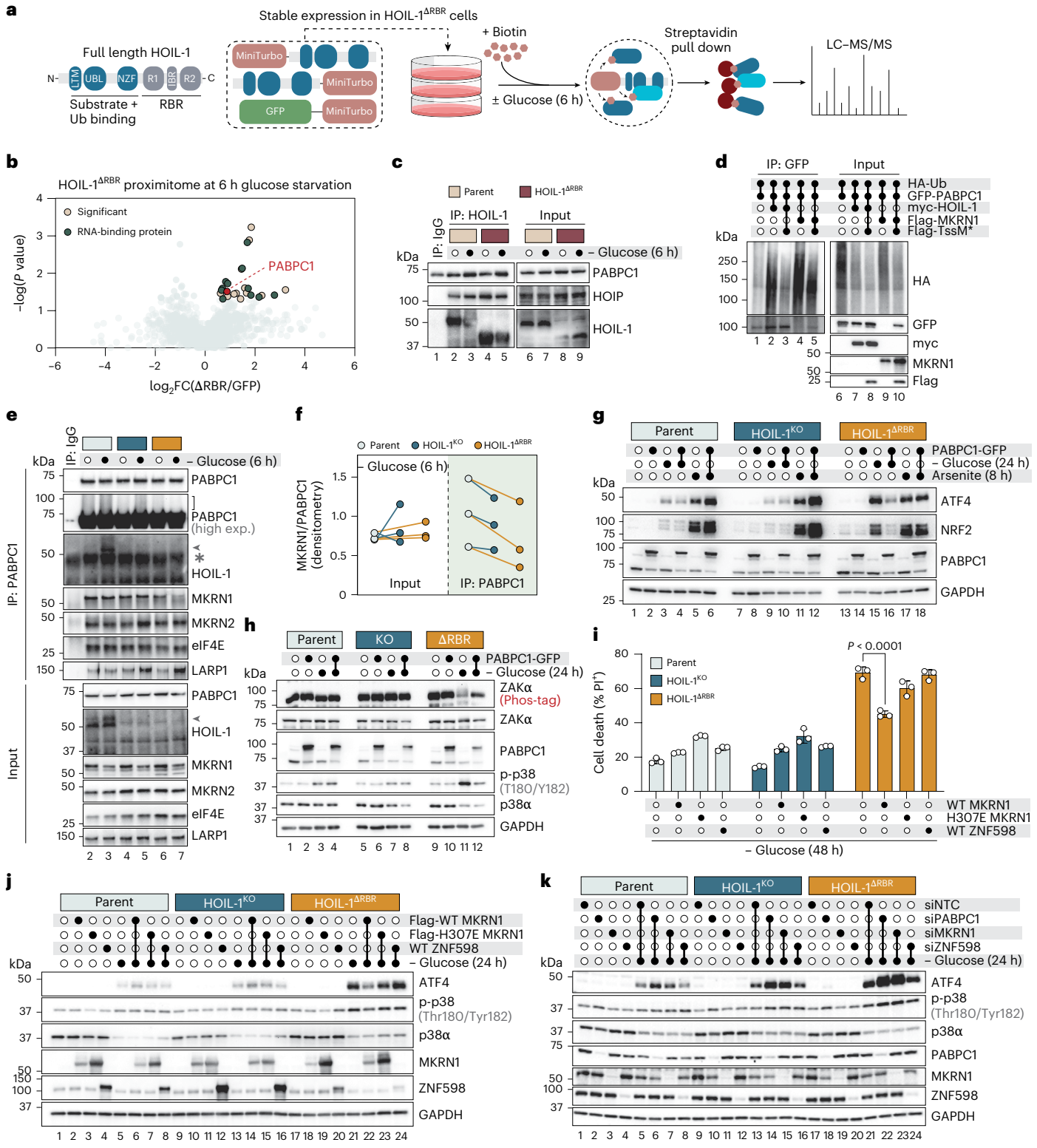

https://doi.org/10.1038/s41556-026-01936-6

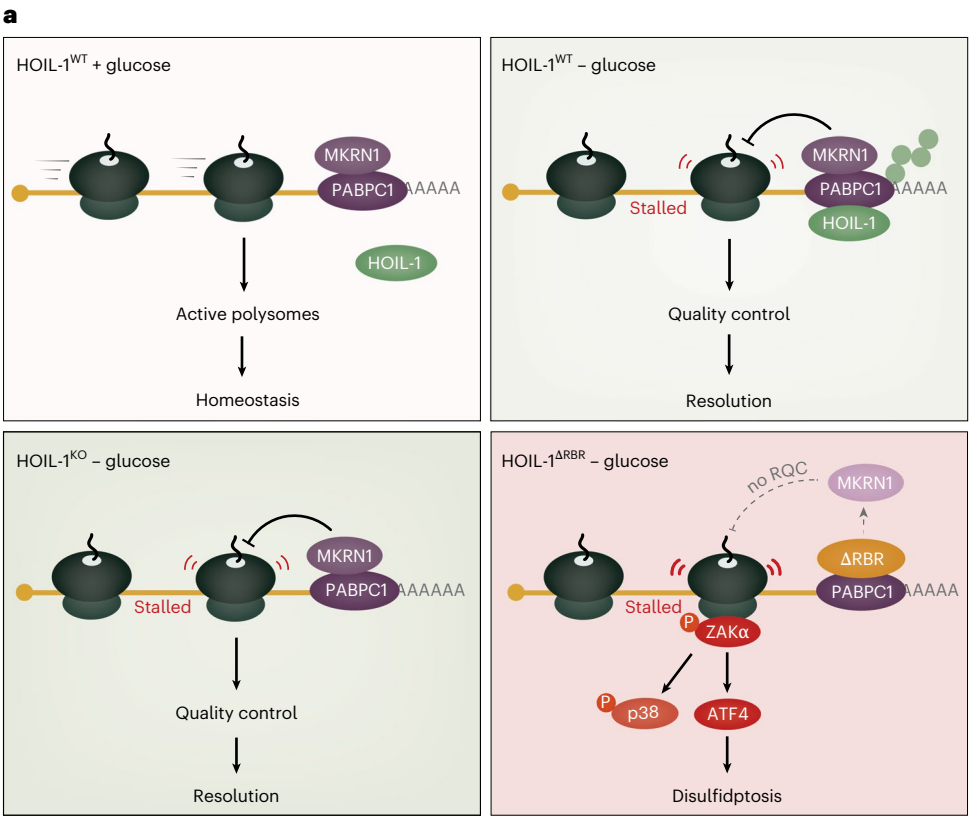

Fig. 8 | HOIL-1, PABPC1 and MKRN1 suppress ZAKα-driven disulfidptosis during glucose starvation. a, The proposed model. Cells in full glucose medium are in homeostasis. During glucose starvation in WT cells, HOIL-1 binds and ubiquitinates PABPC1, which resolves stress and stalled ribosomes by facilitating quality control via MKRN1. In HOIL-1^{KO} cells, MKRN1 retains PABPC1 binding and quality control is unaffected. HOIL-1$^{\Delta RBR}$ acts as a dominant-negative by binding to PABPC1 and excluding MKRN1 from the complex. Unresolved stalled ribosomes in HOIL-1$^{\Delta RBR}$ cells activate ZAKα, which promotes p38 phosphorylation and ATF4 translation, leading to disulfidptosis.

If ΔRBR HOIL-1 is acting as a dominant-negative, we reasoned we could override its effects by altering the stoichiometry of PABPC1 or MKRN1. Indeed, PABPC1 overexpression shut down ATF4 in response to glucose starvation but not sodium arsenite (Fig. 7g) and protected against disulfidptosis but not amino acid starvation-induced cell death (Extended Data Fig. 10e). Glucose starvation-induced ribotoxic stress was potently quelled by PABPC1 overexpression (Fig. 7h). Overexpression of WT MKRN1, but not the catalytically inactive H307E mutant, likewise suppressed glucose starvation-induced ZAKα activation, ATF4 and cell death (Fig. 7i,j) but had no effect on amino acid starvation (Extended Data Fig. 10f). Critically, the canonical RQC E3 ligase, ZNF598, could not rescue cell death upon overexpression (Fig. 7i). Consistent with our overexpression data, silencing PABPC1 or MKRN1, but not ZNF598, enhanced ATF4 and phospho-p38 levels during glucose starvation (Fig. 7k), particularly in HOIL-1^{KO} cells. These data demonstrate that PABPC1 and MKRN1 limit the RSR during glucose starvation. Failure of this quality control system in HOIL-1$^{\Delta RBR}$ cells precipitates a ZAKα–ATF4-driven stress response that kills the cell via disulfidptosis (Fig. 8).

Discussion

Selective autophagy of glycogen particles via glycophagy plays an important role in cardiac metabolic stress[79] and diabetic cardiomyopathy[80]. As HOIL-1 can directly ubiquitinate glycogen in vitro[24,81,82], our data support the compelling hypothesis that HOIL-1 promotes glycophagy by tagging glycogen particles for clearance. The inability of cardiomyocytes in HOIL-1$^{\Delta RBR}$ mice to breakdown glycogen may disrupt the adaptive metabolic changes needed to mitigate pressure overload, thereby accelerating pathology. Indeed, glycogen aggregates were observed in HOIL-1$^{\Delta RBR}$ cardiomyocytes only after pressure overload was induced (Fig. 1h). Impaired glycogen breakdown, as in Danon disease and Pompe disease[83], or excessive glycogen deposition, as in PRKAG2 syndrome[84], commonly manifests as cardiomyopathy. We propose that these metabolic perturbations also cause ribosomal stress. It remains to be determined whether disulfidptosis, which is exacerbated by insufficient glycogen reserves[50], contributes to cardiac pathology in vivo.

Male, but not female, HOIL-1$^{\Delta RBR}$ mice had exacerbated cardiomyocyte cellular hypertrophy and LV dilatation following LV pressure overload. While there is no known sex bias in PGBM1[14], it is notable that ZAK-deficient mice also present sex-biased metabolic phenotypes. Male ZAK$^{-/-}$ mice are slightly leaner than WT mice, while females have similar body mass[3]. Further, male ZAK$^{-/-}$ mice are protected against ageing-associated metabolic dysfunction while females are not[4]. There is also prior evidence that ZAKα contributes to cardiac pathophysiology. ZAKα was first cloned from a cDNA library derived from a failing human heart in search of regulators of cardiac hypertrophy[85]. ZAKα is abundantly expressed in cardiomyocytes[86] and, when overexpressed, promotes hypertrophy of cardiac myoblasts[87]. Transgenic overexpression of the ZAKβ isoform in cardiomyocytes causes spontaneous cardiac fibrosis and accelerated mortality in response to isoproterenol-induced hypertrophy[88], and a selective ZAKα inhibitor protected against hypertrophic cardiomyopathy in a spontaneous hypertensive rat model[89]. Although we lack direct evidence, we speculate that sex-specific ZAKα activity may in part drive cardiac hypertrophy in HOIL-1$^{\Delta RBR}$ mice. Future studies will address this important question.

Cells are equipped with multiple translation surveillance mechanisms, as different problems require different solutions. The nature

and location of the problematic mRNA or ribosome determine which system is deployed to resolve the issue[90–93]. For example, a recent study demonstrates ZNF598 responds to ribosome collisions specifically at the start site during translation initiation in stem cells[94]. Intriguingly, they show that a ZNF598^{RING} mutant acts as a dominant-negative that causes differential ISR activation relative to full ZNF598 loss, similar to what we report here with HOIL-1. In our work, we did not observe a role for ZNF598 in the glucose starvation response. During amino acid starvation and oxidative stress, ribosomes stall towards the start codon, while during glucose starvation they stall towards the stop codon[95]. Given that MKRN1 and PABPC1 reside at poly(A) tails and A-rich stretches of 3′ UTRs[77], our data support the existence of a distinct quality-control response that surveils ribosome stalling towards the site of translation termination. Characterizing the molecular mechanisms of this surveillance system is an important area for further investigation.

Ribosomes are massive macromolecular assemblies. Beyond their textbook roles in protein translation, their vast surfaces also serve as signalling platforms where information about the cellular metabolic state can be encoded and transduced. The language of ubiquitin is well-suited for this. Decoding this information and understanding how E3 ligases and deubiquitinases collaborate in this context will be of great interest. Advances in techniques to detect non-canonical ubiquitin modifications, such as HOIL-1-mediated ester-linked ubiquitin, will undoubtedly reveal additional layers of regulation of ribosomal stress signalling.

Online content

Any methods, additional references, Nature Portfolio reporting summaries, source data, extended data, supplementary information, acknowledgements, peer review information; details of author contributions and competing interests; and statements of data and code availability are available at https://doi.org/10.1038/s41556-026-01936-6.

References

1. Costa-Mattioli, M. & Walter, P. The integrated stress response: from mechanism to disease. *Science* **368**, eaat5314 (2020).
2. Wu, C. C., Peterson, A., Zinshteyn, B., Regot, S. & Green, R. Ribosome collisions trigger general stress responses to regulate cell fate. *Cell* **182**, 404–416 (2020).
3. Snieckute, G. et al. Ribosome stalling is a signal for metabolic regulation by the ribotoxic stress response. *Cell Metab.* **34**, 2036–2046 (2022).
4. Snieckute, G. et al. ROS-induced ribosome impairment underlies ZAKα-mediated metabolic decline in obesity and aging. *Science* **382**, eadf3208 (2023).
5. Boisson, B. et al. Immunodeficiency, autoinflammation and amylopectinosis in humans with inherited HOIL-1 and LUBAC deficiency. *Nat. Immunol.* **13**, 1178–1186 (2012).
6. Nilsson, J. et al. Polyglucosan body myopathy caused by defective ubiquitin ligase RBCK1. *Ann. Neurol.* **74**, 914–919 (2013).
7. Wang, K. et al. Whole-genome DNA/RNA sequencing identifies truncating mutations in RBCK1 in anovel Mendelian disease with neuromuscular and cardiac involvement. *Genome Med.* **5**, 1–8 (2013).
8. Krenn, M. et al. Mutations outside the N-terminal part of RBCK1 may cause polyglucosan body myopathy with immunological dysfunction: expanding the genotype–phenotype spectrum. *J. Neurol.* **265**, 394–401 (2018).
9. Phadke, R. et al. RBCK1-related disease: a rare multisystem disorder with polyglucosan storage auto-inflammation recurrent infections skeletal AND cardiac myopathy—four additional patients AND a review of the current literature. *J. Inherit. Metab. Dis.* **43**, 1002–1013 (2020).
10. AlAnzi, T., Al Harbi, F., AlGhamdi, A. & Mohamed, S. A novel variant of RBCK1 gene causes mild polyglucosan myopathy. *Neurosciences* **27**, 45–49 (2022).
11. Maurer, C. et al. Genetic insights from consanguineous cardiomyopathy families. *Genes* **14**, 1–11 (2023).
12. Pühringer, M., Eisenkölbl, A. & Gröppel, G. Expanding the phenotype of RBCK1-associated polyglucosan body myopathy type 1. *Mol. Genet. Metab. Rep.* **38**, 101031 (2024).
13. MozafaryBazargany, M. et al. A novel likely pathogenic homozygous RBCK1 variant in dilated cardiomyopathy with muscle weakness. *ESC Heart Fail.* **11**, 1472–1482 (2024).
14. Sun, Q., Xie, Z., Song, L. & Fu, D. A case of polyglucosan body myopathy caused by an RBCK1 gene variant and literature review. *Mol. Genet. Genomic Med.* **12**, e2432 (2024).
15. Ikeda, F. et al. SHARPIN forms a linear ubiquitin ligase complex regulating NF-κB activity and apoptosis. *Nature* **471**, 637–641 (2011).
16. Sasaki, Y. et al. Defective immune responses in mice lacking LUBAC-mediated linear ubiquitination in B cells. *EMBO J.* **32**, 2463–2476 (2013).
17. Boisson, B. et al. Human HOIP and LUBAC deficiency underlies autoinflammation, immunodeficiency, amylopectinosis, and lymphangiectasia. *J. Exp. Med.* **212**, 939–951 (2015).
18. Okamura, K. et al. Survival of mature T cells depends on signaling through HOIP. *Sci. Rep.* **6**, 36135 (2016).
19. Teh, C. E. et al. Linear ubiquitin chain assembly complex coordinates late thymic T-cell differentiation and regulatory T-cell homeostasis. *Nat. Commun.* **7**, 13353 (2016).
20. Wang, J. et al. LUBAC suppresses IL-21-induced apoptosis in CD40-activated murine B cells and promotes germinal center B cell survival and the T-dependent antibody response. *Front. Immunol.* **12**, 658048 (2021).
21. Jain, R. et al. Dual roles for LUBAC signaling in thymic epithelial cell development and survival. *Cell Death Differ.* **28**, 2946–2956 (2021).
22. Fuseya, Y. et al. Attenuation of HOIL-1L ligase activity promotes systemic autoimmune disorders by augmenting linear ubiquitin signaling. *JCI Insight* **9**, e171108 (2024).
23. Oda, H. et al. Biallelic human SHARPIN loss of function induces autoinflammation and immunodeficiency. *Nat. Immunol.* **25**, 764–777 (2024).
24. Kelsall, I. R. et al. HOIL-1 ubiquitin ligase activity targets unbranched glucosaccharides and is required to prevent polyglucosan accumulation. *EMBO J.* **41**, e109700 (2022).
25. Kelsall, I. R., Zhang, J., Knebel, A., Arthur, J. S. C. & Cohen, P. The E3 ligase HOIL-1 catalyses ester bond formation between ubiquitin and components of the Myddosome in mammalian cells. *PNAS* **116**, 13293–13298 (2019).
26. Petrova, T., Zhang, J., Nanda, S. K., Figueras-Vadillo, C. & Cohen, P. HOIL-1-catalysed, ester-linked ubiquitylation restricts IL-18 signaling in cytotoxic T cells but promotes TLR signalling in macrophages. *FEBS J.* **288**, 5909–5924 (2021).
27. McCrory, E. H., Akimov, V., Cohen, P. & Blagoev, B. Identification of ester-linked ubiquitylation sites during TLR7 signalling increases the number of inter-ubiquitin linkages from 8 to 12. *Biochem. J.* **479**, 2419–2431 (2022).
28. Peltzer, N. et al. LUBAC is essential for embryogenesis by preventing cell death and enabling haematopoiesis. *Nature* **557**, 112–117 (2018).
29. Tokunaga, F. et al. Involvement of linear polyubiquitylation of NEMO in NF-kappaB activation. *Nat. Cell Biol.* **11**, 123–132 (2009).
30. Fujita, H. et al. Cooperative Domain formation by homologous motifs in HOIL-1L and SHARPIN plays a crucial role in LUBAC stabilization. *Cell Rep.* **23**, 1192–1204 (2018).

31. Fuseya, Y. et al. The HOIL-1L ligase modulates immune signalling and cell death via monoubiquitination of LUBAC. *Nat. Cell Biol.* **22**, 663–673 (2020).
32. Altman, B. J. & Rathmell, J. C. Metabolic stress in autophagy and cell death pathways. *Cold Spring Harb. Perspect. Biol.* **4**, a008763 (2012).
33. Olivetti, G. et al. Apoptosis in the failing human heart. *New Engl. J. Med.* **336**, 1131–1141 (1997).
34. Guerra, S. et al. Myocyte death in the failing human heart is gender dependent. *Circ. Res.* **85**, 856–866 (1999).
35. Wencker, D. et al. A mechanistic role for cardiac myocyte apoptosis in heart failure. *J. Clin. Invest.* **111**, 1497–1504 (2003).
36. Whelan, R. S., Kaplinskiy, V. & Kitsis, R. N. Cell death in the pathogenesis of heart disease: mechanisms and significance. *Annu. Rev. Physiol* **72**, 19–44 (2010).
37. Gao, L. et al. The mechanism of linear ubiquitination in regulating cell death and correlative diseases. *Cell Death Dis.* **14**, 659 (2023).
38. Koppula, P., Zhang, Y., Shi, J., Li, W. & Gan, B. The glutamate/cystine antiporter SLC7A11/xCT enhances cancer cell dependency on glucose by exporting glutamate. *J. Biol. Chem.* **292**, 14240–14249 (2017).
39. Xu, W. et al. Comprehensive multi-omics identification of interferon-γ response characteristics reveals that RBCK1 regulates the immunosuppressive microenvironment of renal cell carcinoma. *Front. Immunol.* **12**, 734646 (2021).
40. Katsuya, K. et al. Small-molecule inhibitors of linear ubiquitin chain assembly complex (LUBAC), HOIPINs, suppress NF-κB signaling. *Biochem. Biophys. Res. Commun.* **509**, 700–706 (2019).
41. Damgaard, R. B. et al. The deubiquitinase OTULIN is an essential negative regulator of inflammation and autoimmunity. *Cell* **166**, 1215–12301 (2016).
42. Damgaard, R. B. et al. OTULIN deficiency in ORAS causes cell type-specific LUBAC degradation, dysregulated TNF signalling and cell death. *EMBO Mol. Med.* **11**, e9324 (2019).
43. Caro-Maldonado, A. et al. Glucose deprivation induces an atypical form of apoptosis mediated by caspase-8 in Bax-, Bak-deficient cells. *Cell Death Differ.* **17**, 1335–1344 (2010).
44. Iurlaro, R. et al. Glucose deprivation induces ATF4-mediated apoptosis through TRAIL death receptors. *Mol. Cell. Biol.* **37**, e00479–16 (2017).
45. Bialik, S. et al. The mitochondrial apoptotic pathway is activated by serum and glucose deprivation in cardiac myocytes. *Circ. Res.* **85**, 403–414 (1999).
46. León-Annicchiarico, C. L. et al. ATF4 mediates necrosis induced by glucose deprivation and apoptosis induced by 2-deoxyglucose in the same cells. *FEBS J.* **282**, 3647–3658 (2015).
47. Ding, B. et al. Sestrin2 is induced by glucose starvation via the unfolded protein response and protects cells from non-canonical necroptotic cell death. *Sci. Rep.* **6**, 22538 (2016).
48. Baik, J. Y. et al. ZBP1 not RIPK1 mediates tumor necroptosis in breast cancer. *Nat. Commun.* **12**, 2666 (2021).
49. Hamann, J. C. et al. Entosis is induced by glucose starvation. *Cell Rep.* **20**, 201–210 (2017).
50. Liu, X. et al. Actin cytoskeleton vulnerability to disulfide stress mediates disulfidptosis. *Nat. Cell Biol.* **25**, 404–414 (2023).
51. Liu, X. et al. Cystine transporter regulation of pentose phosphate pathway dependency and disulfide stress exposes a targetable metabolic vulnerability in cancer. *Nat. Cell Biol.* **22**, 476–486 (2020).
52. Liu, X., Zhang, Y., Zhuang, L., Olszewski, K. & Gan, B. NADPH debt drives redox bankruptcy: SLC7A11/xCT-mediated cystine uptake as a double-edged sword in cellular redox regulation. *Gene. Dis* **8**, 731–745 (2021).
53. Ghergurovich, J. M. et al. A small molecule G6PD inhibitor reveals immune dependence on pentose phosphate pathway. *Nat. Chem. Biol.* **16**, 731–739 (2020).
54. Cracan, V., Titov, D. V., Shen, H., Grabarek, Z. & Mootha, V. K. A genetically encoded tool for manipulation of NADP(+)/NADPH in living cells. *Nat. Chem. Biol.* **13**, 1088–1095 (2017).
55. Kreß, J. K. C. et al. The integrated stress response effector ATF4 is an obligatory metabolic activator of NRF2. *Cell Rep.* **42**, 112724 (2023).
56. Foronda, H. et al. Heteromeric clusters of ubiquitinated ER-shaping proteins drive ER-phagy. *Nature* **618**, 402–410 (2023).
57. Forrester, A. et al. A selective ER-phagy exerts procollagen quality control via a calnexin–FAM134B complex. *EMBO J.* **38**, e99847 (2019).
58. Chino, H., Hatta, T., Natsume, T. & Mizushima, N. Intrinsically disordered protein TEX264 mediates ER-phagy. *Mol. Cell* **74**, 909–921 (2019).
59. Liang, J. R. et al. A genome-wide ER-phagy screen highlights key roles of mitochondrial metabolism and ER-resident UFMylation. *Cell* **180**, 1160–1177 (2020).
60. An, H. & Harper, J. W. Systematic analysis of ribophagy in human cells reveals bystander flux during selective autophagy. *Nat. Cell Biol.* **20**, 135–143 (2018).
61. Juszkiewicz, S. & Hegde, R. S. Initiation of quality control during poly(A) translation requires site-specific ribosome ubiquitination. *Mol. Cell* **65**, 743–750 (2017).
62. Matsuo, Y. et al. Ubiquitination of stalled ribosome triggers ribosome-associated quality control. *Nat. Commun.* **8**, 159 (2017).
63. Meydan, S. & Guydosh, N. R. A cellular handbook for collided ribosomes: surveillance pathways and collision types. *Curr. Genet.* **67**, 19–26 (2021).
64. Yan, L. L. & Zaher, H. S. Ribosome quality control antagonizes the activation of the integrated stress response on colliding ribosomes. *Mol. Cell* **81**, 614–628 (2021).
65. Sinha, N.K. et al. The ribotoxic stress response drives UV-mediated cell death. *Cell* **187**, 3652–3670 (2024).
66. Ikeuchi, K. et al. Collided ribosomes form a unique structural interface to induce Hel2-driven quality control pathways. *EMBO J.* **38**, e100276 (2019).
67. Juszkiewicz, S. et al. ZNF598 is a quality control sensor of collided ribosomes. *Mol. Cell* **72**, 469–481 (2018).
68. Sinha, N. K. et al. EDF1 coordinates cellular responses to ribosome collisions. *eLife* **9**, e58828 (2020).
69. Juszkiewicz, S. et al. Ribosome collisions trigger *cis*-acting feedback inhibition of translation initiation. *eLife* **9**, e60038 (2020).
70. Hickey, K. L. et al. GIGYF2 and 4EHP inhibit translation initiation of defective messenger RNAs to assist ribosome-associated quality control. *Mol. Cell* **79**, 950–962 (2020).
71. Wang, L. et al. UFMylation of RPL26 links translocation-associated quality control to endoplasmic reticulum protein homeostasis. *Cell Res.* **30**, 5–20 (2020).
72. Arthur, L. et al. Translational control by lysine-encoding A-rich sequences. *Sci. Adv.* **1**, e1500154 (2015).
73. Craig, A. W., Haghighat, A., Yu, A. T. & Sonenberg, N. Interaction of polyadenylate-binding protein with the eIF4G homologue PAIP enhances translation. *Nature* **392**, 520–523 (1998).
74. Kahvejian, A., Svitkin, Y. V., Sukarieh, R., M'Boutchou, M. N. & Sonenberg, N. Mammalian poly(A)-binding protein is a eukaryotic translation initiation factor, which acts via multiple mechanisms. *Genes Dev.* **19**, 104–113 (2005).
75. Yi, H. et al. PABP cooperates with the CCR4–NOT complex to promote mRNA deadenylation and block precocious decay. *Mol. Cell* **70**, 1081–1088 (2018).

76. Webster, M. W. et al. mRNA deadenylation is coupled to translation rates by the differential activities of Ccr4-Not nucleases. *Mol. Cell* **70**, 1089–1100 (2018).
77. Hildebrandt, A. et al. The RNA-binding ubiquitin ligase MKRN1 functions in ribosome-associated quality control of poly(A) translation. *Genome Biol.* **20**, 1–20 (2019).
78. Szczesna, M. et al. Bacterial esterases reverse lipopolysaccharide ubiquitylation to block host immunity. *Cell Host Microbe* **32**, 913–924 (2024).
79. Reichelt, M. E., Mellor, K. M., Curl, C. L., Stapleton, D. & Delbridge, L. M. Myocardial glycophagy – a specific glycogen handling response to metabolic stress is accentuated in the female heart. *J. Mol. Cell. Cardiol.* **65**, 67–75 (2013).
80. Mellor, K. M. et al. Myocardial glycophagy flux dysregulation and glycogen accumulation characterize diabetic cardiomyopathy. *J. Mol. Cell. Cardiol.* **189**, 83–89 (2024).
81. Wu, Q., Koliopoulos, M. G., Rittinger, K. & Stieglitz, B. Structural basis for ubiquitylation by HOIL-1. *Front. Mol. Biosci.* **9**, 1098144 (2022).
82. Wang, X. S. et al. The unifying catalytic mechanism of the RING-between-RING E3 ubiquitin ligase family. *Nat. Commun.* **14**, 168 (2023).
83. Arad, M. et al. Glycogen storage diseases presenting as hypertrophic cardiomyopathy. *New Engl. J. Med.* **352**, 362–372 (2005).
84. Arad, M. et al. Constitutively active AMP kinase mutations cause glycogen storage disease mimicking hypertrophic cardiomyopathy. *J. Clin. Investig.* **109**, 357–362 (2002).
85. Bloem, L. J. et al. Tissue distribution and functional expression of a cDNA encoding a novel mixed lineage kinase. *J. Mol. Cellular Cardiol.* **33**, 1739–1750 (2001).
86. Liu, T. C. et al. Cloning and expression of ZAK, a mixed lineage kinase-like protein containing a leucine-zipper and a sterile-alpha motif. *Biochem. Biophys. Res. Commun.* **274**, 811–816 (2000).
87. Huang, C. Y. et al. ZAK re-programs atrial natriuretic factor expression and induces hypertrophic growth in H9c2 cardiomyoblast cells. *Biochem. Biophys. Res. Commun.* **324**, 973–980 (2004).
88. Christe, M. et al. Transgenic mice with cardiac-specific over-expression of MLK7 have increased mortality when exposed to chronic beta-adrenergic stimulation. *J. Mol. Cellular Cardiol.* **37**, 705–715 (2004).
89. Yang, J. et al. Design, synthesis, and structure-activity relationships of 1,2,3-triazole benzenesulfonamides as new selective leucine-zipper and sterile-α motif kinase (ZAK) inhibitors. *J. Med. Chem.* **63**, 2114–2130 (2020).
90. Garshott, D. M. et al. iRQC, a surveillance pathway for 40S ribosomal quality control during mRNA translation initiation. *Cell Rep.* **36**, 109642 (2021).
91. Phillips, B. P. & Miller, E. A. Ribosome-associated quality control of membrane proteins at the endoplasmic reticulum. *J. Cell Sci.* **133**, jcs251983 (2020).
92. Gurzeler, L. A. et al. Drug-induced eRF1 degradation promotes readthrough and reveals a new branch of ribosome quality control. *Cell Rep.* **42**, 113056 (2023).
93. Oltion, K. et al. An E3 ligase network engages GCN1 to promote the degradation of translation factors on stalled ribosomes. *Cell* **186**, 346–362 (2023).
94. Rodschinka, G. et al. Comparative CRISPRi screens reveal a human stem cell dependence on mRNA translation-coupled quality control. *Nat. Struct. Mol. Biol.* **32**, 1932–1946 (2025).
95. Guzikowski, A. R. et al. Differential translation elongation directs protein synthesis in response to acute glucose deprivation in yeast. *RNA Biol.* **19**, 636–649 (2022).

Methods

All animal procedures were reviewed by the Institutional Animal Care and Use Committees at Yale University under protocol nos. 10019 and 07788 and comply with all relevant ethical regulations.

Key resources table

A key resources table is provided in Supplementary Table 5 and provides a detailed overview of catalogue numbers. Further details can be found in the Nature Portfolio Reporting Summary linked to this Article.

Mice

Mice were maintained in a pathogen-free facility on a 12 h light, 12 h dark cycle with ad libitum food and water. Mice were fed standard chow diet (Teklad Global 18% Protein Rodent Diet). All breeding animals were heterozygous for the *Rbck1* null allele, as in the study by Tokunaga et al.[29], and had been previously backcrossed to a C57BL/6 background more than nine times. Age-matched male and female *Rbck1*$^{+/+}$ and *Rbck1*$^{null/null}$ littermates were used in all experiments.

Cell lines

AC16 cells were cultured in DMEM/F12, HEPES (Gibco, 11320033) supplemented with 10% FBS, HEK293T (female) cells and MEFs were cultured in DMEM (Gibco, 11995065) supplemented with 10% FBS and 786-O cells (male) were cultured in RPMI 1640 (Gibco, 11875093) supplemented with 10% FBS and 1% penicillin–streptomycin. All cell lines were maintained at 37 °C with 5% CO_2. AC16 cells were a kind gift from Iain Scott (UPMC). HEK293T and 786-O cells were obtained from American Type Culture Collection. HOIL-1$^{\Delta RING1}$ MEFs were previously generated[31]. All cell lines were routinely tested for *Mycoplasma*.

TAC

TAC was performed on mice at approximately 10 weeks of age in mice using a minimally invasive approach[96]. After anaesthesia with ketamine (100 mg kg^{-1}) and xylazine (10 mg kg^{-1}), a skin incision 0.5–1.0 cm in length was made at the level of the suprasternal notch, and a longitudinal cut 2–3 mm in length was made in the proximal portion of the sternum. This allowed for visualization of the aortic arch without opening the pleural space. A 27-gauge needle was placed next to the aortic arch to calibrate the constriction and an 8-0 suture was tied. Following ligation, the needle was removed. The skin was closed and mice were allowed to recover on a warming pad until they were fully awake.

Echocardiography

Mice were anaesthetised with 1.5% isoflurane and 1.5% oxygen and kept on a heated platform during imaging. Echocardiography was performed with a Visual Sonics Vevo2100 ultrasound with a 40-mHz probe. Standard echo views were obtained of the left ventricle and of the aortic arch.

Histology

Mouse hearts were fixed in 4% paraformaldehyde for 24 h at 4 °C, then stored in 70% ethanol for an additional 48 h. Then, 5 µm sections were cut and parrafin-embedded. Sections were stained with hematoxylin and eosin (H&E), Masson's Trichrome, periodic acid–Schiff and TUNEL using standard histochemical procedure. Cardiomyocyte cross-sectional area and width were calculated using the CmyoSize macro for Fiji/ImageJ[97]. Five randomly selected regions of interest from H&E-stained heart sections at 40× magnification were used per mouse. Glycogen aggregates were quantified using a Fiji/ImageJ macro using five randomly selected regions from periodic acid–Schiff-stained heart sections at 20× magnification per mouse.

Molecular biology

All plasmid subcloning was done using the In-Fusion Snap Assembly Kit (Takara Bio, 638947). Site-directed mutagenesis was done using QuikChange XL (Agilent, 200517). See Supplementary Table 6 for a list of plasmids used and generated in this study.

Lentivirus generation and transduction for stable cell line generation

First, 5×10^5 HEK293T cells were seeded on poly-L-lysine-coated six-well plates in 2 ml DMEM + 10% FBS. The following day, cells were transfected with 1.5 µg psPAX2, 0.5 µg pMD2.G and 2.0 µg transfer vector per well using Lipofectamine 2000 according to the manufacturer's protocol. Media was changed 8 h after transfection. Media containing lentivirus was collected every 24 h and stored at 4 °C. After 72 h, pooled lentiviral media was filtered through a 0.45-µm mixed cellulose esters filter (Millipore). Target cells were transduced in six-well plates at 30–40% confluence with 1 ml lentiviral media containing 8 µg ml^{-1} polybrene. Media were replaced after 24 h. The appropriate selection antibiotic was added to transduced cells 48 h post-transduction. After 7–10 days of selection, transduced cells were expanded and stocks were frozen down, followed by maintenance in a half dose of the selection antibiotic. No antibiotics were included in the media for experiments.

KO cell line generation

For CRISPR-Cas9 gene editing, single guide RNA sequences were chosen using CHOPCHOP[98] and cloned into either lentiCRISPRv2-puro (Addgene, 52961) or lentiCRISPRv2-hygro (Addgene, 98291) according to the Feng Zhang laboratory protocol. Target cells were transduced as above. Following selection, cells were reseeded in three 96-well plates per cell line using limiting dilution. Single cell-derived colonies were expanded, and KO efficiency was validated by immunoblot. Multiple successfully edited clones per cell line were tested in initial experiments.

Cell treatment and starvation

Cells were seeded such that they were at approximately 70% confluence at the time of treatment or starvation. For starvation experiments, cells were seeded on poly-L-lysine-coated plates to minimize cell loss during washes. To starve, medium was aspirated and cells were washed twice quickly and gently with pre-warmed PBS, and either glucose-free DMEM (Gibco, 11966025) supplemented with 10% dialyzed FBS (Thermo Fisher, A3382001) or Earl's Balanced Salt Solution (Gibco, 24010043) was added for glucose or amino acid starvation, respectively. For cystine starvation, media were prepared using DMEM without L-glutamine, L-cystine, glucose, phenol red or sodium pyruvate (USBiological, D9815-25L), with 4 mM L-glutamine added. L-Cystine (Thermo Fisher, J61651.09) was added to a final concentration of 200 µM where indicated. Unless otherwise indicated, inhibitors or other supplements were added at the same time of starvation.

Transient gene silencing was achieved by reverse transfection of small interfering (siRNA) at a final concentration of 10 nM using RNAiMAX Lipofectamine (Invitrogen, 13778075) according to the manufacturer's protocol. All siRNA used were ON-TARGETplus SMARTpool siRNA from Horizon Discovery.

UV-C irradiation was performed using a UV crosslinker (Analytik Jena CL-1000) set to 254 nm for the indicated doses. Then, 1 h before irradiation, the medium was aspirated and cells were washed twice with pre-warmed PBS and replaced with phenol red-free DMEM/F12 (Gibco, 21041025) containing 10% FBS. Cells were elevated approximately 9 cm away from the lamp source for stimulation. The cell culture plate lid was removed during irradiation and quickly replaced, then cells were returned to the incubator for 24 h.

Glycogen quantification

First, 9×10^4 AC16 cells were seeded in poly-L-lysine-coated six-well plates in triplicate per condition. The following day, cells were pre-treated with glycogen phosphorylase inhibitor (Cayman, 17578) or dimethylsulfoxide (DMSO) vehicle control for 1 h before glucose

starvation for an additional 1 h, or left in DMEM/F12 + 10% FBS. Glycogen phosphorylase inhibitor or DMSO was included during starvation. After starvation, cells were placed on ice and quickly washed twice with 1 ml ice-cold PBS, scraped into 150 µl ice-cold ddH_2O and collected in 0.2-ml strip PCR tubes on ice. Then, 15 µl was reserved for protein quantification and the remainder was boiled for 30 min at 98 °C. After boiling, samples were spun down and diluted 1:10 with ddH_2O. Glycogen was quantified using the Glycogen Assay Kit (Sigma, MAK016) with slight modifications: (1) the Hydrolysis Enzyme Mix was used at half the recommended concentration, (2) the Development Enzyme Mix was used at a third of the recommended concentration and (3) the Fluorescent Peroxidase Substrate was diluted 1:10. Glycogen content was normalized to protein concentration. The data are presented as percentages of glycogen measured in full media.

Immunoblotting

When collecting lysates for direct immunoblot analysis, media and dead cells were aspirated, and adherent cells were quickly washed with 1 ml ice-cold PBS. After removing all PBS, cells were scraped directly into a modified Laemmli buffer (62.5 mM Tris–HCl pH 6.8, 15% glycerol, 2% SDS and 0.025% bromophenol blue) containing 5% freshly added 2-mercaptoethanol (2-ME). Samples were boiled for 5 min at 95 °C followed by vigorous vortexing to reduce viscosity. Samples were resolved on 4–15% or 4–20% Criterion TGX pre-cast Midi gels (Bio-Rad, 5671085 or 5671095) at a 90 V constant voltage, followed by transfer onto 0.45-µm or 0.2-µm nitrocellulose membranes using the Trans-Blot Turbo Transfer System (Bio-Rad). Membranes were quickly washed with distilled water and blocked with 5% milk in 0.1% TBS-Tween for 1 h at room temperature, followed by overnight incubation at 4 °C in primary antibody diluted in either 5% milk in 0.1% TBS-Tween or 5% bovine serum album in 0.1% TBS-Tween. Membranes were washed 4 × 10 min in 0.1% TBS-Tween, followed by incubation with HRP-conjugated secondary antibodies in 5% milk in 0.1% TBS-Tween for 1 h at room temperature. Membranes were washed 4 × 10 min in 0.1% Tween and the signal was detected using Amersham ECL Detection Reagents (Cytiva, RPN2105) or Super Signal West Femto (Thermo Fisher, 34095) with a ChemiDoc imaging system (Bio-Rad).

To examine ZAKα phosphorylation, samples were resolved on 7% acrylamide gels containing 10.7 µM Phos-Tag (Wako, AAL-107) and 21.3 µM $MnCl_2$ (as in the study by Wu et al.[2]) and processed as above.

RT–qPCR

For reverse transcription quantitative polymerase chain reactions (RT–qPCR), total RNA was extracted using TRIzol reagent (Thermo Fisher, 15596026) according to the manufacturer's protocol. First, 1 µg RNA was reverse transcribed using the High-Capacity cDNA Reverse Transcription Kit (Thermo Fisher, 4368814) according to the manufacturer's protocol. cDNA was diluted 1:5 in nuclease-free water and 2 µl was mixed with 10 µl 2× SYBR Select MasterMix (Thermo Fisher, 4472908) and 250 nM forward and reverse qPCR primers in a 20 µl final volume per sample. Thermocycling was according to the manufacturer's protocol. Following normalization to the housekeeping gene *TBP*, fold induction was calculated using the $2^{-\Delta\Delta Ct}$ method. See Supplementary Table 7 for primer sequences.

Immunoprecipitation

To examine PABPC1 ubiquitination, 2.0×10^6 HEK293T cells were seeded in poly-L-lysine-coated 10-cm dishes, one plate per sample. The following day, cells were transfected with 2 µg of each plasmid, normalizing the total DNA payload with pCMV-Flag empty vector, using Lipofectamine 2000 at a 3:1 Lipofectamine:DNA ratio. Cells were harvested by trypsinization, centrifuged at 300*g* for 5 min at 4 °C, and cell pellets were washed with 2 × 10 ml ice-cold PBS. Cell pellets were subjected to hot lysis by resuspending in 100 µl ubiquitin lysis buffer (1% SDS, 50 mM Tris–HCl pH 7.5, 150 mM NaCl and 5 mM EDTA) containing a protease inhibitor and 50 µM PR-619 (Cayman Chemical, 16276) using a wide bore pipette tip, followed by boiling for 15 min at 95 °C with intermittent trituration. After boiling, samples were diluted 1:10 with Buffer G (1% Triton, 50 mM Tris–HCl pH 7.5 and 150 mM NaCl) containing a protease inhibitor and PR-619 and passed through a 22-G syringe until homogenous (~5–10 strokes). Lysates were clarified at 21,000*g* for 15 min at 4 °C. Then, 15 µl GFP-Trap magnetic agarose beads (Proteintech gtma) were washed three times in 500 µl ice-cold dilution buffer and added to 500 µg of the lysate. Samples were rotated for 1 h at 4 °C, then washed four times with wash buffer (10 mM Tris–HCl, 150 mM NaCl, 0.5 mM EDTA and 0.05% NP-40). Proteins were eluted by boiling in 40 µl Laemmli containing 10% 2-ME for 10 min and subject to immunoblot analysis.

For endogenous PABPC1 co-immunoprecipitation, 1.6×10^6 AC16 cells were seeded in poly-L-lysine-coated 15-cm dishes, five plates per sample. The following day, cells were starved of glucose for 6 h as above. Adherent cells were collected by trypsinization and centrifuged at 300*g* for 5 min at 4 °C. Cell pellets were washed twice with 50 ml ice-cold PBS, then lysed in 1 ml lysis buffer (10 mM Tris–HCl, 150 mM NaCl, 1.0 mM EDTA, 0.5% NP-40 and fresh protease inhibitor) and left on ice for 30 min with intermittent gentle vortexing. The same 1 ml was used to harvest all five plates of a sample. Lysates were clarified at 21,000*g* for 15 min at 4 °C. For each sample, 4 µg anti-PABPC1 (Proteintech, 10970-1-AP) or rabbit IgG isotype control (Cell Signaling Technology, 3900S) was added to 50 µl washed Dynabeads Protein G beads (Invitrogen, 10003D) in 1.5 ml LoBind tubes (Eppendorf, 022431081) containing 200 µl PBS + 0.02% Tween, mixed well and rotated at room temperature for 40 min. Antibody–bead complexes were washed with 200 µl 0.02% PBS-Tween, and 2 mg of lysate in a 1 ml final volume was added and rotated overnight at 4 °C. Beads were washed four times with 200 µl ice-cold 0.02% PBS-Tween and transferred to a clean tube with the last wash. Proteins were eluted by boiling in 40 µl Laemmli containing 10% 2-ME for 10 min and subjected to immunoblot analysis.

RNA granule fractionation

Fractionation was performed as in ref. 99. In brief, 9×10^5 (for 24 h glucose starvation) or 4.5×10^5 (for untreated, 8 h glucose starvation and sodium arsenite treatment) AC16 cells were seeded in poly-L-lysine-coated 15-cm dishes, three plates per sample. The 24 h glucose starvation was initiated when cells reached 80% confluence. The following day, cells were starved of glucose for 8 h, treated with 0.5 mM sodium arsenite for 1 h in complete medium or left untreated. After treatment, media was aspirated and cells were washed twice with 10 ml ice-cold PBS, then scraped into 1 ml ice-cold Buffer L (50 mM Tris pH 7.5, 50 mM NaCl, 5 mM $MgCl_2$, 0.1% NP-40, fresh 1 mM 2-ME, 100 U ml^{-1} RNase inhibitor (Sigma, 3335402001) and protease and phosphatase inhibitors) and mechanically lysed by 30 strokes with a Dounce homogenizer on ice. The same 1 ml lysis buffer was used for all plates of a sample. Then, 50 µl was removed and mixed with 50 µl Laemmli buffer + 10% 2-ME as the whole cell extract fraction. The remaining 950 µl was centrifuged at 2,000*g* at 4 °C for 2 min. The resulting pellet (nuclear fraction) was washed once in 300 µl complete Buffer L then resuspended in 300–400 µl Laemmli + 5% 2-ME, while the supernatant was centrifuged again at 10,000*g* at 4 °C for 10 min. The resulting pellet (RNA granule fraction) was washed once in 300 µl complete Buffer L, then resuspended in 40–60 µl Laemmli + 5% 2-ME. The supernatant (cytosolic fraction) was mixed 1:1 with Laemmli + 10% 2-ME. All samples were frozen at −20 °C until immunoblot analysis.

Cell death analysis

To study cell death, cells were seeded in 12-well plates such that they were at 70% confluence at the time of starvation or treatment the following day (6×10^4 AC16 cells, 7×10^4 786-O cells and 3×10^4 MEFs). After the indicated treatment, cells were harvested by collecting the media containing floating cells in 5-ml round-bottom polystyrene tubes

(Corning, 352052). Adherent cells were washed once with room temperature PBS, trypsinized and pooled with the floating cells. Cells were centrifuged at 400*g* for 5 min at 4 °C. The supernatant was removed and cell pellets were resuspended in 250 µl PBS containing 5 µg ml^{-1} propidium iodide (Thermo Fisher, P3566) and stained for 15 min at room temperature in the dark. Samples were processed on a BD LSRFortessa X-20 Cell Analyzer.

MitoSOX Red staining

To assess mitochondrial superoxide levels, cells were stained with MitoSOX Red (Thermo Fisher, M36008). Briefly, 5 µM MitoSOX Red was added directly to media during the last 30 min of glucose starvation. Cells were then washed three times with Hank's Balanced Salt Solution and either trypsinized and processed by flow cytometry on a BD LSRFortessa X-20 Cell Analyzer or media was replaced with phenol red- and glucose-free DMEM (Thermo Fisher, A1443001) and imaged on an EVOS M5000 Imaging System (Invitrogen, AMF5000SV) using a 20× objective and Texas Red light cube.

LC–MS/MS global metabolomics

AC16 cells were seeded in Primaria six-well plates (Corning, 353846) such that they were at 70% confluence at time of starvation (1×10^5 cells per well for 24 h starvation and 6×10^4 cells per well for 3 h starvation) in sextuplicate in 2 ml DMEM/F12 supplemented with 10% FBS. Cells were starved by carefully aspirating media, washing cells twice with 1 ml room temperature D-PBS, then adding 2 ml pre-warmed DMEM without glucose, glutamine or phenol red (Thermo Fisher, A1443001) supplemented with 10% dialysed FBS and 4 mM L-glutamine. After starvation, plates were removed from the incubator one plate at a time and placed on ice. Media were aspirated and cells were washed quickly with 1 ml ice-cold 5 mM HEPES. Then, 150 µl ice-cold quenching buffer (20% methanol into 0.1% formic acid, 3 mM sodium fluoride and 5.5 µg ml^{-1} D8-phenylalanine) was added to each well. Cells were quickly scraped into quenching buffer and transferred to a pre-chilled V-bottom polypropylene plate (BD, 53263) on dry ice. Once all samples were collected, the plate was sealed with aluminium film (Bioexpress, T-3025-8B) and stored at −80 °C.

Cell lysates were lyophilized in the 96-well plate. Samples were prepared by resuspending the cell pellet in 50 µl 10% acetonitrile solution with D_4-taurine (25 µM) as a second internal standard. Subsequently, 5 µl of the supernatant was injected for each analysis mode on the mass spectrometer.

Chromatography. Two columns were used separately: a Thermo Scientific Hypercarb column (HC column; 100 × 4.6 mm, 3 µm) and a Phenomenex Kinetex F5 Core-shell LC column (RP column; 100 × 2.1 mm, 2.6 µm).

For the HC column, separations were performed with 1 ml min^{-1} linear gradients. Mobile phase A: 15 mM ammonium formate, 0.03% acetyl acetone and 0.1% formic acid. Mobile phase B: 60% acetonitrile, 35% isopropanol, 15 mM ammonium formate and 0.1% formic acid. The column temperature was 50 °C and the autosampler temperature was 5 °C.

For the RP column, separations were performed with 0.3 ml min^{-1} linear gradients. Mobile phase A: 95% water, 5% acetonitrile and 0.1% formic acid. Mobile phase B: 95% acetonitrile, 5% water and 0.1% formic acid. The column temperature was 30 °C and the autosampler temperature was 5 °C.

Mass spectrometry. Data were analysed using the Sciex TripleTOF 6600 and collected using an information-dependent analysis (IDA) workflow consisting of a time-of-flight mass spectrometry scan (200 ms) and a high-resolution IDA experiment (70 ms each) monitoring ten candidate ions per cycle. Former target ions were excluded after two occurrences for 5 s, and dynamic background subtraction was employed. The mass range for both time-of-flight mass spectrometry and IDA MS/MS scans was 60–1,000 with the RP column and 70–1,000 with the HC column.

The ion source conditions were as follows: ion spray voltage of 5,000 V for positive-mode coupling with the RP column and −4,500 V for negative-mode coupling with the HC column, ion source gas 1 of 50, ion source gas 2 of 50, curtain gas of 30 and temperatures of 400 °C with the RP column and 500 °C with the HC column. Compound dependent parameters for the two modes were a declustering potential of 35, a collision energy of 30 and a collision energy spread of 20.

Data processing. El-MAVEN software (Elucidata.io) was used for peak picking and curation from in-house targeted and untargeted libraries. Targeted libraries used the commercial standard kit of ~600 metabolites (IROA Technologies) in the two modes of analyses (the RP column positive ion acquisition mode and the HC column negative ion acquisition mode) yielding reference data (molecular ions and retention times) with wide coverage of the endogenous metabolome. Untargeted libraries containing ~2,700 metabolites, drawn from the KEGG database, and the top five candidates with the highest intensity throughout a sample run for each metabolite were automatically curated.

Data were normalized by the sum of all targeted metabolites within each sample in each mode and then log transformed. Sample quality was assessed using two internal standards, D_8-phenylalanine and D_4-taurine to identify any outliers to be excluded from the downstream analysis. Next, the normalized data from the two modes were merged. If a metabolite appeared in both modes, the one with the best intensity was chosen.

Principal component analysis, PLS-DA and heat maps from the merged targeted data were performed/generated using MetaboAnalyst (https://www.metaboanalyst.ca/). Differential expression analysis for each comparison was performed using the metabolomics application in Polly (polly.elucidata.io). Normal *P* values and log_2FC data were uploaded to Shiny GAM (https://artyomovlab.wustl.edu/shiny/gam/) to generate an optimized metabolic network displaying ~60 of the most changed and closely connected metabolites. The upregulated and downregulated metabolites in the treatment groups were then used separately for pathway enrichment analysis in MetaboAnalyst.

$NADP^+$:NADPH quantification

First, 4×10^3 AC16 cells were seeded in poly-L-lysine-coated 96-well plates. The following day, cells (at ~60% confluence) were starved of glucose by aspirating media, washing wells twice with 50 µl room temperature PBS, then gently adding 75 µl glucose-free DMEM supplemented with 10% dialysed FBS. When indicated, 16 mM glucose was added to the media. $NADP^+$ and NADPH levels were measured using the NADP/NADPH-Glo Assay (Promega, G9081) following the manufacturer's protocol.

O-propargyl-puromycin incorporation assay

After the indicated treatment (glucose starvation or anisomycin treatment), 20 µM *O*-propargyl-puromycin was added to cell culture media for the last 30 min. The medium was then aspirated, cells were washed once with pre-warmed PBS, trypsinized, inactivated with PBS + 10% FBS and collected in 5-ml round-bottom polystyrene tubes. The cell pellet was washed once with PBS. Cells were fixed by resuspending in 250 µl 4% paraformaldehyde and incubated at room temperature for 10 min. After washing the pellet once with PBS + 3% BSA, cells were permeabilized with 0.25% Triton in PBS for 15 min at room temperature. Cells were then washed twice with PBS + 3% BSA. Alexa Fluor 647 was clicked onto *O*-propargyl-puromycin using the Click-iT Plus Alexa Fluor 647 picolyl azide toolkit (Invitrogen, C10643) according to the manufacturer's instructions. Cells were stained for 30 min at room temperature in the dark, washed once with PBS + 3% BSA and then processed on a BD LSRFortessa X-20 Cell Analyzer.

di-Gly TMT-based proteomics and ubiquitinomics

First, 1.8×10^6 AC16 cells were seeded into poly-L-lysine-coated 15-cm dishes, three plates per sample in quadruplicate. When cells reached 80% confluence, they were starved of glucose as above. After starvation, cells were washed twice with 10 ml ice-cold PBS and scraped into 1 ml urea lysis buffer (9 M urea, 50 mM HEPES pH 8.5 and 0.5% sodium deoxycholate) with 20 mM 2-chloroacetamide (Sigma, C0267) and 4 μg ml^{-1} Lys-C (Wako, 12505061). The same 1 ml was used to harvest all three plates of a sample. Samples were immediately flash frozen in liquid nitrogen then stored at −80 °C

For protein extraction, samples were gently thawed, then placed in a Bullet Blender at a speed of '6' for 30 s with an interval of 10 s at 40 °C for six cycles. Proteins were digested with Lys-C (200:1 protein:enzyme ratio by weight) in the presence of 10 mM DTT and 5% acetonitrile for 3 h, followed by a four-fold dilution with 50 mM HEPES buffer pH 8.5 and overnight trypsin digestion (50:1 protein:enzyme by weight) (Promega, V5280) at room temperature. The peptides were desalted on C18 SPE column (Waters) and dried under vacuum.

The enrichment of di-Gly peptides was performed using PTMScan HS Ubiquitin/SUMO Remnant Motif (K-GG) Kit (Cell Signaling Technology) as previously described[100]. Briefly, the di-Gly peptides were isolated from 2 mg peptides by magnetic K-GG beads after incubation at 40 °C for 1.5 h. The eluted di-Gly peptides were adjusted to pH 8.5 using 50 mM HEPES and labelled with 60 μg TMTpro reagent at room temperature for 30 min. After the reaction was quenched with 5% hydroxylamine, the TMTpro-labelled di-Gly peptides were mixed in equal amounts, desalted on C18 stagetips and fractionated in a 60 min gradient of 15–50% B on a reverse phase HPLC column (ACQUITY UPLC BEH C18 column, 1.0 × 100 mm, 1.7 μm particle size, Waters) on an Agilent 1220 HPLC system (buffer A: 10 mM ammonium formate pH 8.0; buffer B: 90% MeCN and 10 mM ammonium formate pH 8.0) and collected into ten fractions. All fractions were dried, reconstituted in 5% formic acid and analysed using acidic pH reverse phase LC–MS/MS (CoAnn Technologies, 75 μm ID x 20 cm, 1.9 μm C18 resin at 60 °C) on an Ultimate 3000 UPLC system (Thermo Fisher Scientific). Peptides were eluted in a 120 min gradient of 16–55% buffer B (67% MeCN, 3% DMSO and 0.1% FA) with buffer A (3% DMSO and 0.1% FA) at a flow rate of 0.25 μl min^{-1} before mass spectrometry analysis.

For total proteome analysis, the peptides in the flowthrough from di-Gly enrichment experiments were labelled with TMTpro at a ratio of 1.5:1 by weight. After mixing in equal amounts, the fractionation was performed on an ACQUITY UPLC BEH C18 column (2.1 × 100 mm, 1.7 μm particle size; Waters). The HPLC gradient was 15–50% B for 120 min at a flow rate of 0.2 ml min^{-1} on the same Agilent 1220 HPLC system. A total of 40 pooled fractions were dried under vacuum, resuspended in 5% formic acid and analysed by acidic pH reverse phase LC–MS/MS in an 80 min gradient of 16–55% buffer B before mass spectrometry analysis.

The Orbitrap HF mass spectrometer (Thermo Fisher Scientific) was operated in data-dependent mode. The parameters for MS1 scan were set as 60,000 resolution, scan range 460–1600 m/z, 3×10^6 automatic gain control (AGC) target and 50 ms maximal ion time for whole proteome analysis. The parameters for MS2 scans were 120 m/z low mass threshold, 1×10^5 AGC, 110 ms maximal ion time, 20 data-dependent MS2 scans, a 1.0 m/z isolation window with a 0.2 m/z offset, 32 normalized collision energy in higher-energy collisional dissociation and a 10 s dynamic exclusion for whole proteome analysis. For ubiquitinome analysis, MS1 scans were set as 60,000 resolution, a scan range 530–1,600 m/z, 3×10^6 AGC target and 50 ms maximal ion time. MS2 scans were set as 120 m/z low cut-off, 1×10^5 AGC, 150 ms maximal ion time, 17 data-dependent MS2 scans, a 1.0 m/z isolation window with 0.2 m/z offset, 30–32 normalized collision energy in higher-energy collisional dissociation and a 20 s dynamic exclusion.

The mass spectrometric database search was processed by the JUMP software suite[101]. The MS/MS spectra were searched against the UniProt human protein database, which contained 170,122 entries and was downloaded in 2020. The search parameters included a mass tolerance of 15 ppm for both precursor ions and MS/MS ions, full trypticity with a maximum two missed cleavages, a maximum of three dynamic modification sites per peptide, dynamic modification with Met oxidation (+15.99492 Da) and Lys di-Gly modification (+114.04293 Da, for ubiquitinomes), and static modifications with TMT tags on Lys and N-termini (+304.2071453 Da) and Cys carbamidomethylation (+57.02146 Da). All protein and peptide identifications were filtered on the basis of mass accuracy and matching scores using the target–decoy strategy to reduce protein or peptide FDR to <1%. The quantification of proteins and di-Gly peptides was performed using the JUMP suite pipeline. Differentially expressed di-Gly peptides were determined using both P values and $\log_2$FCs calculated by the limma R package. The significance of differential expression was evaluated on the basis of statistical criteria, with $P < 0.01$ and $\log_2$FC > two-fold of the standard deviation (s.d.). The s.d. of di-Gly peptides was estimated by fitting to a Gaussian distribution to evaluate the magnitude of experimental variations.

Polysome and disome profiling

First, 1.8×10^6 AC16 cells were seeded in poly-L-lysine-coated 15-cm dishes, with four plates per sample. Cells were starved of glucose for the indicated times or treated with 5 μM anisomycin for 1 h in full medium. After treatment, cells were washed three times with 10 ml ice-cold PBS + 100 μg ml^{-1} cycloheximide (CHX) on ice. Cells were scraped into 1 ml polysome lysis buffer (15 mM Tris–HCl pH 7.5, 5 mM $MgCl_2$, 150 mM NaCl and 1% Triton X-100) supplemented with fresh 2 mM DTT, 100 μg ml^{-1} CHX and a protease inhibitor. The same 1 ml was used to harvest all plates of a sample. Lysates were left on ice for 5 min, then clarified at 21,000g for 5 min at 4 °C. All samples were diluted to 1.7 mg ml^{-1} in a 1 ml final volume and flash frozen in liquid nitrogen.

For disome analysis, cells were treated and lysed as above. Following lysate clarification, RNA content was measured using the Qubit RNA BR Assay Kit (Thermo Fisher, Q10210). Then, 100 μg RNA per sample was digested with 2 μg RNase A (Thermo Scientific, EN0531) at 24 °C with 200 rpm agitation for 20 min. RNase was quenched by adding 200U SUPERase·In RNase inhibitor (Invitrogen, AM2694) and subjected to fractionation immediately.

Sucrose gradients of 10–50% (for polysomes) or 10–40% (for disomes) (15 mM Tris pH 7.5, 5 mM $MgCl_2$, 150 mM NaCl, 2 mM DTT and 100 μg ml^{-1} CHX) were made and fractionated using Biocomp Gradient Station (Biocomp Instruments). Lysates were thawed on ice, added to sucrose gradients and centrifuged at 160,000g at 4 °C in a Beckmann SW41 rotor for 2 h. During fractionation, absorbance was continually monitored at 260 nm. Fractions were collected and subjected to immunoblot analysis where indicated.

Proximity labelling

First, 1.8×10^6 MiniTurbo fusion-expressing AC16 cells were seeded in poly-L-lysine-coated 15-cm dishes, two plates per sample. When cells reached ~70% confluence, media was aspirated, cells were washed twice with 10 ml PBS and replaced with 20 ml glucose-free DMEM + 10% dialysed FBS + 50 μM D-biotin (Sigma-Aldrich, B4639). Further, 16 mM D-glucose was added to control plates. After starvation, cells were washed twice with 10 ml ice-cold PBS, then scraped into 1 ml RIPA lysis buffer (150 mM NaCl, 5 mM EDTA pH 8.0, 50 mM Tris–HCl pH 8.0, 1% NP-40, 0.5% sodium deoxycholate and 0.1% SDS) containing protease and phosphatase (Sigma-Aldrich, 4906845001) inhibitors. The same 1 ml was used to harvest all plates of a sample. Lysates were placed on ice for 30 min with intermittent vortexing, then clarified at 14,000g for 20 min at 4 °C. Clarified lysates were pre-cleared with 15 μl washed Protein A magnetic beads (Cell Signaling Technology, 73778) for 30 min at 4 °C with rotation. Then, 50 μl of washed Streptavidin Magnetic Beads (Pierce, 88816) were added to 1.5 mg lysate in a 1 ml final volume and rotated overnight at 4 °C. The next day, beads were

washed four times in 1 ml ice-cold RIPA, followed by four times in 1 ml ice-cold PBS. The beads were transferred to a fresh tube on the last wash. PBS was completely removed and the beads were subjected to LC–MS/MS analysis.

Statistics and reproducibility

Unless otherwise specified, statistical analyses were performed using GraphPad Prism software (v.10). No statistical method was used to predetermine sample sizes, but our sample sizes are similar to those reported in previous publications[31,50,60]. No data were excluded from the analyses. Experimenters were blinded to mouse genotypes during surgery, echocardiography and histological analyses. Experimenters were not blinded during cell culture experiments. Details on biological replicates and statistical tests are included in the figure legends. Data distribution was assumed to be normal but this was not formally tested. Metabolome and ubiquitinome analysis experiments were performed once, and proximity labelling experiments were performed two independent times. All other experiments were repeated at least three times with similar results unless otherwise indicated.

Reporting summary

Further information on research design is available in the Nature Portfolio Reporting Summary linked to this article.

Data availability

Mass spectrometry data from LC–MS/MS ubiquitin remnant profiling have been deposited in ProteomeXchange with the primary accession code PXD046661 (https://www.ebi.ac.uk/pride/archive/projects/PXD046661). Metabolomics data are available in Supplementary Table 1. No restrictions on data availability apply. All other data supporting the findings of this study are available from the corresponding author on reasonable request. Source data are provided with this paper.

Code availability

No original code was generated in this study.

References

96. Li, N. et al. miR-182 modulates myocardial hypertrophic response induced by angiogenesis in heart. *Sci. Rep.* **6**, 21228 (2016).
97. da Silva, F. S., Aquino de Souza, N. C. S., de Moraes, M. V., Abreu, B. J. & de Oliveira, M. F. CmyoSize: an ImageJ macro for automated analysis of cardiomyocyte size in images of routine histology staining. *Ann. Anat.* **241**, 151892 (2022).
98. Labun, K., Krause, M., Torres Cleuren, Y. & Valen, E. CRISPR genome editing made easy through the CHOPCHOP website. *Curr. Protoc.* **1**, e46 (2021).
99. Namkoong, S., Ho, A., Woo, Y. M., Kwak, H. & Lee, J. H. Systematic characterization of stress-induced RNA granulation. *Mol. Cell* **70**, 175–187 (2018).
100. Radko-Juettner, S. et al. Targeting DCAF5 suppresses SMARCB1-mutant cancer by stabilizing SWI/SNF. *Nature* **628**, 442–449 (2024).
101. Wang, X. et al. JUMP: a tag-based database search tool for peptide identification with high sensitivity and accuracy. *Mol. Cell. Proteomics.* **13**, 3663–3673 (2014).

Acknowledgements

This work was supported in part by the NIH grant no. R35CA197589 to C.M.C., NIH grant nos. R01HL148008 and R01HL128069 to L.H.Y., NIH grant no. R01GM132358 and NSF grant no. 2330451 to W.V.G. and NSF GRFP DGE2139841 to K.S.A. We thank R. Cardone, Q. Sun and the Chemical Metabolism Core at Yale University for their assistance with LC–MS/MS global metabolomics; N. Guerrera for echocardiography; J. Kanyo, F. Collin and the Keck Proteomics Core at Yale University for LC–MS/MS analysis of proximity labelling experiments; and J. Hines for careful reading of the manuscript. HOIL-1$^{\Delta RBR}$ mice were kindly provided by D. MacDuff (University of Illinois at Chicago). The TssM* construct was a kind gift from J. Pruneda (Oregon Health and Science University).

Author contributions

Conceptualization: T.D. Methodology: T.D., J.Z., K.S.A. and Z.W. Investigation: T.D., P.N., J.Z., Z.W., K.S.A. and M.M. Resources: K.I. Writing—original draft: T.D. Writing—review and editing: T.D., L.H.Y. and C.M.C. Visualization: T.D. Supervision: T.D., W.V.G., J.P., L.H.Y. and C.M.C. Project administration: T.D. Funding acquisition: C.M.C., L.H.Y. and W.V.G.

Competing interests

The authors declare no competing interests.

Additional information

Extended data is available for this paper at https://doi.org/10.1038/s41556-026-01936-6.

Supplementary information The online version contains supplementary material available at https://doi.org/10.1038/s41556-026-01936-6.

Correspondence and requests for materials should be addressed to Todd Douglas.

Peer review information *Nature Cell Biology* thanks Boyi Gan, Toshifumi Inada and the other, anonymous, reviewer(s) for their contribution to the peer review of this work. Peer reviewer reports are available.

https://doi.org/10.1038/s41556-026-01936-6

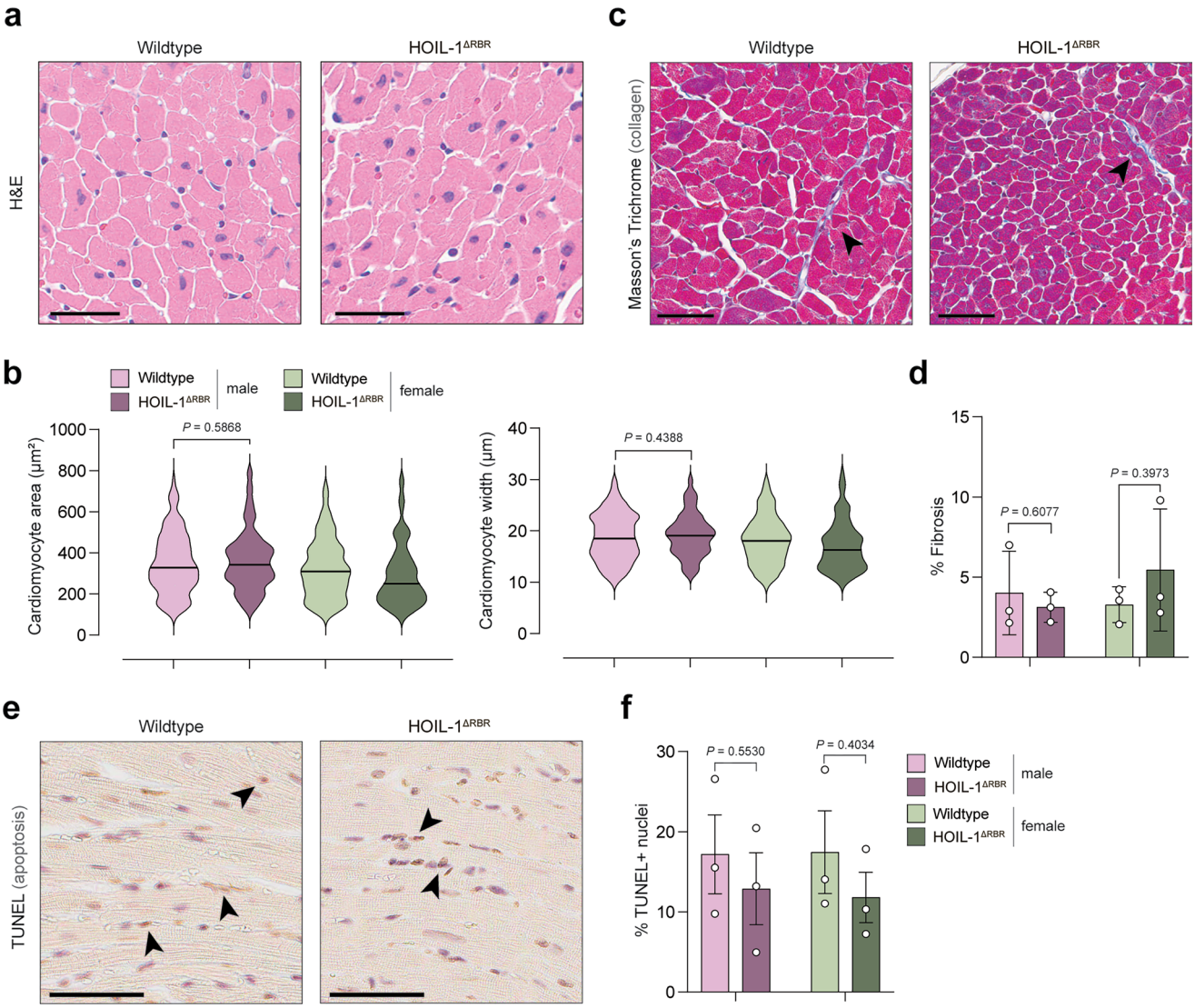

Extended Data Fig. 1 | HOIL-1 loss does not influence cardiac fibrosis or cardiomyocyte apoptosis under pressure overload. a, Hematoxylin and eosin (H&E)-stained sections from untreated male mice. Scale bar = 30 µm. **b**, Violin plot of cardiomyocyte cross-sectional area and width quantified from H&E images (n = 3 WT male mice, n = 3 HOIL-1$^{\Delta RBR}$ male mice, n = 4 WT female mice, n = 2 HOIL-1$^{\Delta RBR}$ female mice). Black line is the median. **c**, Masson's Trichrome-stained male heart sections 9 weeks post-TAC. Arrowheads indicate interstitial collagen. Scale bar = 45 µm. **d**, Cardiac fibrosis quantified from Masson's Trichrome images (n = 3 male mice, n = 3 female mice per genotype). **e**, TUNEL-stained heart sections 9 weeks post-TAC. Arrowheads indicate TUNEL+ nuclei. Scale bar = 60 µm. **f**, Proportion of TUNEL+ nuclei quantified from TUNEL images (n = 3 male mice, n = 3 female mice per genotype). Data are presented as the mean ± s.e.m (**d**, **f**). *P* values were determined by unpaired two-tailed Student's t-test (**b**, **d**, **f**). Source numerical data are available in Source Data.

https://doi.org/10.1038/s41556-026-01936-6

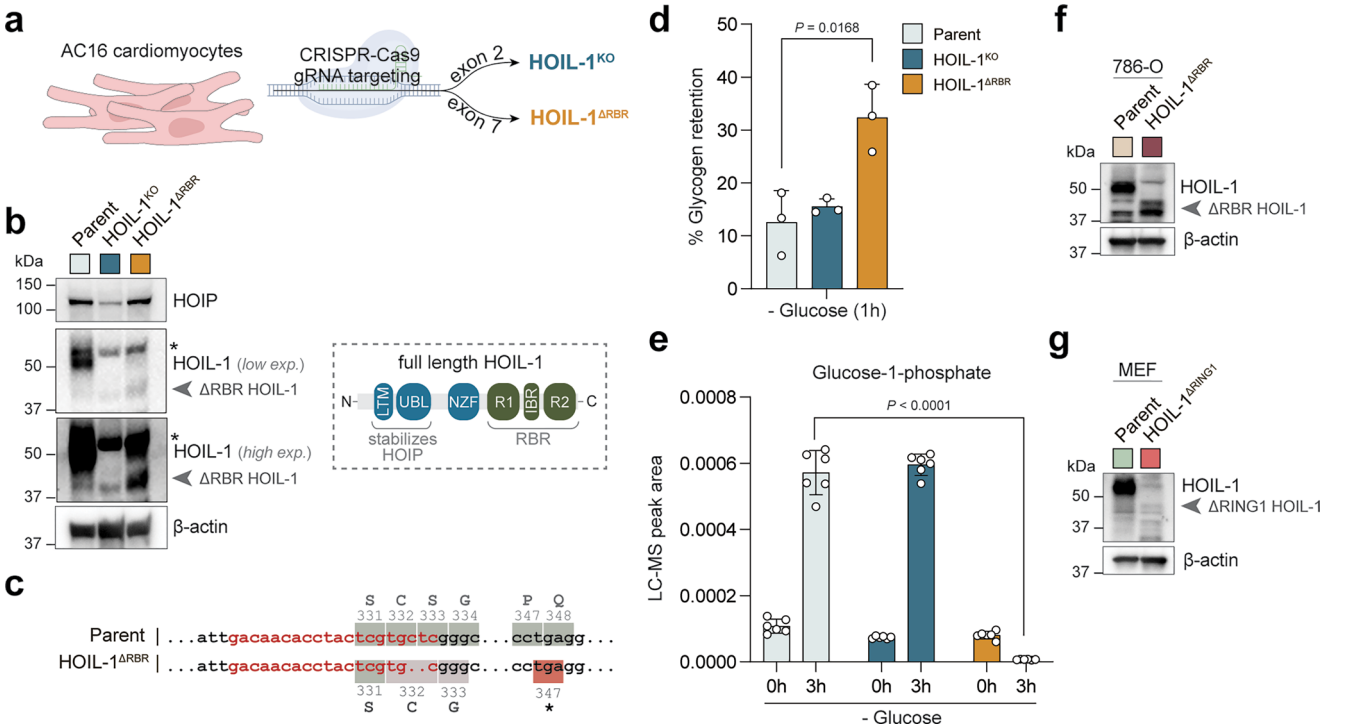

Extended Data Fig. 2 | Loss of the HOIL-1 RBR impairs glycogen breakdown. **a**, Model system. **b**, Immunoblot analysis of AC16 cells. Arrowhead indicates ΔRBR HOIL-1. Asterisks indicate non-specific bands. **c**, Genomic DNA sequencing from AC16 cells confirming deletion and premature stop codon in HOIL-1$^{\Delta RBR}$ cells. Red text is the gRNA target sequence. **d**, Fraction of cellular glycogen remaining after 1 h glucose starvation in AC16 cells. Pooled data from three independent experiments. Each data point is the mean of 3 biological replicates. Data are presented as mean ± s.d. **e**, Glucose-1-phosphate levels in AC16 cells after glucose starvation measured by LC-MS (n = 6 biological replicates). Data are presented as mean ± s.e.m. **f**, Immunoblot analysis of HOIL-1$^{\Delta RBR}$ 786-O cells. **g**, Immunoblot analysis of HOIL-1$^{\Delta RING1}$ MEFs. *P* values were determined by unpaired two-tailed Student's *t*-test (**d**) or two-way ANOVA followed by Dunnett's post-hoc comparison (**e**). Source numerical data and uncropped blots are available in Source Data.

https://doi.org/10.1038/s41556-026-01936-6

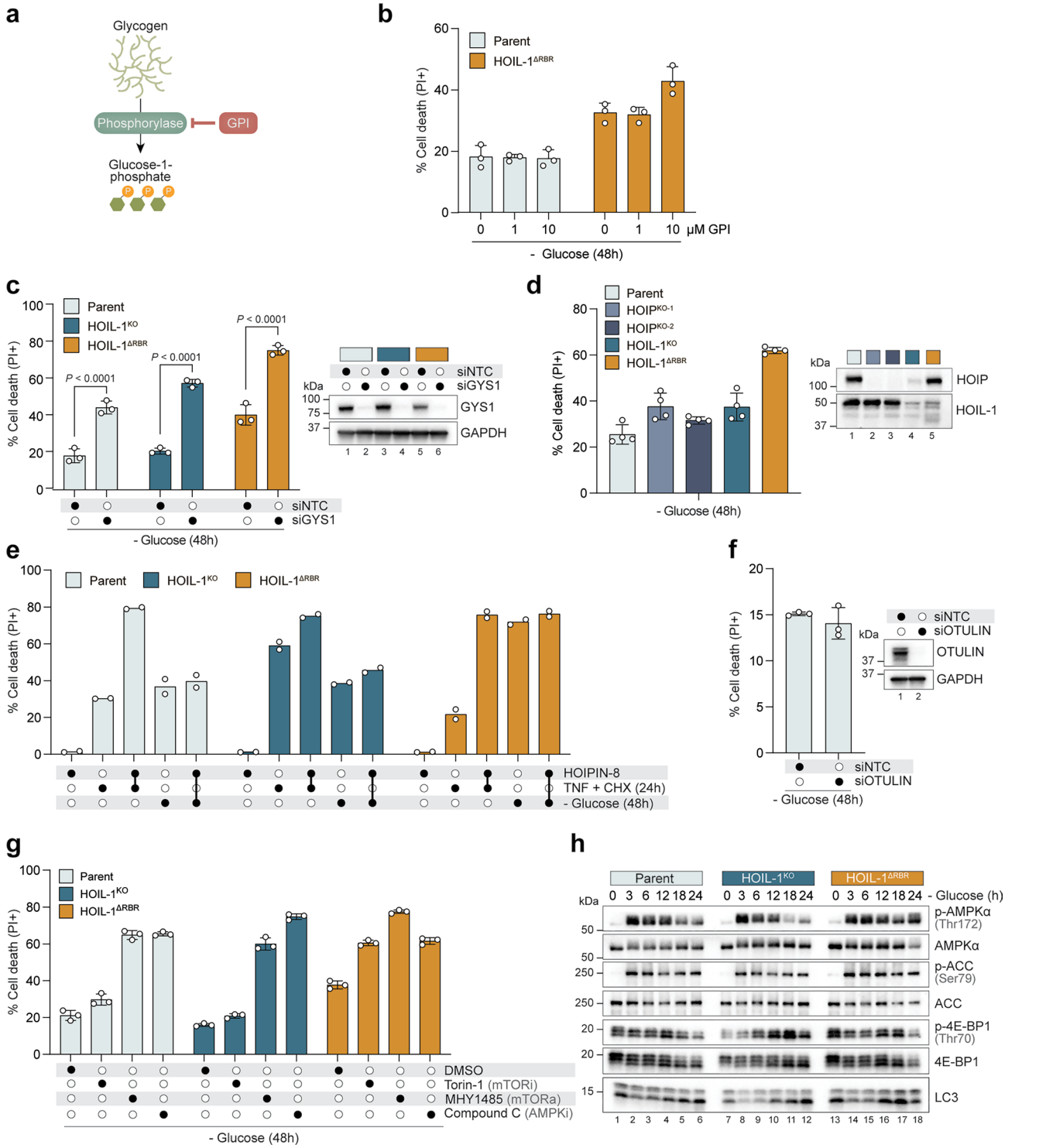

Extended Data Fig. 3 | Glucose starvation causes noncanonical cell death. **a**, Schematic. Glycogen phosphorylase inhibitor (GPI) reduces glycogen breakdown. **b**, Cell death in AC16 cells pre-treated with GPI for 1 h followed by 48 h glucose starvation (n = 3 biological replicates). **c**, Cell death in AC16 cells transfected with GYS1 or non-targeting control (NTC) siRNA prior to glucose starvation for 48 h (n = 3 biological replicates). **d**, Cell death in HOIP^{KO} AC16 cells after 48 h glucose starvation (n = 4 biological replicates). **e**, Cell death in AC16 cells after TNF (20 ng/ml) + CHX (6 μg/ml) treatment for 24 h or glucose starvation for 48 h in combination with HOIPIN-8 (30 μM) (n = 2 biological replicates). **f**, Cell death in AC16 cells transfected with OTULIN or NTC siRNA prior to glucose starvation for 48 h (n = 3 biological replicates). **g**, Cell death in AC16 cells treated with DMSO vehicle, Torin-1 (250 nM), MHY1485 (20 μM), or Compound C (7 μM) concurrent with 48 h glucose starvation (n = 3 biological replicates). **h**, Immunoblot analysis for AMPK and mTOR-related proteins in AC16 cells following glucose starvation for the indicated time-points. Data are presented as mean ± s.e.m from one representative experiment (**b**-**g**). *P* values were determined by two-way ANOVA followed by Dunnett's post-hoc comparison (**c**). Source numerical data and uncropped blots are available in Source Data.

https://doi.org/10.1038/s41556-026-01936-6

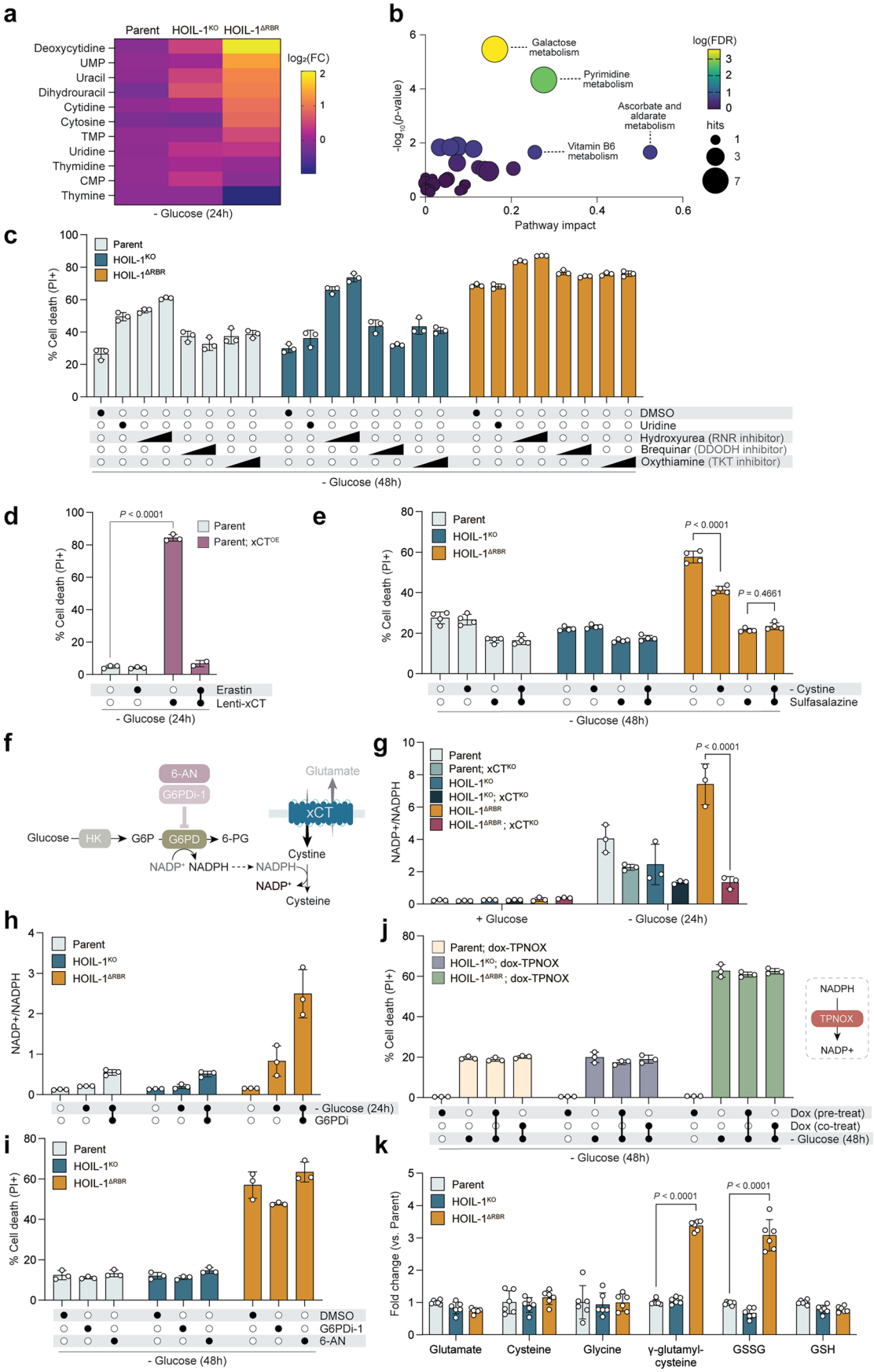

Extended Data Fig. 4 | See next page for caption.

https://doi.org/10.1038/s41556-026-01936-6

Extended Data Fig. 4 | NADPH collapse does not cause glucose starvation-induced cell death. a, Heatmap of metabolite levels after 24 h glucose starvation represented as log2(FC) of parental AC16 cells. **b**, Pathway analysis of metabolites enriched in HOIL-1$^{\Delta RBR}$ cells after 24 h glucose starvation. **c**, Cell death in AC16 cells after DMSO vehicle, uridine (25 mM), hydroxyurea (0.2 mM, 2.0 mM), brequinar (0.1 μM, 1.0 μM), or oxythiamine (0.5 mM, 5 mM) treatment concurrent with 48 h glucose starvation (n = 3 biological replicates). **d**, Cell death in AC16 cells stably overexpressing (OE) xCT treated with erastin (2 μM) concurrent with 48 h glucose starvation (n = 3 biological replicates for all except parent-xCT^{OE} + erastin, n = 2 biological replicates). **e**, Cell death in AC16 grown in L-cystine and glucose-free media supplemented with L-cystine (200 μM) or sulfasalazine (500 μM) for 48 h (n = 4 biological replicates). **f**, Schematic of NADP + and/NADPH flux. **g**, Measurement of NADP+ and NADPH ratio during glucose starvation in xCT^{KO} AC16 cells (n = 3 biological replicates). **h**, Measurement of NADP+ and NADPH ratio in AC16 cells treated with G6PD inhibitor (G6PDi-1, 50 μM) during glucose starvation (n = 3 biological replicates). **i**, Cell death in AC16 cells after DMSO vehicle, G6PDi-1 (50 μM), or 6-aminonicotinamide (6-AN, 20 μM) treatment concurrent with 48 h glucose starvation (n = 3 biological replicates). **j**, Cell death in AC16 cells stably overexpressing doxycycline (dox)-inducible TPNOX treated with dox (1 μg/ml) for either 24 h prior to (pre-treat) or concurrently (co-treat) with 48 h glucose starvation (n = 3 biological replicates). **k**, xCT-related metabolite levels at 24 h glucose starvation as measured by untargeted LC-MS represented as fold change over parent (n = 6 biological replicates). Data are presented as mean ± s.e.m from one representative experiment (**c**-**e**, **g**-**k**). *P* values were determined by two-way ANOVA followed by Tukey's (**e**) or Dunnett's (**g**, **k**) post-hoc comparison. Source numerical data are available in Source Data.

https://doi.org/10.1038/s41556-026-01936-6

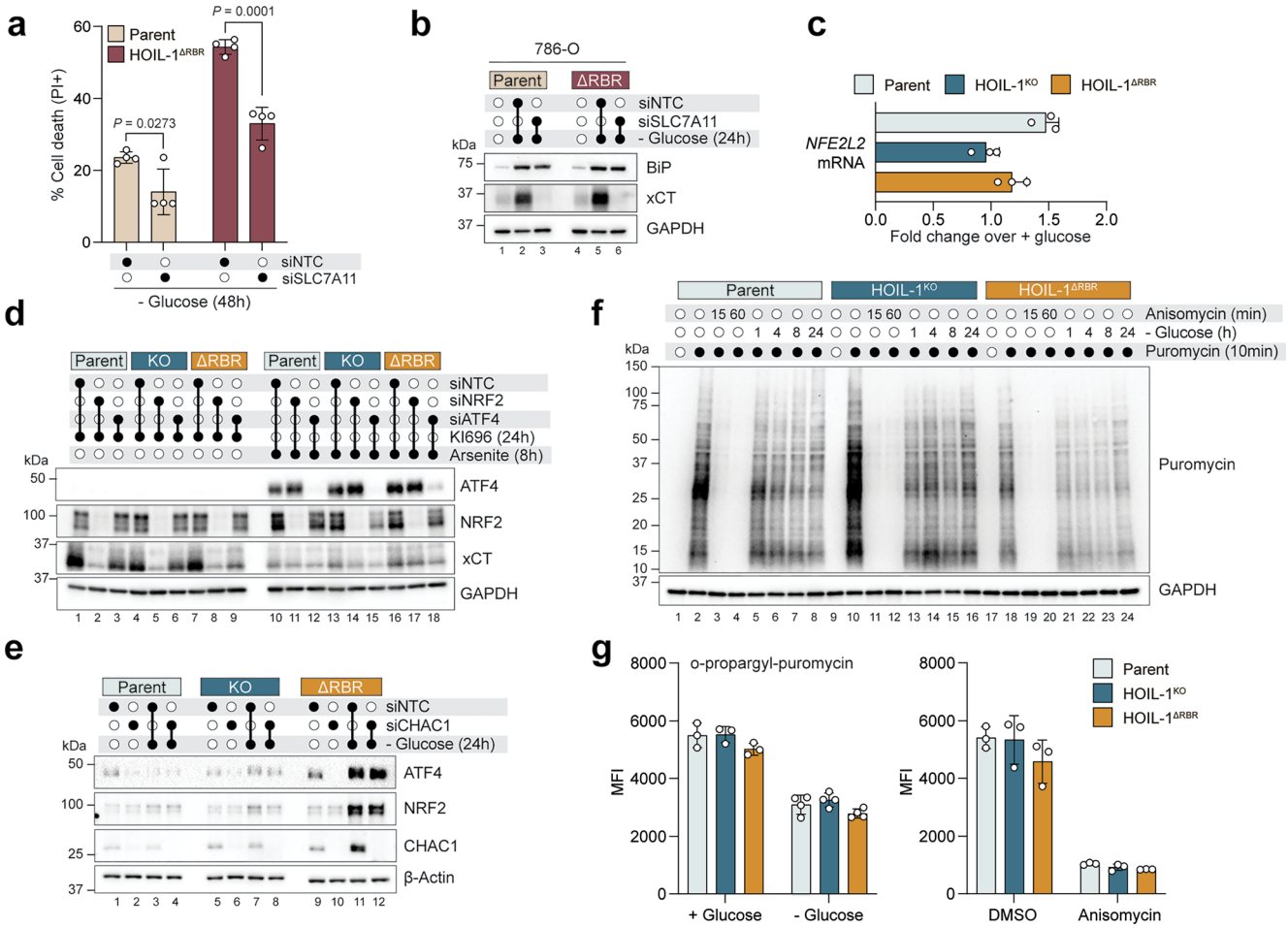

Extended Data Fig. 5 | ATF4 post-transcriptionally regulates NRF2. **a**, Cell death in 786-O cells transfected with xCT or NTC siRNA prior to glucose starvation for 48 h (n = 4 biological replicates). **b**, Immunoblot analysis of 786-O cells transfected with xCT or NTC siRNA prior to glucose starvation. **c**, NRF2 (*NFEL2*) mRNA levels (normalized to *TBP*) in AC16 cells after 24 h glucose starvation. Data represented as the fold change over full media (n = 3 biological replicates). **d**, Immunoblot analysis of AC16 cells transfected with ATF4, NRF2, or non-targeting control (NTC) siRNA 48 h prior to treatment with KI696 (NRF2 activator, 1 μM) for 24 h or sodium arsenite (10 μM) for 8 h. **e**, Immunoblot analysis of AC16 cells transfected with CHAC1 or NTC siRNA prior to glucose starvation for 24 h. **f**, Immunoblot analysis of puromycin incorporation in AC16 cells treated with anisomycin (5 μM) or starved of glucose for the indicated times. **g**, Alexa Fluor 647-o-propargyl-puromycin incorporation in AC16 cells starved of glucose (24 h) or treated with anisomycin (15 min) measured by flow cytometry (n = 3 biological replicates for all except -glucose, n = 4 biological replicates). Data are presented as mean ± s.e.m from one representative experiment (**a**, **c**, **g**). *P* values were determined by unpaired two-tailed Student's *t*-test (**a**). Source numerical data and uncropped blots are available in Source Data.

https://doi.org/10.1038/s41556-026-01936-6

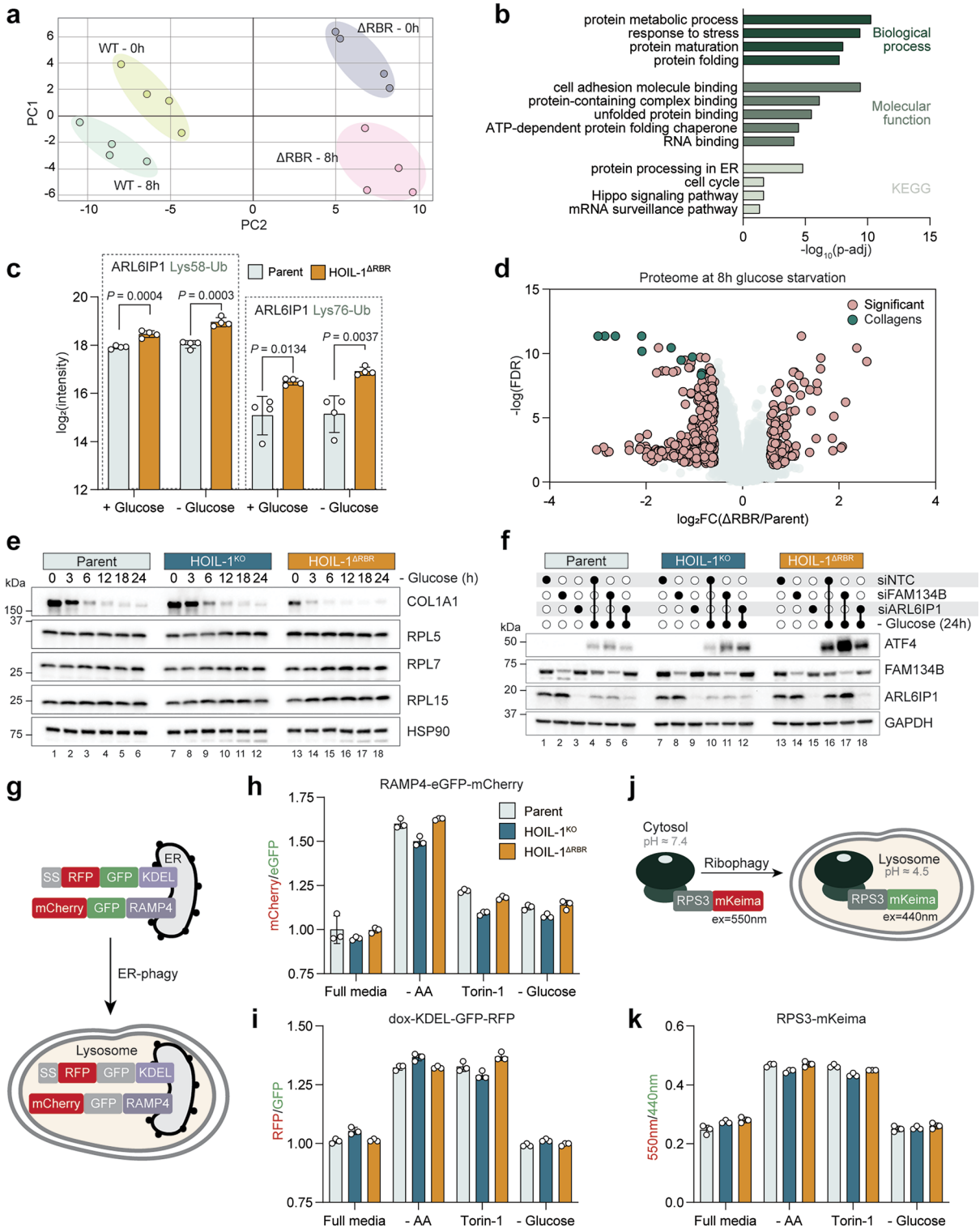

Extended Data Fig. 6 | Selective autophagy is not involved in the glucose starvation response. a, Principal component analysis of ubiquitinome data. **b**, Gene ontology enrichment analysis of proteins with increased ubiquitin-modified peptides in HOIL-1$^{\Delta RBR}$ cells relative to parent AC16 cells after 8 h glucose starvation. **c**, Log transformed intensities of ARL6IP1 ubiquitinated lysines in AC16 cells detected by LC-MS/MS (n = 6 biological replicates). **d**, Volcano plot of differentially abundant proteins in parent and HOIL-1$^{\Delta RBR}$ AC16 cells after 8 h glucose starvation. Significant: FDR > 0.05, log2FC > 2 SD. **e**, Immunoblot analysis of AC16 cells starved of glucose for the indicated time-points. **f**, Immunoblot analysis of AC16 cells transfected with FAM134B, ARL6IP1, or non-targeting control (NTC) siRNA 48 h prior to glucose starvation for 48 h. **g**, Schematic of ER-phagy reporters. GFP quenching in the acidic lysosome alters the GFP:RFP ratio. **h**, Flow cytometric analysis of mCherry and GFP intensity in AC16 cells stably expressing RAMP4-eGFP-mCherry treated with Torin-1 (250 nM) or starved of amino acids (AA) or glucose for 24 h (n = 3 biological replicates). **i**, As in (**g**) but cells stably expressing dox-KDEL-GFP-RFP were treated with doxycycline (1 µg/ml) for 24 hours prior to starvation or treatment (n = 3 biological replicates). **j**, Schematic of ribophagy reporters. **k**, As in (**h**,**i**) but cells express RPS3-mKeima (n = 3 biological replicates). Data are presented as mean ± s.e.m from one representative experiment (**c**, **h**-**k**). *P* values were determined by unpaired two-tailed Student's *t*-test (**c**). Source numerical data and uncropped blots are available in Source Data.

https://doi.org/10.1038/s41556-026-01936-6

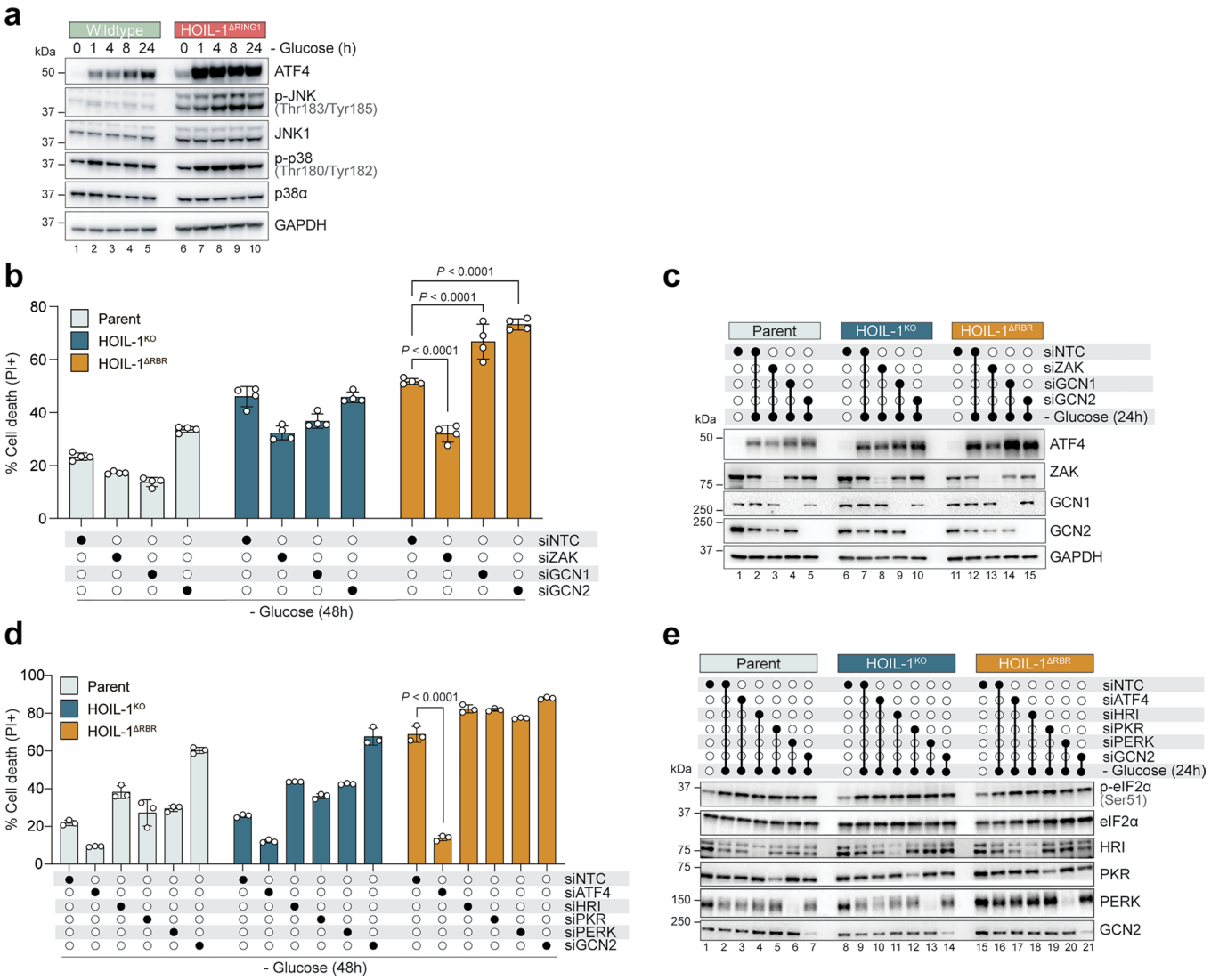

Extended Data Fig. 7 | GCN1, GCN2, and the eIF2α kinases do not promote disulfidptosis. a, Immunoblot analysis of MEFs starved of glucose for the indicated time-points. **b**, Cell death in AC16 cells transfected with ZAK, GCN1, GCN2 or non-targeting control (NTC) siRNA prior to glucose starvation for 48 h (n = 4 biological replicates). **c**, Immunoblot analysis of AC16 cells transfected with ZAK, GCN1, GCN2 or NTC siRNA prior to glucose starvation for 24 h. **d**, Cell death in AC16 cells transfected with the indicated siRNA prior to glucose starvation for 48 h (n = 3 biological replicates). **e**, Immunoblot analysis of AC16 cells transfected with the indicated siRNA prior to glucose starvation for 24 h. Data are presented as mean ± s.e.m from one representative experiment (**b**,**d**). *P* values were determined by two-way ANOVA followed by Dunnett's post-hoc comparison (**b**,**d**). Source numerical data and uncropped blots are available in Source Data.

https://doi.org/10.1038/s41556-026-01936-6

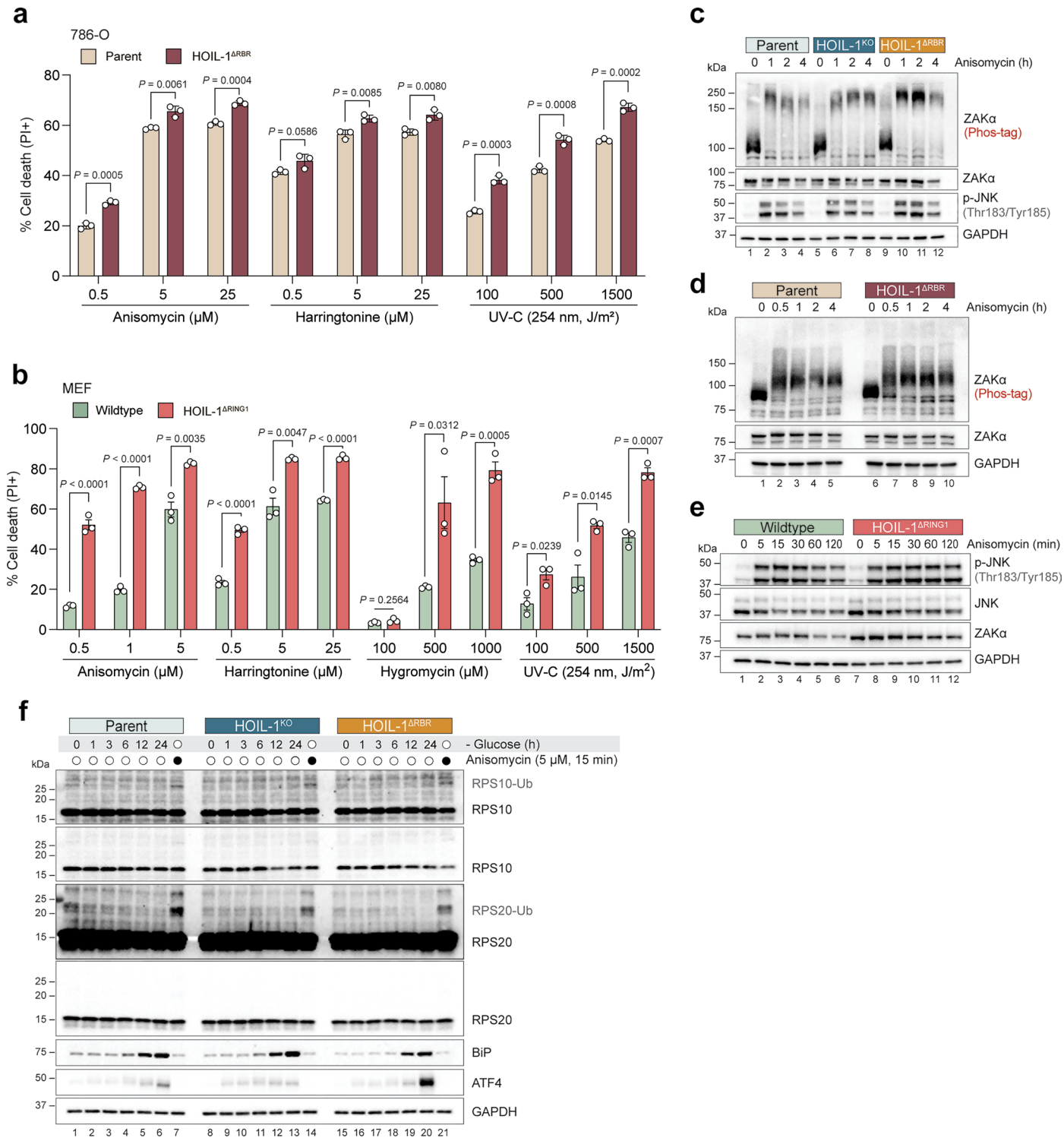

Extended Data Fig. 8 | HOIL-1 loss-of-function enhances cell death and prolongs ribotoxic stress during translational stress. a, Cell death in 786-O cells treated with the indicated ribotoxic stressors for 24 h (n = 3 biological replicates). Hygromycin was not used as HOIL-1$^{\Delta RBR}$ 786-O cells were generated with a hygromycin resistant plasmid. **b**, Cell death in MEFs treated with the indicated ribotoxic stressors for 24 h (n = 3 biological replicates). **c**, Immunoblot analysis of AC16 cells after anisomycin (5 μM) treatment for the indicated time-points. ZAKα phosphorylation was assessed using a Phos-Tag acrylamide gel. **d**, Immunoblot analysis of 786-O cells after anisomycin (0.5 μM) treatment for the indicated time-points. ZAKα phosphorylation was assessed using a Phos-Tag acrylamide gel. **e**, Immunoblot analysis of MEFs after anisomycin (0.5 μM) treatment. **f**, Immunoblot analysis of AC16 cells after glucose starvation or anisomycin (5 μM) treatment for the indicated time-points. Data are presented as mean ± s.e.m from one representative experiment. P values were determined by two-way ANOVA followed by Dunnett's post-hoc comparison. Source numerical data and uncropped blots are available in Source Data.

https://doi.org/10.1038/s41556-026-01936-6

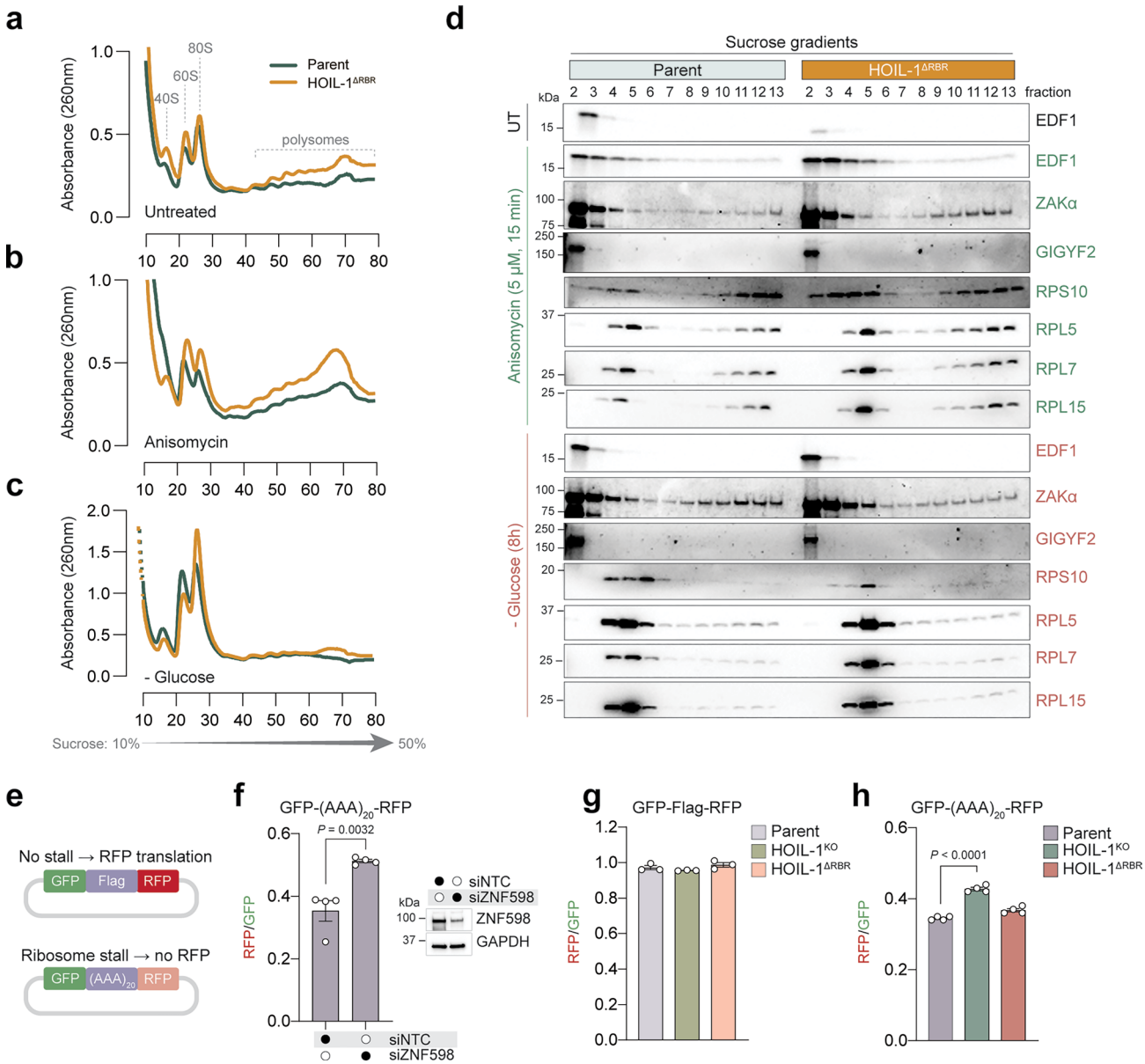

Extended Data Fig. 9 | Glucose starvation does not cause ribosome collisions. **a**, Polysome profiles from lysates of untreated AC16 cells. **b**, Polysome profiles from lysates of AC16 cells treated with anisomycin (5 μM) for 1 hour. **c**, Polysome profiles from lysates of AC16 cells starved of glucose for 24 h. **d**, Immunoblot analysis of sucrose fractions from **a**-**c**. **e**, Schematic of ribosome stalling reporter constructs. Ribosome stalling on $(AAA)_{20}$ reduces RFP translation. **f**, Flow cytometric analysis of GFP and RFP in AC16 cells stably expressing the ribosome stalling reporter transfected with ZNF598 or NTC siRNA 48 h prior (n = 4 biological replicates). Immunoblot analysis of ZNF598 knockdown shown. **g**, Flow cytometric analysis of GFP and RFP in AC16 cells stably expressing the ribosome nonstalling reporter (n = 3 biological replicates). **h**, Flow cytometric analysis of GFP and RFP in AC16 cells stably expressing the ribosome stalling reporter (n = 3 biological replicates). Data are presented as mean ± s.e.m from one representative experiment. *P* values were determined by unpaired two-tailed Student's *t*-tests (**f**, **h**). Source numerical data and uncropped blots are available in Source Data.

https://doi.org/10.1038/s41556-026-01936-6

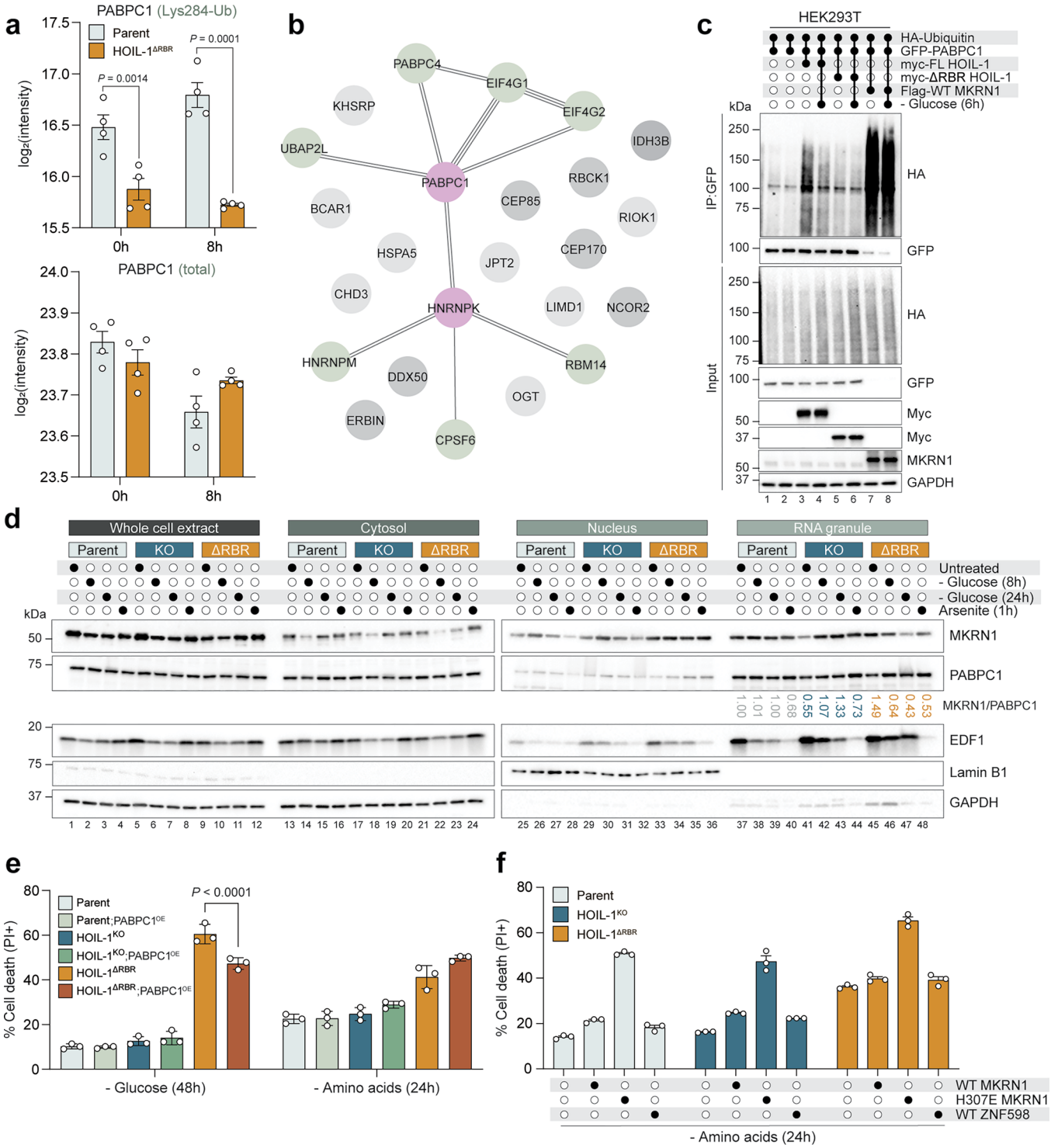

Extended Data Fig. 10 | HOIL-1 ubiquitinates PABPC1 and controls MKRN1 localization. a, Log transformed intensities of PABPC1 ubiquitinated Lys284 and total levels in AC16 cells detected by LC-MS/MS (n = 4 biological replicates). **b**, STRING analysis of the ΔRBR HOIL-1 proximitome during glucose starvation. **c**, Immunoblot analysis of HEK293T cells transfected with the indicated plasmids 24 h prior to 6 h glucose starvation where indicated, followed by hot lysis in 1% SDS and anti-GFP immunoprecipitation. **d**, Immunoblot analysis of AC16 cells treated with sodium arsenite (10 μM) or starved of glucose for the indicated time-points, followed by subcellular fractionation of RNA-protein granules. **e**, Cell death in AC16 cells stably expressing PABPC1-GFP after 48 h glucose starvation or 24 h amino acid starvation (n = 3 biological replicates). **f**, Cell death in AC16 cells stably expressing MKRN1 or ZNF598 after 24 h amino acid starvation (n = 3 biological replicates). Data are presented as mean ± s.e.m from one representative experiment. *P* values were determined by unpaired two-tailed Student's t-tests (**a**) and two-way ANOVA followed by Holm–Šídák's post-hoc comparison (**e**). Source numerical data and uncropped blots are available in Source Data.

nature portfolio

Corresponding author(s): Todd Douglas

Last updated by author(s): 2026 03 12

Reporting Summary

Nature Portfolio wishes to improve the reproducibility of the work that we publish. This form provides structure for consistency and transparency in reporting. For further information on Nature Portfolio policies, see our Editorial Policies and the Editorial Policy Checklist.

Statistics

For all statistical analyses, confirm that the following items are present in the figure legend, table legend, main text, or Methods section.

n/a	Confirmed	
☐	☒	The exact sample size (*n*) for each experimental group/condition, given as a discrete number and unit of measurement
☐	☒	A statement on whether measurements were taken from distinct samples or whether the same sample was measured repeatedly
☐	☒	The statistical test(s) used AND whether they are one- or two-sided *Only common tests should be described solely by name; describe more complex techniques in the Methods section.*
☒	☐	A description of all covariates tested
☐	☒	A description of any assumptions or corrections, such as tests of normality and adjustment for multiple comparisons
☐	☒	A full description of the statistical parameters including central tendency (e.g. means) or other basic estimates (e.g. regression coefficient) AND variation (e.g. standard deviation) or associated estimates of uncertainty (e.g. confidence intervals)
☐	☒	For null hypothesis testing, the test statistic (e.g. *F*, *t*, *r*) with confidence intervals, effect sizes, degrees of freedom and *P* value noted *Give P values as exact values whenever suitable.*
☒	☐	For Bayesian analysis, information on the choice of priors and Markov chain Monte Carlo settings
☒	☐	For hierarchical and complex designs, identification of the appropriate level for tests and full reporting of outcomes
☒	☐	Estimates of effect sizes (e.g. Cohen's *d*, Pearson's *r*), indicating how they were calculated

Our web collection on statistics for biologists contains articles on many of the points above.

Software and code

Policy information about availability of computer code

Data collection	Western blot: Image Lab 6.1 (Bio-Rad) Flow cytometry: FACSDiva 6.1 (BD Biosciences) Polysome profiling: Triax Flow Cell v1.56A (Biocomp) Plate reader: SparkControl (Tecan)
Data analysis	Prism v10 (GraphPad) FlowJo v10 (FlowJo, LLC) Fiji (ImageJ) CellProfiler v4.2 (Broad Institute) Scaffold v5.3.3 (Proteome Software) El-MAVEN software (Elucidata.io) JUMPsuite (ttps://github.com/JUMPSuite/JUMP) JUMPshiny (https://jumpshiny.genenetwork.org/) MetaboAnalyst (https://www.metaboanalyst.ca/)

For manuscripts utilizing custom algorithms or software that are central to the research but not yet described in published literature, software must be made available to editors and reviewers. We strongly encourage code deposition in a community repository (e.g. GitHub). See the Nature Portfolio guidelines for submitting code & software for further information.

Data

Policy information about availability of data

All manuscripts must include a data availability statement. This statement should provide the following information, where applicable:

- Accession codes, unique identifiers, or web links for publicly available datasets
- A description of any restrictions on data availability
- For clinical datasets or third party data, please ensure that the statement adheres to our policy

Raw numerical data and uncropped western blot images are provided in Source Data. Raw mass spectrometry data from the ubiquitinomics/proteomics experiment has been deposited at the ProteomeXchange Consortium with the dataset identifier PXD046661 (https://www.ebi.ac.uk/pride/archive/projects/PXD046661). The MS/MS spectra were searched against the UniProt human protein database (https://www.uniprot.org/). Raw metabolomics data is available in Supplementary Table 1. Metabolome pathway analyses were performed using the Human Metabolome Database (https://hmdb.ca/). Gene ontology was performed using ShinyGO 0.82 (https://bioinformatics.sdstate.edu/go/). Protein-protein interaction network analysis was performed using STRING (https://string-db.org/). All other data supporting the findings of the study are available from the corresponding author on reasonable request.

Research involving human participants, their data, or biological material

Policy information about studies with human participants or human data. See also policy information about sex, gender (identity/presentation), and sexual orientation and race, ethnicity and racism.

Reporting on sex and gender	N/A
Reporting on race, ethnicity, or other socially relevant groupings	N/A
Population characteristics	N/A
Recruitment	N/A
Ethics oversight	N/A

Note that full information on the approval of the study protocol must also be provided in the manuscript.

Field-specific reporting

Please select the one below that is the best fit for your research. If you are not sure, read the appropriate sections before making your selection.

☒ Life sciences ☐ Behavioural & social sciences ☐ Ecological, evolutionary & environmental sciences

For a reference copy of the document with all sections, see nature.com/documents/nr-reporting-summary-flat.pdf

Life sciences study design

All studies must disclose on these points even when the disclosure is negative.

Sample size	No statistical method was used to predetermine sample size. Samples sizes were chosen based on the generally accepted standard for the minimum number of replicates needed to obtain conclusive evidence for these types of experiments reported in previous publications. Sample sizes are reported in the figure legend.
Data exclusions	No data were excluded from analysis.
Replication	Metabolome and ubiquitinome analysis experiments were performed once and proximity labeling was performed two independent times. All other experiments were repeated at least three times with similar results unless otherwise indicated.
Randomization	No randomization was used in our experimental design.
Blinding	For cell line experiments, investigators were not blinded to the samples during data collection due to impracticality. For mouse experiments, the investigators were blinded to genotype during procedures and data collection. Investigators were blinded to mouse genotype during ex vivo immunohistochemical staining and analyses.

Reporting for specific materials, systems and methods

We require information from authors about some types of materials, experimental systems and methods used in many studies. Here, indicate whether each material, system or method listed is relevant to your study. If you are not sure if a list item applies to your research, read the appropriate section before selecting a response.

Materials & experimental systems

n/a	Involved in the study
☐	☒ Antibodies
☐	☒ Eukaryotic cell lines
☒	☐ Palaeontology and archaeology
☐	☒ Animals and other organisms
☒	☐ Clinical data
☒	☐ Dual use research of concern
☒	☐ Plants

Methods

n/a	Involved in the study
☒	☐ ChIP-seq
☐	☒ Flow cytometry
☒	☐ MRI-based neuroimaging

Antibodies

Antibodies used

In general, primary antibodies were used at a 1:1000 dilution. Secondary antibodies were used at a 1:5000 dilution.

Rabbit monoclonal anti-4E-BP1, Cell Signaling Technology (Cat# 9644)
Rabbit monoclonal anti-ACC, Cell Signaling Technology (Cat# 3676)
Mouse monoclonal anti-AMPKα, Cell Signaling Technology (Cat# 2793)
Polyclonal rabbit anti-ARL6IP1, Proteintech (Cat# 12988-1-AP)
Rabbit monoclonal anti-ATF4, Cell Signaling Technology (Cat# 11815)
Rabbit polyclonal anti-ATF4, Abcam (Cat# ab31390)
Mouse monoclonal anti-β-Actin, Cell Signaling Technology (Cat# 3700)
Rabbit polyclonal anti-BiP, Cell Signaling Technology (Cat# 3183)
Rabbit polyclonal anti-CHAC1, Proteintech (Cat# 15207-1-AP)
Rabbit polyclonal anti-EDF1, Proteintech (Cat# 12419-1-AP)
Rabbit monoclonal anti-eIF2α , Cell Signaling Technology (Cat# 5324)
Rabbit polyclonal anti-eIF4E, Cell Signaling Technology (Cat# 9742)
Rabbit monoclonal anti-eIF4G, Cell Signaling Technology (Cat# 2469)
Rabbit polyclonal anti-FAM134B, Proteintech (Cat# 21537-1-AP)
Rabbit monoclonal anti-Flag tag (D6W5B), Cell Signaling Technology (Cat# 14793)
Mouse monoclonal anti-GAPDH (6C5), Millipore-Sigma (Cat# MAB374)
Rabbit polyclonal anti-GCN1L1, Bethyl Laboratories (Cat# A301-843A-T)
Rabbit polyclonal anti-GCN2, Cell Signaling Technology (Cat# 3302)
Mouse monoclonal anti-GFP (1E10H7), Proteintech (Cat# 66002-1-Ig)
Mouse monoclonal anti-GIGYF2 , Santa Cruz Biotechnology (Cat# sc-393918)
Mouse monoclonal anti-HA tag (6E2), Cell Signaling Technology (Cat# 2367)
Rabbit polyclonal anti-HOIL-1, Millipore-Sigma (Cat# HPA024185)
Mouse monoclonal anti-HOIL-1, Millipore-Sigma (Cat# MABC576)
Sheep polyclonal anti-HOIL-1, University of Dundee MRC (Cat# HOIL)
Mouse monoclonal anti-HOIP, R&D Systems (Cat# MAB8039)
Rabbit polyclonal anti-HRI, Proteintech (Cat# 20499-1-AP)
Rabbit polyclonal anti-HSP90, Cell Signaling Technology (Cat# 4874)
Mouse monoclonal anti-JNK1, Cell Signaling Technology (Cat# 3708)
Rabbit monoclonal anti-Lamin B1, Cell Signaling Technology (Cat# 13435)
Rabbit polyclonal anti-LC3A/B, Cell Signaling Technology (Cat# 4108)
Rabbit polyclonal anti-MKRN1, Bethyl Laboratories (Cat# A300-990A)
Mouse monoclonal anti-MKRN1, Santa Cruz (Cat# sc-515815)
Mouse monoclonal anti-Myc (9B11), Cell Signaling Technology (Cat# 2276)
Rabbit polyclonal anti-NRF2, Thermo Fisher Scientific (Cat# PA5-27882)
Mouse monoclonal anti-p38α , Cell Signaling Technology (Cat# 9228)
Rabbit polyclonal anti-PABPC1, Proteintech (Cat# 10970-1-AP)
Rabbit polyclonal anti-PGAM5, Cell Signaling Technology (Cat# 24584)
Rabbit monoclonal anti-phospho-ACC (S79), Cell Signaling Technology (Cat# 11818)
Rabbit polyclonal anti-phospho-4E-BP1 (T70), Cell Signaling Technology (Cat# 9455)
Rabbit monoclonal anti-phospho-AMPKα (T172), Cell Signaling Technology (Cat# 2535)
Rabbit monoclonal anti-phospho-eIF2α (S51), Cell Signaling Technology (Cat# 3398)
Rabbit polyclonal anti-phospho-JNK (T183/Y185), Cell Signaling Technology (Cat# 9251)
Rabbit polyclonal anti-phospho-p38 (T180/Y182), Cell Signaling Technology (Cat# 9211)
Rabbit polyclonal anti-phospho-RPS6 (S240/244), Cell Signaling Technology (Cat# 2215)
Rabbit polyclonal anti-PERK, Proteintech (Cat# 24390-1-AP)
Rabbit polyclonal anti-PKR, Proteintech (Cat# 18244-1-AP)
Rabbit monoclonal anti-phospho-ubiquitin (S65), Cell Signaling Technology (Cat# 62802)
Rabbit monoclonal anti-PINK1, Cell Signaling Technology (Cat# 6946)
Mouse monoclonal anti-puromycin (12D10), Millipore-Sigma (Cat# MABE343)
Rabbit polyclonal anti-RPL15, Proteintech (Cat# 16740-1-AP)
Rabbit polyclonal anti-RPL5, Proteintech (Cat# 29092-1-AP)
Rabbit polyclonal anti-RPL7, Proteintech (Cat# 14583-1-AP)
Rabbit polyclonal anti-RPS10, Proteintech (Cat# 14894-1-AP)
Rabbit monoclonal anti-RPS10, Abcam (Cat# ab151550)
Rabbit monoclonal anti-RPS20, Abcam (Cat# ab133776)
Mouse monoclonal anti-RPS6, Cell Signaling Technology (Cat# 2317)

Rabbit monoclonal anti-xCT, Cell Signaling Technology (Cat# 12691)
Rabbit polyclonal anti-ZAK, Proteintech (Cat# 28761-1-AP)
Rabbit polyclonal anti-ZNF598, Novus Biologicals (Cat# NBP1-84659)
Donkey polyclonal anti-rabbit IgG, HRP-linked whole Ab, Cytiva (Cat# NA934)
Sheep polyclonal anti-mouse IgG, HRP-linked whole Ab, Cytiva (Cat# NA931)
Donkey polyclonal anti-sheep IgG HRP conjugate, Novus Biologicals (Cat# HAF016)
Mouse monoclonal anti-rabbit IgG (conformation specific) HRP conjugate, Cell Signaling Technology (Cat# 5127)
Rabbit monoclonal anti-mouse IgG (light chain specific) HRP conjugate, Cell Signaling Technology (Cat# 58802)
Mouse Anti-Sheep IgG, light chain specific, Jackson ImmunoResearch (Cat# 213-002-177)
Mouse Anti-Sheep IgG, light chain specific, Jackson ImmunoResearch (Cat# 213-002-177)

Validation

The antibodies used in this study have been validated as reported on the manufacturer's website. When applicable, antibodies were validated using CRISPR-Cas9 knockout cells or siRNA-silenced cells.
anti-4E-BP1, Cell Signaling Technology (Cat# 9644): https://www.cellsignal.com/products/primary-antibodies/4e-bp1-53h11-rabbit-mab/9644
anti-ACC, Cell Signaling Technology (Cat# 3676): https://www.cellsignal.com/products/primary-antibodies/acetyl-coa-carboxylase-c83b10-rabbit-mab/3676
anti-AMPKα, Cell Signaling Technology (Cat# 2793): https://www.cellsignal.com/products/primary-antibodies/ampka-f6-mouse-mab/2793
anti-ARL6IP1, Proteintech (Cat# 12988-1-AP): https://www.ptglab.com/products/ARL6IP1-Antibody-12988-1-AP.htm
anti-ATF4, Cell Signaling Technology (Cat# 11815): https://www.cellsignal.com/products/primary-antibodies/atf-4-d4b8-rabbit-mab/11815
anti-ATF4, Abcam (Cat# ab31390): https://www.abcam.com/en-us/products/primary-antibodies/atf-4-antibody-ab31390
anti-β-Actin, Cell Signaling Technology (Cat# 3700): https://www.cellsignal.com/products/primary-antibodies/b-actin-8h10d10-mouse-mab/3700
anti-BiP, Cell Signaling Technology (Cat# 3183): https://www.cellsignal.com/products/primary-antibodies/bip-antibody/3183
anti-CHAC1, Proteintech (Cat# 15207-1-AP): https://www.ptglab.com/products/CHAC1-Antibody-15207-1-AP.htm
anti-EDF1, Proteintech (Cat# 12419-1-AP): https://www.ptglab.com/products/EDF1-Antibody-12419-1-AP.htm
anti-eIF2α , Cell Signaling Technology (Cat# 5324): https://www.cellsignal.com/products/primary-antibodies/eif2a-d7d3-xp-rabbit-mab/5324
anti-eIF4E, Cell Signaling Technology (Cat# 9742): https://www.cellsignal.com/products/primary-antibodies/eif4e-antibody/9742
anti-eIF4G, Cell Signaling Technology (Cat# 2469): https://www.cellsignal.com/products/primary-antibodies/eif4g-c45a4-rabbit-mab/2469
anti-FAM134B, Proteintech (Cat# 21537-1-AP): https://www.ptglab.com/products/FAM134B-Antibody-21537-1-AP.htm
anti-Flag tag (D6W5B), Cell Signaling Technology (Cat# 14793): https://www.cellsignal.com/products/primary-antibodies/dykddddk-tag-d6w5b-rabbit-mab-binds-to-same-epitope-as-sigma-aldrich-anti-flag-m2-antibody/14793
anti-GAPDH (6C5), Millipore-Sigma (Cat# MAB374): https://www.sigmaaldrich.com/CA/en/product/mm/mab374
anti-GCN1L1, Bethyl Laboratories (Cat# A301-843A-T): https://www.fortislife.com/products/primary-antibodies/rabbit-anti-gcn1l1-antibody/BETHYL-A301-843
anti-GCN2, Cell Signaling Technology (Cat# 3302): https://www.cellsignal.com/products/primary-antibodies/gcn2-antibody/3302
anti-GFP (1E10H7), Proteintech (Cat# 66002-1-Ig): https://www.ptglab.com/products/eGFP-Antibody-66002-1-Ig.htm
anti-GIGYF2 , Santa Cruz Biotechnology (Cat# sc-393918): https://www.scbt.com/p/gigyf2-antibody-a-12
anti-HA tag (6E2), Cell Signaling Technology (Cat# 2367): https://www.cellsignal.com/products/primary-antibodies/ha-tag-6e2-mouse-mab/2367
anti-HOIL-1, Millipore-Sigma (Cat# HPA024185): https://www.sigmaaldrich.com/CA/en/product/sigma/hpa024185
anti-HOIL-1, Millipore-Sigma (Cat# MABC576): https://www.sigmaaldrich.com/CA/en/product/mm/mabc576
anti-HOIL-1, University of Dundee MRC (Cat# HOIL): https://mrcppureagents.dundee.ac.uk/antibody-ext/589249
anti-HOIP, R&D Systems (Cat# MAB8039): https://www.rndsystems.com/products/human-hoip-rnf31-antibody-875227_mab8039
anti-HRI, Proteintech (Cat# 20499-1-AP): https://www.ptglab.com/products/EIF2AK1-Antibody-20499-1-AP.htm
anti-HSP90, Cell Signaling Technology (Cat# 4874): https://www.cellsignal.com/products/primary-antibodies/hsp90-antibody/4874
anti-JNK1, Cell Signaling Technology (Cat# 3708): https://www.cellsignal.com/products/primary-antibodies/jnk1-2c6-mouse-mab/3708
anti-Lamin B1, Cell Signaling Technology (Cat# 13435): https://www.cellsignal.com/products/primary-antibodies/lamin-b1-d9v6h-rabbit-mab/13435
anti-LC3A/B, Cell Signaling Technology (Cat# 4108): https://www.cellsignal.com/products/primary-antibodies/lc3a-b-antibody/4108
anti-MKRN1, Bethyl Laboratories (Cat# A300-990A): https://www.thermofisher.com/antibody/product/MKRN1-Antibody-Polyclonal/A300-990A
anti-MKRN1, Santa Cruz (Cat# sc-515815): https://www.scbt.com/p/makorin-1-antibody-c-8?
anti-Myc (9B11), Cell Signaling Technology (Cat# 2276): https://www.cellsignal.com/products/primary-antibodies/myc-tag-9b11-mouse-mab/2276
anti-NRF2, Thermo Fisher Scientific (Cat# PA5-27882): https://www.thermofisher.com/antibody/product/Nrf2-Antibody-Polyclonal/PA5-27882
anti-p38α , Cell Signaling Technology (Cat# 9228): https://www.cellsignal.com/products/primary-antibodies/p38a-mapk-l53f8-mouse-mab/9228
anti-PABPC1, Proteintech (Cat# 10970-1-AP): https://www.ptglab.com/products/PABPC1,PABP-Antibody-10970-1-AP.htm
anti-PGAM5, Cell Signaling Technology (Cat# 24584): https://www.cellsignal.com/products/primary-antibodies/pgam5-long-isoform-antibody/24584
anti-phospho-ACC (S79), Cell Signaling Technology (Cat# 11818): https://www.cellsignal.com/products/primary-antibodies/phospho-acetyl-coa-carboxylase-ser79-d7d11-rabbit-mab/11818
anti-phospho-4E-BP1 (T70), Cell Signaling Technology (Cat# 9455): https://www.cellsignal.com/products/primary-antibodies/phospho-4e-bp1-thr70-antibody/9455
anti-phospho-AMPKα (T172), Cell Signaling Technology (Cat# 2535): https://www.cellsignal.com/products/primary-antibodies/phospho-ampka-thr172-40h9-rabbit-mab/2535
anti-phospho-eIF2α (S51), Cell Signaling Technology (Cat# 3398): https://www.cellsignal.com/products/primary-antibodies/phospho-eif2a-ser51-d9g8-xp-rabbit-mab/3398

anti-phospho-JNK (T183/Y185), Cell Signaling Technology (Cat# 9251): https://www.cellsignal.com/products/primary-antibodies/phospho-sapk-jnk-thr183-tyr185-antibody/9251
anti-phospho-p38 (T180/Y182), Cell Signaling Technology (Cat# 9211): https://www.cellsignal.com/products/primary-antibodies/phospho-p38-mapk-thr180-tyr182-antibody/9211
anti-phospho-RPS6 (S240/244), Cell Signaling Technology (Cat# 2215): https://www.cellsignal.com/products/primary-antibodies/phospho-s6-ribosomal-protein-ser240-244-antibody/2215
anti-PERK, Proteintech (Cat# 24390-1-AP): https://www.ptglab.com/products/EIF2AK3-Antibody-24390-1-AP.htm
anti-PKR, Proteintech (Cat# 18244-1-AP): https://www.ptglab.com/products/EIF2AK2-Antibody-18244-1-AP.htm
anti-phospho-ubiquitin (S65), Cell Signaling Technology (Cat# 62802): https://www.cellsignal.com/products/primary-antibodies/phospho-ubiquitin-ser65-e2j6t-rabbit-mab/62802
anti-PINK1, Cell Signaling Technology (Cat# 6946): https://www.cellsignal.com/products/primary-antibodies/pink1-d8g3-rabbit-mab/6946
anti-puromycin (12D10), Millipore-Sigma (Cat# MABE343): https://www.sigmaaldrich.com/CA/en/product/mm/mabe343
anti-RPL15, Proteintech (Cat# 16740-1-AP): https://www.ptglab.com/products/RPL15-Antibody-16740-1-AP.htm
anti-RPL5, Proteintech (Cat# 29092-1-AP): https://www.ptglab.com/products/RPL5-Antibody-29092-1-AP.htm
anti-RPL7, Proteintech (Cat# 14583-1-AP): https://www.ptglab.com/products/RPL7-Antibody-14583-1-AP.htm
anti-RPS10, Proteintech (Cat# 14894-1-AP): https://www.ptglab.com/products/RPS10-Antibody-14894-1-AP.htm
anti-RPS10, Abcam (Cat# ab151550): https://www.abcam.com/en-us/products/primary-antibodies/rps10-antibody-epr8545-ab151550
anti-RPS20, Abcam (Cat# ab133776): https://www.abcam.com/en-us/products/primary-antibodies/rps20-antibody-epr8716-ab133776
anti-RPS6, Cell Signaling Technology (Cat# 2317): https://www.cellsignal.com/products/primary-antibodies/s6-ribosomal-protein-54d2-mouse-mab/2317
anti-xCT, Cell Signaling Technology (Cat# 12691): https://www.cellsignal.com/products/primary-antibodies/xct-slc7a11-d2m7a-rabbit-mab/12691
anti-ZAK, Proteintech (Cat# 28761-1-AP): https://www.ptglab.com/products/ZAK-Antibody-28761-1-AP.htm
anti-ZNF598, Novus Biologicals (Cat# NBP1-84659): https://www.novusbio.com/products/znf598-antibody_nbp1-84659

Eukaryotic cell lines

Policy information about cell lines and Sex and Gender in Research

Cell line source(s)	AC16 cells (human) were a gift from Dr. Iain Scott (UPMC) and developed by Davidson, MM et al. 2005 (PMID: 15913645) WT and HOIL-1ΔRING1 MEFs were previously generated by Fuseya, Y et al. 2020 (PMID: 32393887). 786-O cells (human, male) were acquired from ATCC (CRL-1932). HEK293T cells (human, female) were acquired from ATCC (CRL-3216).
Authentication	Cell lines were not authenticated in-house.
Mycoplasma contamination	All cells were tested routinely for mycoplasma contamination using PlasmoTest™ Mycoplasma Detection Kit (Invivogen). All cell lines tested negative.
Commonly misidentified lines (See ICLAC register)	No commonly misidentified cell lines were used in this study.

Animals and other research organisms

Policy information about studies involving animals; ARRIVE guidelines recommended for reporting animal research, and Sex and Gender in Research

Laboratory animals	Mice were maintained in a pathogen-free facility on a 12h light, 12h dark cycle with ad libitum food and water. All breeding animals were heterozygous for the Rbck1 null (ΔRBR) allele and had been previously backcrossed to a C57BL/6 background more than nine times. Age-matched male and female HOIL-1+/+ and HOIL-1ΔRBR littermates were used in all experiments.
Wild animals	No wild animals were used.
Reporting on sex	Both male and female mice were used. Equal numbers of both sexes were used in all experiments.
Field-collected samples	No field samples were collected.
Ethics oversight	All procedures were reviewed and approved by the Institutional Animal Care and Use Committees (IACUC) at Yale, protocols 10019 and 07788.

Note that full information on the approval of the study protocol must also be provided in the manuscript.

Plants

Seed stocks	*Report on the source of all seed stocks or other plant material used. If applicable, state the seed stock centre and catalogue number. If plant specimens were collected from the field, describe the collection location, date and sampling procedures.*
Novel plant genotypes	*Describe the methods by which all novel plant genotypes were produced. This includes those generated by transgenic approaches, gene editing, chemical/radiation-based mutagenesis and hybridization. For transgenic lines, describe the transformation method, the number of independent lines analyzed and the generation upon which experiments were performed. For gene-edited lines, describe the editor used, the endogenous sequence targeted for editing, the targeting guide RNA sequence (if applicable) and how the editor was applied.*
Authentication	*Describe any authentication procedures for each seed stock used or novel genotype generated. Describe any experiments used to assess the effect of a mutation and, where applicable, how potential secondary effects (e.g. second site T-DNA insertions, mosiacism, off-target gene editing) were examined.*

Flow Cytometry

Plots

Confirm that:

☒ The axis labels state the marker and fluorochrome used (e.g. CD4-FITC).

☒ The axis scales are clearly visible. Include numbers along axes only for bottom left plot of group (a 'group' is an analysis of identical markers).

☐ All plots are contour plots with outliers or pseudocolor plots.

☒ A numerical value for number of cells or percentage (with statistics) is provided.

Methodology

Sample preparation	For propidium iodide staining: Cells were seeded in 12-well plates such that they were at 70% confluence at the time of starvation or treatment the following day (6x10^4 AC16 cells, 7x10^4 786-O cells, 3x10^4 MEFs). After the indicated treatment, cells were harvested by collecting the media containing floating cells in 5 mL round bottom polystyrene tubes (Corning 352052). Adherent cells were washed once with room temperature PBS, trypsinized, and pooled with the floating cells. Cells were centrifuged at 2,400 rpm for 5 minutes at 4°C. The supernatant was removed and cell pellets were resuspended in 250 µL PBS containing 5 µg/mL propidium iodide (ThermoFisher P3566) and stained for 15 minutes at room temperature in the dark. For O-propargyl-puromycin incorporation: After the indicated treatment (glucose starvation, anisomycin treatment), 20 µM O-propargyl-puromycin (MedChemExpress HY-15680) was added to cell culture media for 30 minutes. The media was then aspirated, cells were washed once with pre-warmed PBS, trypsinized, inactivated with PBS + 10% FBS, and collected in 5 mL round bottom polystyrene tubes. The cell pellet was washed once with PBS. Cells were fixed by resuspending in 250 µL 4% paraformaldehyde and incubated at room temperature for 10 minutes. After washing the pellet once with PBS + 3% BSA, cells were permeabilized with 0.25% Triton in PBS for 15 minutes at room temperature. Cells were then washed twice with PBS + 3% BSA. Alexa Fluor 647 was clicked onto O-propargyl-puromycin using the Click-iT Plus Alexa Fluor 647 picolyl aizde toolkit (Invitrogen C10643) according to the manufacturer's instructions. Cells were stained with Alexa Fluor 647-conjugated O-propargyl-puromycin for 30 minutes at room temperature in the dark, then washed once with PBS + 3% BSA.
Instrument	Samples were processed on a BD LSRFortessa X-20 Cell Analyzer
Software	Samples were collected using FACSDiva 6.1 (BD Biosciences) and analyzed using FlowJo v10 (FlowJo LLC)
Cell population abundance	At least 10,000 cells were acquired per sample.
Gating strategy	Samples were first gated on SSC-A x FSC-A to include dead cells but exclude debris. From these, propidium iodide-positive cells were gated as shown in the source data, typically ~10^4-10^5.

☒ Tick this box to confirm that a figure exemplifying the gating strategy is provided in the Supplementary Information.